UCRL-19654
c.2

MOLECULAR BEAM KINETICS

David D. Parrish
(Ph. D. Thesis)

October 1970

AEC Contract No. W-7405-eng-48

LAWRENCE RADIATION LABORATORY
UNIVERSITY of CALIFORNIA BERKELEY

UCRL-19654
c.2

DISCLAIMER

TABLE OF CONTENTS

MOLECULAR BEAM KINETICS

David D. Parrish

Inorganic Materials Research Division, Lawrence Radiation Laboratory
Department of Chemistry, University of California
Berkeley, California

ABSTRACT

An apparatus has been constructed to perform magnetic deflection analysis of reactive scattering in crossed molecular beams of neutral species. An inhomogeneous deflecting magnet between the surface ionization detector and the collision zone of the two crossed thermal energy beams was used to distinguish elastic reactant scattering from reactive product scattering by utilizing the large difference in their magnetic dipoles. Studies have been made of the reactions of Li with NO_2, CH_3NO_2, SF_6, CCl_4, and CH_3I. The total reaction cross sections and the reactive attenuations of the wide-angle Li elastic scattering for all of these gases are considerably smaller than are the corresponding features previously reported for the reactions of Li + XY (XY = Cl_2, Br_2 and ClI). However, interesting differences are observed in the product LiX center-of-mass (CM) angular distributions for the five gases studied here. The LiO product of the NO_2 reaction is more sharply peaked in the direction of the Li atom than are the corresponding LiX products of the Li + XY reaction. The $LiNO_2$ and LiF products of the CH_3NO_2 and SF_6 reactions exhibit very broad, almost isotropic CM angular distributions. The LiCl and LiI products of the CCl_4 and CH_3I reactions are predominantly scattered into the backward hemisphere in the CM coordinate system. The features of the NO_2 reaction are discussed in terms of the electron transfer mechanism which has been advanced to account for the features of the reactions of the alkali atoms with the halogen molecules.

A classical harmonic forces, normal modes model has been developed to allow convenient investigation of certain features of the dynamics of chemical reactions. The Cs + alkyl iodide reaction dynamics are investigated by means of a linear, four-particle ($Cs-I-CH_2-R$ where R = H, CH_3, C_2H_5 or C_3H_7) application of this model. The full reaction exoergicity is initially partitioned between potential energy of Cs-I extension and $I-CH_2$ compression, and the trajectories of the four particles are followed until the $I-CH_2$ distance reaches a critical extension, at which point the reaction is assumed to be complete. The model is examined as a function of two parameters, the $I-CH_2$ force constant, k_2, and the initial repulsive energy in $I-CH_2$ compression, P. By varying k_2, the model spans the spectrum of possible direct-interaction reaction dynamics from the limit of the adiabatic, very slow $CsI-CH_2R$ separation (low k_2 limit) to the limit of impulsive release of the $I-CH_2$ compression (high k_2 limit). In contrast to previous calculations, we obtain a good qualitative fit to the experimentally reported product recoil energies if: (1) a relatively high value of k_2, near the impulsive limit, is used; (2) the potential surface is largely repulsive, with P = 19.0 kcal/mole out of a total 28.7 kcal/mole reaction exoergicity and (3) both the CsI and the CH_2-R alkyl radical carry off substantial internal excitations. A similar, linear, three particle model applies the two derived values of k_2 and P to the reactions of all of the alkali metals with methyl iodide. Experimental measurements of the energy partitioning is available only for the Cs, Rb, and K reactions; this data is well reproduced by the model. The unstudied Li and Na reactions are predicted to exhibit significant deviations from the trend found for the three heavier alkali metals, and a possible

explanation of the reported anomalously small total reactive cross section of the Na + CH_3I reaction is presented. Another application of the linear, three particle model shows that the small variations that have been observed in the energy partitioning in the reactions of the alkali metals with the diatomic halogens may be explained by the effect on the reaction dynamics of the varying alkali to halogen mass ratio.

An apparatus has been constructed to measure the velocity dependence of excitation transfer in atomic collisions. A velocity selected thermal beam of Tl atoms is crossed with a thermal beam of Hg atoms in which a small fraction of the Hg atoms are excited to the $^3P_{0,2}$ states by electron bombardment. A photomultiplier equipped with a narrow band pass interference filter and located below the beam collision zone provides a sensitive and specific detector for collisionally excited Tl atoms in a particular energy level. Results for the Tl 7s $^2S_{1/2}$ state indicate that the total cross section for creating this energy level decreases as the asymptotic relative velocity, V, increases. The derived data points are well fit by a V^{-2} dependence. A method for the time normalization and statistical analysis of noisy data is presented.

I. INTRODUCTION

The technique of crossed molecular beam offers the chemist a unique opportunity to observe collision dynamics without the loss of direct information that statistical and thermodynamic averaging entails. Although there are severe practical problems, molecular beam kinetics can, at least in principle, approach the ideal experiment where the incident species are prepared in given initial states and then the states of the scattered products are determined directly after the collision in which they are formed. Product parameters which are capable of being determined are the product identities, recoil direction, and the partitioning of the available energy among the products' translational and internal (rotational, vibrational and electronic) degrees of freedom. The use of the two crossed beams is particularly advantageous in the investigation of low energy collisions; the distribution of relative velocities of approach is much more narrowly confined than is possible if a single beam is allowed to impinge on a volume of gas confined in a scattering cell.

Investigations of the dynamics of neutral collisions in crossed molecular beams received a great impetus from the first observation of a chemical reaction in crossed neutral beams by Bull and Moon[1] and from the measurement of the first product angular distribution by Datz and Taylor.[2] In the sixteen years since these first successes, crossed beam studies have proliferated in sophistication as well as quantity and diversity. Almost all of the early studies of neutral systems investigated the scattering of alkali metals due to the existence of positive surface ionization[2] which provides an extremely sensitive and specific detector for species with small ionization potentials.

Successful crossed beam studies utilizing detection by electron bombardment and mass analysis or by negative surface ionization have been accomplished only very recently. The processes that can be studied in crossed neutral beams may be roughly divided into three categories: elastic, inelastic and reactive scattering.

During an elastic collision neither energy transfer nor chemical rearrangement occurs. The interaction potential that completely determines the dynamics of such a collision can be adequately represented by a single central force expression, thus allowing a relatively tractable mathematical treatment. Consequently, measurement of the angular distribution of the elastic scattering of a non-reactive system allows the extraction of a detailed description of the potential function.[3] In order to obtain the potential function unambiguously, it is necessary to have both a very narrow angular resolution and a closely confined distribution of initial relative velocities. Early studies were largely confined to the alkali metal systems and yielded only a two parameter fit to an assumed potential form. Recently however, the best alkali results[3a] and even some greatly improved studies of non-alkali systems[4] promise to allow direct inversion from the experimental data to the potential function. The elastic scattering from chemically reactive systems not only yields information on the interaction potential, but also elucidates the reaction dynamics; in particular the probability of reaction as a function of impact parameter may be approximately extracted from the elastic scattering.[5]

An inelastic collision event is characterized by a change of the internal quantum states of the species during the period of interaction;

thus, compared to elastic scattering, a much more complicated and diverse situation exists. Very few systematic studies of inelastic processes in neutral, low energy systems have yet been reported. Chapter VI and VII of this thesis describe a crossed beam study of the velocity dependence of electronic energy transfer in an atomic collision.

A molecular interaction that involves a chemical change in the collision partners is defined as reactive scattering. Intensive investigations of the reactive scattering of alkali metal systems[6] have directly measured the product angular distributions, translational energy distributions and rotational excitation. In addition, the variation of these reaction characteristics with initial relative translational energy and molecular orientation have been determined for a few of these systems. A very recent study[7] has successfully measured the vibrational energy distribution of a reaction product by using the reactive scattering from two crossed beams as the source for a molecular beam electric resonance spectrometer. Previously, such direct information had been available only from observation of infrared chemiluminescence.[8] The results presented here in Chapter II and III and Appendices A and B extend crossed beam investigations of reactive scattering to(excepting Fr) the last uninvestigated member of the alkali family, Li; two thermal beams are employed and the product angular distributions and nominal values of the products' translational energy are extracted. Recently, reactive scattering studies have also been carried out for non-alkali systems and very detailed results for a wide variety of reactive systems should be available in the near future.[9]

Chapters IV and V present a very simple model suitable for the investigation of collision dynamics in a form that facilitates the achievement

of physical insight into the dominating features of a collision. Suprisingly accurate reproductions of certain features of suitable systems have been obtained.

REFERENCES

1. T. H. Bull and P. B. Moon, Disc. Far. Soc. 17, 54 (1954).

2. E. H. Taylor and S. Datz, J. Chem. Phys. 23, 67 (1955).

3. R. B. Bernstein and J. T. Muckerman, Adv. Chem. Phys. 12, 389 (1967). This review summarizes the theory and results as they stood at that time.

3a. H. Pauly and J. P. Toennies, "Beam Experiments at Thermal Energies" in B. Bederson and W. L. Fite, Eds., Methods of Experimental Physics. VIIA. Atomic Interactions (Academic Press, New York, 1968) p. 227.

4. J. M. Parson, T. P. Schafer, F. P. Tully, P. E. Siska, Y. C. Wong, and Y. T. Lee, J. Chem. Phys. 53, 2123 (1970).

5. For reviews, see (a) E. F. Greene, A. L. Moursund, and J. Ross, Adv. Chem. Phys. 10, 135 (1966). (b) E. F. Greene and J. Ross, Science, 159, 587 (1968).

6. Recent reviews include: (a) D. R. Herschbach, Adv. Chem. Phys. 10, 319 (1966). (b) J. P. Toennies, Ber. Bunsenges. Physik. Chem. 72, 927 (1968).

7. S. M. Freund, G. A. Fisk, D. R. Herschbach, and W. Klemperer, J. Chem. Phys. to be published.

8. K. G. Anlauf, J. C. Polanyi, W. H. Wong, and K. B. Woodall, J. Chem. Phys. 49, 5189 (1968), and references cited therein.

9. The most recent review of reactive scattering of alkali as well as nonalkali systems is: D. R. Herschbach International School of Physics "Enrico Fermi" Course 44 - Molecular Beams and Reaction Kinetics (Ch. Schlier, Ed., Academic Press, N.Y., 1970).

II. APPARATUS FOR MAGNETIC DEFLECTION ANALYSIS OF REACTIVE SCATTERING IN CROSSED MOLECULAR BEAMS

A. Introduction

The design of this apparatus was guided by three considerations. First, it was desired to carry out quickly primitive crossed molecular beam studies of the angular distributions of the reactive scattering of Li, and possibly the heavier members of the alkaline earth family, with halogen containing compounds. Such studies, utilizing two reactant beams with full thermal velocities and with no velocity analysis of the products, have been carried out for Na, K, Rb and Cs where the reaction partners have included HX, RX, X_2, XX', SX_2, PX_3, CH_2X_2, CHX_3, CX_4, SnX_4, SF_6 and CF_3I as well as NO_2 and RNO_2 (which form MO and MNO_2, respectively). (Here, as well as elsewhere in this thesis, M, R and X represent the alkali metal or alkaline earth atom, and organic radical and a halogen atom, respectively). Several reviews[1] of these studies have been given. The qualitative features of the center of mass angular and kinetic energy product distributions may be extracted from the measured laboratory angular distributions. Similar studies have been completed in this laboratory for ten reactions of Li atoms.[2] An initial experiment reproduced the results of the two filament, differential surface ionization investigation of the reaction of Na with Br_2,[3] thereby demonstrating the reliability of the technique employed here. As a second consideration it was desired to construct the apparatus so that it can be easily modified to allow more detailed investigations of these reactions including, for example, velocity and rotational energy analysis of the scattered products or velocity selection of one of the reactant beams. These modifications are

now being carried out by other members of the research group. Finally, it was desired to construct an apparatus that would have as great a flexibility as possible in the investigation of other aspects of collision dynamics. Some results of the other studies also carried out in this apparatus will be discussed later.

The previous studies of the alkali metal reactions have been possible due to the utilization of surface ionization as a sensitive and specific detector. The primary problem faced in extending these studies to lithium and the alkaline earths is the detection of these species which have higher ionization potentials and thus much lower detection efficiencies (approximately 1.0 to 0.1 percent compared with essentially 100 percent for Cs). In the previous studies differential surface ionization was employed to measure the scattered M and MX separately; however, due to the decreased detection efficiencies of the species in the proposed studies, it was deemed desirable to construct an apparatus which would allow either the two filament technique or magnetic deflection analysis to be utilized to distinguish between the elastically and reactively scattered alkali or alkaline earth species. Some of the reactions of the heavier alkali atom reactions have also been studied with magnetic deflection analysis,[4] but these studies have served primarily to substantiate previous two-filament results rather than to study unexamined reactions.

The apparatus is described in this chapter as it was designed and built for use in the Li atom experiments discussed in Ref. 2 and those to be described in the following chapter. Lists of the mechanical and electrical drawings for this apparatus are given in Appendicies A and B;

Figure 1. Diagram of the vacuum chamber, as viewed from above. The reactant beams, which cross at an angle $\gamma = 90^\circ$, effuse from ovens mounted on a platform which may be rotated from $\Theta = -55^\circ$ to $\Theta = +120^\circ$ with respect to the stationary deflecting magnet and detector assembly. Only scattering in the plane of the reactant beams is measured and the sense of Θ depicted in this figure is taken as positive, with $\Theta = 0^\circ$ in the direction of the Li atom beam. The entire detector assembly (ionizing filament, ion optics, analyzing magnet, electron multiplier, and electrical shield) may be scanned across the gap of the deflecting magnet in order to measure beam profiles and deflection patterns.

Figure 2. Schematic diagram of auxilliary components of the apparatus.

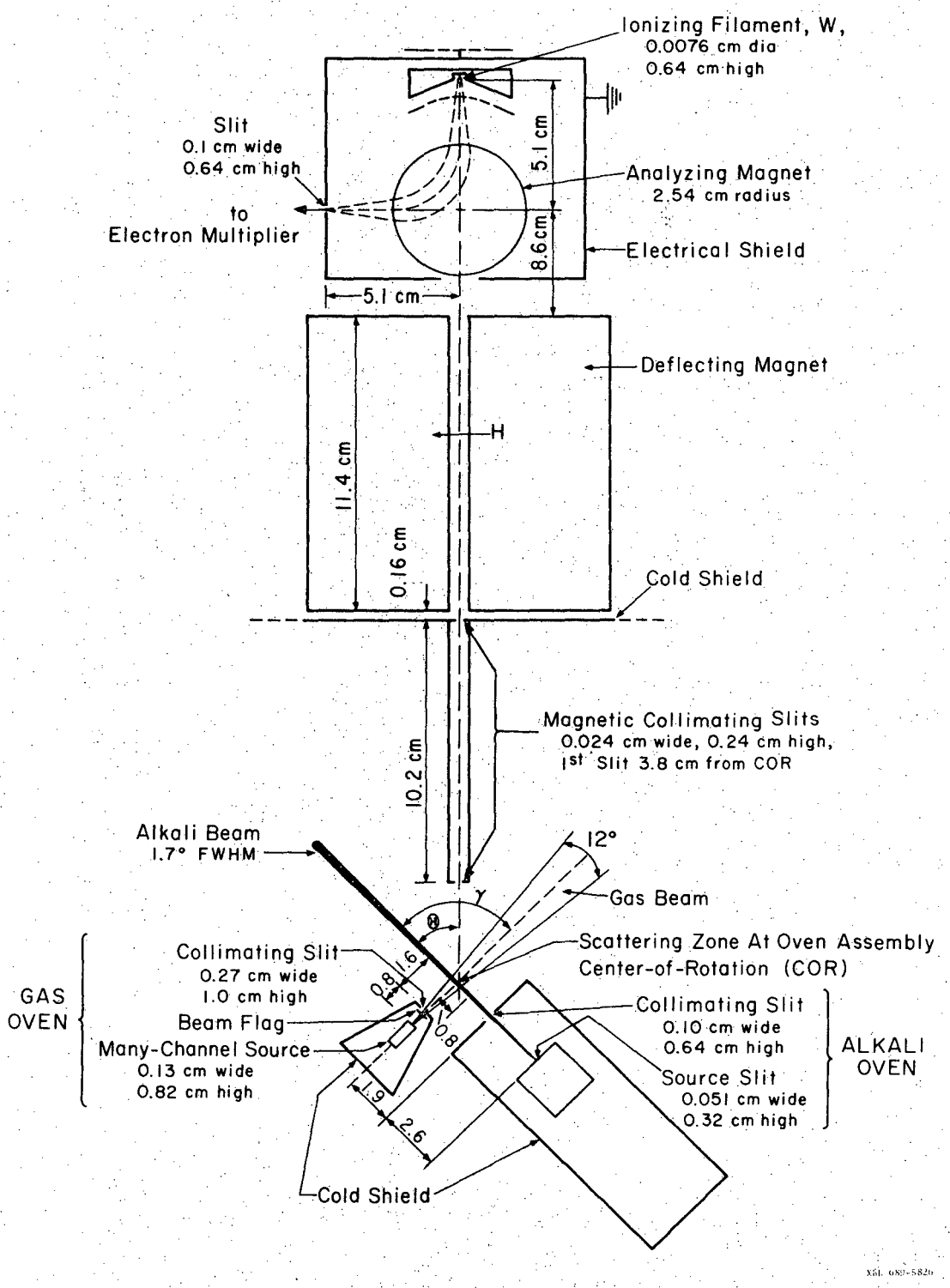
Ionizing Filament, W,
0.0076 cm dia
0.64 cm high
Slit
0.1 cm wide
0.64 cm high
to
Electron Multiplier
5.1 cm
Analyzing Magnet
2.54 cm radius
8.6 cm
Electrical Shield
5.1 cm
Deflecting Magnet
H
11.4 cm
0.16 cm
Cold Shield
10.2 cm
Magnetic Collimating Slits
0.024 cm wide, 0.24 cm high,
1st Slit 3.8 cm from COR
Alkali Beam
1.7° FWHM
12°
Gas Beam
γ
θ
Scattering Zone At Oven Assembly
Center-of-Rotation (COR)
GAS
OVEN
Collimating Slit
0.27 cm wide
1.0 cm high
1.6
0.8
Beam Flag
Many-Channel Source
0.13 cm wide
0.82 cm high
0.8
Collimating Slit
0.10 cm wide
0.64 cm high
Source Slit
0.051 cm wide
0.32 cm high
ALKALI
OVEN
1.9
2.6
Cold Shield
XBL 689-5826

Figure 1

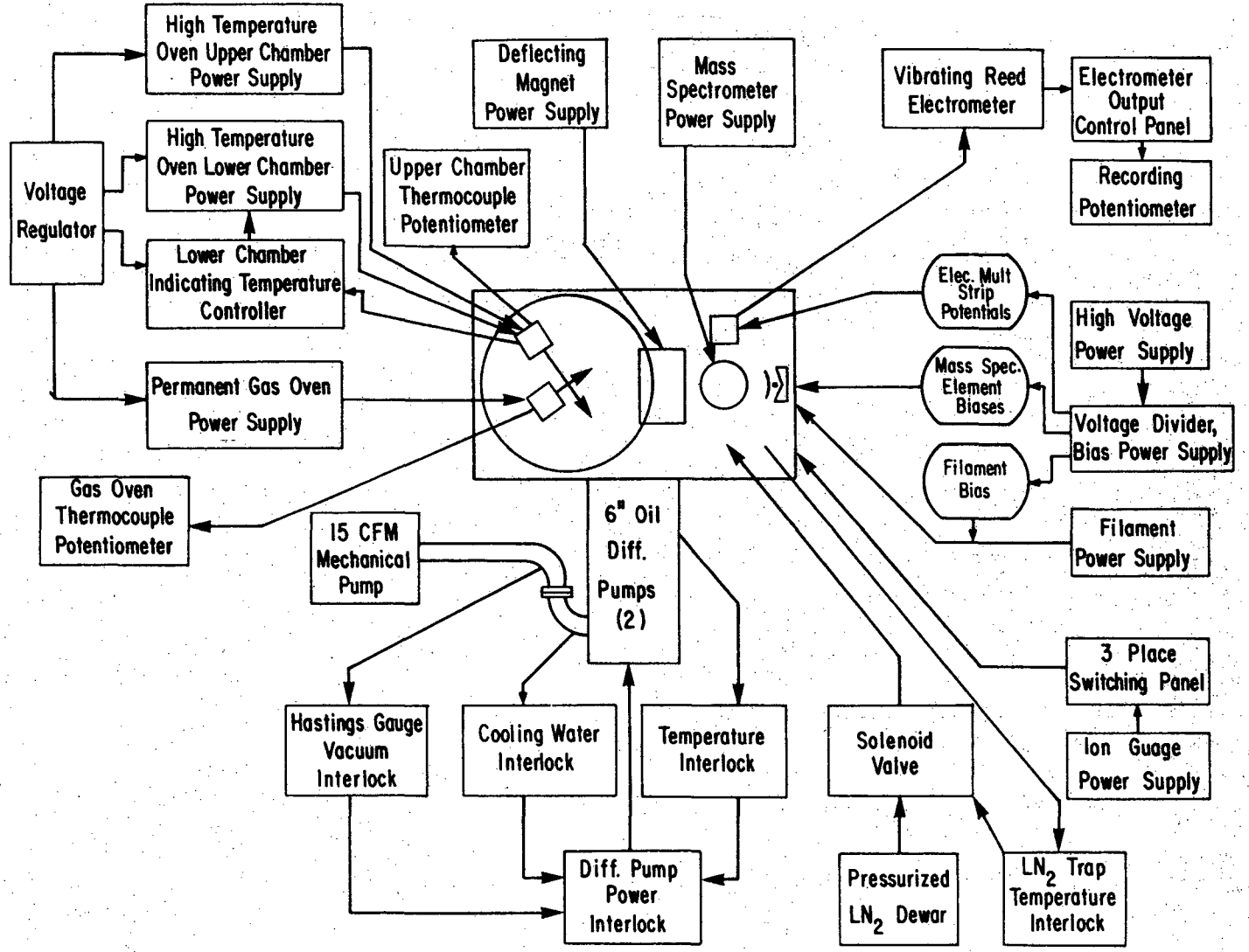

XBL 706-1222

Figure 2

these drawings are on file at Lawrence Radiation Laboratory, Berkeley. A diagram of the essential parts of the apparatus which are enclosed in the vacuum chamber is shown in Fig. 1, and Fig. 2 shows a general schematic of the apparatus together with a block diagram of the electronics.

B. Vacuum System

1. Vacuum Chamber

The vacuum system consists of a single chamber containing both beam sources and the detector; this lack of differential pumping limits the apparatus, as originally constructed and used in this investigation, to studies of reactions in which both reactants are condensable at liquid nitrogen temperature. The chamber is constructed as a large box (37"×33"×27"); each of the four sides is fabricated from heavy aluminum alloy (Alcoa-6061) plate and is removable. Thus, the main body of the chamber consists of the bottom and the top with a vertical support at each corner; this also is fabricated from the same aluminum alloy with welded construction throughout. The four vertical supports are drilled and tapped to receive the bolts by which the sides are attached. The advantage of this construction is that any desired wall or walls may be removed for convenient access for working inside the chamber; the other walls are left in place permanently for the duration of the experiment, thereby providing a flat surface for mounting smaller flanges and other apparatus components by tapping directly into wall. The ability to remove the walls allows easy modification and, if necessary, replacement; in addition, differentially pumped beam source chambers may be bolted on in place of the walls to give the apparatus considerable flexibility of application. A 12" diameter rotating lid is mounted in the top of the vacuum chamber. This lid

may be rotated from outside the chamber while maintaining a vacuum inside.

The low pressure of residual background gases that is necessary to insure minimal scattering of the molecular beams can be achieved only through very fast pumps and extensive trapping since the beam sources represent large leaks into the system. The lowest pressure reached in the system was 5×10^{-8} Torr (uncorrected ion gauge reading) when no experiment was being conducted; however, the pressure typically rose to 1.5×10^{-6} Torr during an experimental run if one of the source ovens required a high temperature. This high pressure was partially due to outgassing of materials that surround the oven and are thus heated by it.

2. Pumps, Traps, and Associated Circuitry

The main pumping for non-condensable gases is obtained from two Consolidated Vacuum Corporations PMC-6B, 6" oil diffusion pumps (nominal pumping speed of each is 1400 liters/sec) while liquid nitrogen cooled surfaces provide very high pumping speeds for condensable gases (typically 1-20 liters/sec/cm^2).[5] The complete interior of the vacuum chamber is enclosed by a copper box equipped with removable walls; in order to maintain the necessary low temperature, this box is attached to a large liquid nitrogen reservoir (capacity 28 liters). This copper tank covers the entire bottom of the apparatus and the diffusion pump baffles are built into it; these baffles have an optically dense design and undoubtedly reduce the effective pumping speed of the oil diffusion pumps. No attempt was made to measure this but the reduction is likely to be a factor of two or greater. A standard 1" Swadgelok fitting was used to couple the liquid nitrogen fill tube to the reservoir; this provides a leak-tight seal even after repeated thermal cycling. The trap is filled automatically by means

of a thermostat interlocked with a pressurized dewar equipped with a solenoid value. The trap is suspended by thin stainless steel straps in order to maximize thermal isolation. Additional pumping in the region of the beam sources is provided by a smaller liquid nitrogen trap (6 liter capacity) suspended from the rotating lid on thin stainless steel tubes; shields surrounding the ovens are attached to and cooled by this reservoir. This tank is filled manually, and is kept cold only during an experimental run.

A single Welch 1397B two stage mechanical pump with a speed of approximately 15 cubic feet per minute at 10 microns is used as fore-pump. A Hastings thermocouple vacuum gauge monitors the fore pressure; it controls an interlock that turns of the power to the diffusion pumps if the pressure rises above a preset value. The diffusion pump power is also interlocked to the flow of the cooling water and the the pump temperature.

The pressure in the main vacuum chamber is monitored by a Veeco RG-75P ionization gauge. The power supply as well as the switching panel for the Hastings gauge, the diffusion pump interlocks and the automatic liquid nitrogen fill system are all designed and constructed by Lawrence Radiation Laboratory.

3. Vacuum Seals and Connections

Rubber O-rings in grooves of standard LRL dimensions are used in most static and all movable vacuum seals. The seal for the 12" diameter rotating lid is provided by a double O-ring groove with a pump out between the grooves; however, it was never necessary to use the pump-out. Rectangular (3/8"×9/16") rubber gaskets serve to seal the large wall flanges. Apiezon

L or N vacuum grease is lightly applied to all O-rings and gaskets; one exception to this is the rotating lid where Dow Corning 33, medium consistency, heat stable low temperature silicone grease is used to insure leak free rotation even when the O-rings are cooled by conduction to the liquid nitrogen tank attached to the lid.

Most electrical feed-throughs are made by drilling holes in epoxy plugs, threading a bare wire through the hole and sealing with epoxy; these epoxy plugs are then sealed with rubber O-rings. Such crude systems give remarkably trouble free performance. For the signal lead a Stupakoff kovar-glass seal is used; 1/4" brass tubes carry both the energizing current and cooling water for the magnets into the chamber. These are sealed at entry to the vacuum by an O-ring; teflon sleeves both inside and outside the vacuum chamber electrically insulate the tubes and define the O-ring groove. Inside the vacuum chamber, connections for the cooling water lines are made with both a well standardized system of the LRL couplings and fittings and Swadgelok fittings; no trouble has been encountered with either system even after repeated resealing.

C. Beam Sources

1. Ovens

The sources of the molecular beams in this apparatus consist of small chambers which contain the molecules at a pressure of up to a few Torr and are equipped with narrow slits. The pressure of the gas and the width of the slit are adjusted so that the mean free path length in the chamber is approximately equal to but not much greater than the slit width; this condition insures that the molecules will leave the sources by molecular

effusion rather than hydrodynamic flow. Under effusive flow conditions the molecules undergo essentially no collisions after they leave the oven while in the latter case a cloud of molecules forms in front of the slit and the boundary of the cloud becomes the effective beam source. When this occurs, the beam broadens, the beam intensity no longer is proportional to the source pressure, and the temperature of the beam is not well defined.[6]

The molecular beam ovens used in this apparatus are of the typical design as described by Ramsey.[6] For the experiments that have been carried out, a double chamber oven was used to produce the Li atom beam; the lower chamber contains the charge of Li metal and its temperature defines the source pressure while the temperature of the upper oven, which can be varied independently from that of the lower, defines the beam temperature. This design permits the achievement of an effusive molecular beam with the kinetic energy variable over a limited range, and allows the minimization of the dimer concentration in the beam. This oven was constructed from stainless steel with welded construction. Although Li slowly attacks stainless steel at the high temperatures required to produce the beam, no serious problem has been encountered; however a slow corrosion of the lower chamber is evident and the tube connecting the two ovens has required replacement. The top of the lower oven, to which the upper oven is connected, is removable to allow refilling of the charge; since copper gaskets could not be used, the lid is lapped and held tightly against a lip around the well in the lower oven by means of a screw mounted on a yoke. This arrangement was found to be satisfactory and did not leak. The tube from the lower to upper oven extends inside the upper oven to above

the level of the slit; this construction insures that the thermal equilibrium is achieved in the upper oven before the gas can leave the slit. The temperatures of the oven chambers are monitored with chromel-alumel thermocouples inserted in wells in the oven blocks. The temperatures were typically 950°K and 1075°K in the lower and upper chambers respectively; at thermal equilibrium, this would correspond to a Li source pressure of ~0.3 Torr, with less than 0.5% Li_2 in the effusing beam. Magnetic deflection typically attenuated the parent Li beam by 99% indicating a negligible concentration of Li_2 in the beam assuming that Li_2 was surface ionized to give Li^+ rather than Li_2^+. An auxiliary experiment, employing velocity and magnetic deflection analysis of the parent Li beam, confirmed that indeed Li_2 did give a surface ionization signal of Li^+ and thus that the Li_2 concentration in these experiments was negligible. Each chamber is heated by 0.020" tantalum wire strung with ceramic beads to provide electrical insulation and wound through holes in the ovens. The power for these ovens, as well as for the other beam source, is supplied by variable, 140V, ac powerstats which are in turn energized by a line voltage regulator. In order to reach the high temperatures required, several layers of 0.001" stainless steel foil surround each oven to serve as heat shields by reducing energy loss through radiation. The lower oven is supported by a 7/8" o.d. stainless steel tube with thin (0.040") walls to minimize heat conduction from the oven. This tube is held by a clamp which is equipped with cooling coils to prevent heating of the surrounding apparatus by conduction from the oven.

Stainless steel foil (.001" thick) is used to define the slit edges of the oven; the foil is held in place with slit jaws and may be adjusted

to any required width. This system results in slits similar to the "ideal slits" described by Miller and Kusch.[7,8]

The non-alkali beam source was designed for use with reagents that have a substantial vapor pressure at room temperature. The reactant gas is prepared on an external vacuum line at the desired pressure (typically ~3 Torr) and a tube provides a connection to the oven. This oven consists of a copper block, encompassing a small volume and equipped with a slit containing a many channel array. The array is of the standard "crinkly foil" construction[9] with characteristics of ~0.012 cm hole radius, ~0.5 cm long and calculated porosity ~90%. Nickel foil has been used and has performed satisfactorily although corrosion is a problem and in the experiments that have been carried out, the foil required periodic replacement. The experimentally measured beam profile was roughly triangular, 13° FWHM which indicates considerable directivity when compared with the geometrically calculated trapezoidal, 19° FWHM beam profile. The heating elements and power supply is similar to that of the double chamber oven; the temperature was typically maintained at 320°K.

2. Cold Shields, Collimating Slits and Beam Flag

A copper cold shield completely surrounds the double chamber oven. This shield is mounted on the liquid nitrogen trap above the ovens which was intended to provide the cooling for the shield; however, it was found that additional water cooling around the lower part of the cold shield was necessary to maintain a low pressure in the system. A large foreslit lets the major portion of the beam through the shield; in order to eliminate troublesome secondary peaks on the beam profile caused by scattering of the beam from the walls of this slit through the cold shield,

it was necessary to bevel the hole on the outside and provide water cooling for this area. A heated, adjustable width collimating slit is mounted on the outside of the cold shield to provide collimation for the beam; the beam profile agrees with geometric calculations and is typically 2° FWHM. In addition to the heat shielding around the oven, further .001" stainless steel foil heat shielding is mounted inside the cold shield.

The cross beam oven is also surrounded by a cold shield mounted on the liquid nitrogen trap. Since only condensable gases are used, this cold shield provides the primary pumping for this source; conduction to the trap cools the shield adequately. Collimation is provided by an unadjustable slit cut into the cold shield; this slit required warming somewhat to prevent clogging. A beam flag, used to interrupt the cross beam, slides along guides built into the cold shield and is connected to a manually operated plunger by a wire coupling; this plunger enters the vacuum through an O-ring seal.

D. Detector Assembly

1. Surface Ionization Detector

A surface ionization detector of the type commonly used in molecular beam work[6] provides sensitive and specific detection of a small class of substances that have low ionization potentials. Additional attractive features of this detector are its linearity of response and simplicity of construction and use.

For the Li atom reactions, a polycrystaline W filament of .003" dia. was used to ionize the reactant metal atoms and the product halide molecules to the singly-charged positive ion of the metal. Due to the high ionization potential of the metals investigated it was necessary

to obtain a surface with as high a work function as possible; accordingly a capillary tube was installed to continuously oxygenate the W surface and the filament was run at a low temperature in order to maintain an oxide coating on the surface.[10,11] In partial agreement with previous work[12] we found that this surface achieved its maximum ionization efficiency and best signal to noise ratio when operated at ~1700°K. The filament is heated by passing a current through it (0.50 amps at 1700°K). Thus current is supplied by Kepco dc power supply (Model 5M 36-5 AM) capable of delivering 0-5 amps at 0 to 36 volts. The filament and its power supply are insulated from ground (rated for 5 kilovolts) to allow the ion source to be maintained at any desired potential. In order to prevent the filament from sagging due to the expansion in length which occurs upon heating, a spring is wound from .010" tantalum wire and spot-welded to one end of the filament. The other ends of the spring and filament are spot welded with the spring stretched to nickel wires which deliver the current and support the filament.

The filament is mounted within a focusing element and an accelerating grid; the design of these three elements is such that they approximately define a "Pierce gun".[13] As indicated in Fig. 1, this assembly ejects the positive ions into the magnetic mass spectrometer at any desired energy. The "Pierce gun" was used because it can be shown by an exact solution of the space-change equations for electrons leaving a space-change-limited cathode that the electron flow is rectilinear;[13] this property is not very critical for positive surface ionization, but future crossed beam studies may be carried out utilizing negative surface ionization in which case space charge limited conditions would exist due to the extraction of

thermal electrons as well as the negatively charged ions. The two elements were constructed from monel metal; they are supported by ceramic rods and electrical contact is made by .020" nickel wires held in place against the elements with tension produced by suitably bending the wires. The potentials of the two elements as well as that of the filament and its power supply are provided by a voltage divider utilizing a Kepco Pax dc power supply capable of delivering 150 ma at 72 volts.

Mass analysis of the surface ionized signal was deemed desirable for two reasons. First, the filaments normally available for use in surface ionization detectors are generally contaminated with small amounts of alkali metals, predominately Na and K. During operation at a high temperature, these impurities boil out of the metal and are ionized, thus causing a large background; mass analysis will eliminate almost all of this when Li or the alkaline earths are being investigated. Second, if negative surface ionization is contemplated, at least a crude method of mass analysis is a necessity in order to eliminate the thermal electrons that are unavoidedly extracted from the ionizing surface along with the negative ions. A very simple and easily fabricated mass spectrometer is simply a magnet with a strong field and circular pole tips. By injecting all ions at the same energy, they are bent in circular paths whose radii are a function of the momentum of the ion. Thus, particles of different mass travel different paths and by suitably locating an exit slit with shielding to collect all ions not reaching the slit, mass analysis is accomplished.

In this apparatus, the ions are mass analyzed in a 2.5 cm radius electromagnet[14] with a 0.79 cm gap. Two features of this magnet

(as well as that of Geise and Maier) deserve comment. The two round poles each have shims in the shape of rings such that they extend .0381 cm away from the pole face and in .0495 cm toward the centers from the outside radius. These shims are designed to minimize inhomogenity[15] of the magnetic field due to "fringing " of the field at the edges. Secondly, the circular pole faces in conjunction with the 90° angle of deflection insure the acceptance of a moderately divergent beam; it has been shown[16] that the beam is focused in angle to second order for such a configuration.

The magnet yoke is fabricated from Armco Magnetic Ingot Iron; Western Electric Permendur was used for the pole pieces. All pieces were plated with .001" nickel to minimize corrosion. The current to energize the magnet is carried by one hundred seventeen windings of 1/8" o.d. soft copper tubing capable of carrying 100 amps with an IR drop of approximately 27 volts. Cooling is provided in the vacuum by running water through the tubing; the water is warmed during its passage through the coils, but no overheating problems have been encountered whenever the operator has mememberred to turn on the water. Insulation is provided for the coils by inserting the copper tubing in fiberglass sleeving before winding the coils. A Universal Electronics transistorized dc power supply capable of delivering 0-15 amps at 0-10 volts provided the energizing current during the Li atom experiments.

The windings were designed to allow the achievement of a magnetic field of 15 kilogauss at 100 amps. No exhaustive calibration was attempted but crude measurements showed 3.8 kiloguass at 25 amps energizing current when only half the windings were used. Measurements taken immediately

outside the gap indicated less than 200 gauss fringing field. The mass spectrometer has proven itself capable of selecting down to at least atomic mass 6; lithium 6 and 7 are clearly separated at maximum resolution. The highest mass selected has been thallium; no attempt was made to separate Tl 203 from Tl 205.

Outside the exit slit (0.10cm × 0.64cm) is mounted a resistance strip electron multiplier (Model M-306, Bendix Corporation, Cincinnati, Ohio) for detection of the ions. This multiplier showed no deterioration after repeated low-pressure exposures to the alkali metal and halogen vapors employed in these experiments. The gain of the multiplier was changed, however, when the deflecting magnet was energized; in order to avoid this, a magnetic shield was fabricated from .062" thick Mu-Metal. This shield had the added benefit of providing electrical shielding which prevented the detection of background ions produced on the heating elements of the ovens. The lead from the anode of the electron multipler is fed through a kovar-glass seal and the current is measured with a Cary Model 31 vibrating reed electrometer and recorded on a Leeds and Northrup Speedomax. G recording potentiometer.

This assembly of the surface ionization filament, mass spectrometer and electron multiplier as well as surrounding electronical shielding are insulated from ground so that the whole system may be biased up to 5 kilovolts from ground. This feature is necessitated by the desire to use this detector for negative surface ionization; in order for the anode of the electron multiplier to be held at ground, as is required by the Cary electrometer, the cathode must be held at voltages as much as two kilovolts negative. In order to accelerate the negative ions

into this cathode, the surface ionization filament, the mass spectrometer, and surrounding electrical shielding must be held at roughly 2 kilovolts more negative. This insulation is provided simply by mounting the complete system on a plexiglass plate. One is limited to .003 or smaller diameter surface ionization filaments, though, because larger filaments radiate enough heat to eventually melt the plexiglass. Teflon sheet between the mass spectrometer yoke and the energizing coils allow the magnet's power supply to be operated at ground. However, the power supply producing the potentials for the mass spectrometer elements and the power supply for the filament current must, of course, be insulated from ground by means of 5 kilovolt isolation transformers. A John Fluke Mfg. Co. Inc., Model 408B high voltage dc power supply (0 to 6 kV, 0 to 20 ma) in conjunction with a voltage divider system provide the potentials for the electron multiplier and the potentials for floating the various power supplies and apparatus components.

The plexiglass plate is mounted on a sliding flange that may be moved in a horizontal direction from outside the vacuum chamber. The position of the flange is monitored to within .001" by a Lufkin dial indicator (1" full range, 10 cycles of the dial). This feature is necessary so that the detector assembly may be scanned across the gap of the deflecting magnet allowing beam profiles and deflection patterns to be measured. In order to eliminate errors due to backlash, the flange is always scanned in the same direction.

2. Deflecting Magnet

Since positive surface ionization produces the singly charged positive metal ion from both the reactant metal atoms and the product halides, a

means of distinguishing between the signal due to each of the two species must be included in the experiment. Two filament differential surface ionization takes advantage of the fact that while tungsten and most other filament materials ionize the alkali atoms and their halides with equal efficiences, an alloy of platinum with 8% tungsten which has been treated by heating in the presence of methane will ionize only the metal, remaining insensitive to the halide even in the presence of halogens.[17] A previous surface ionization study[18] has indicated that differential surface ionization might also be used to distinguish Li from LiX. However, the differential surface ionization detection technique proved impractical in this study due to the extremely poor ionization efficiency of Li atoms on a "methanated" Pt-8% W surface.

An alternative means of differentiating between the reactant and the product is to avail oneself of the different behavior of the two species in an inhomogeneous magnetic field. In the alkali atom systems the ground state of the alkali atoms is $^2S_{1/2}$; none of the excited states of the alkali halides is energetically accessible, so all of the product molecules must be in the $^1\Sigma^+$ ground state. Thus, if the scattered species are passed through an inhomogeneous magnetic field before reaching the detector, the halide will be unaffected, but the spin of the atom will intereact with the field, causing a deflection of the atoms away from the ionizing filament. In practice in this apparatus the deflection is not complete, but the fraction deflected is known. Figure 3a shows the undeflected beam profile and the corresponding deflection pattern. The detector is held at a displacement equal to zero during an experiment. Thus, the maximum fraction deflected is as high as 99%. Figure 3b indicates

that the transmission through the magnet decreases rapidly with increasing energizing current until it almost reaches zero at the maximum current.

The alkaline earth reactions with halogen containing compounds present a somewhat different picture. The ground states of the atom and the halide are $^1S_0$ and $^2\Sigma^+$ respectively; therefore the elastically scattered atoms are unaffected by the field, but the product halide would be deflected. Since the distance of deflection is proportional to the square of the time that the molecule spends in the field, which in turn is inversely proportional to the velocity of the molecule, it should be possible not only to measure the angular distributions of the elastically scattered atoms and the reactively scattered halides separately, but also to extract the velocity distribution of the product by measuring the deflection patterns. Unfortunately, these experiments have not yet been attempted.

An additional advantage of magnetic deflection analysis over two-filament differential surface ionization has become apparent in a recent investigation[19] which showed that the detection efficiency of the "methanated" surface is not zero for internally excited alkali halides, and in fact, appears to approach 15% for KI with 1.9 eV internal excitation. Such residual detection would yield anomalously low values for the intensity of the reactive scattering. In the method presented here the single W filament has been shown[2b,18] to ionize Li and LiX with essentially equal efficiencies. Thus, the above ambiguity is avoided.

The inhomogeneous electromagnet[20,21] used in the apparatus was designed so that the poles conform to the traditional "two wire" form;[6] the advantage of this configuration is that the mathematical treatment

Figure 3(a). Beam profile at zero field calculated from nominal slit geometry (dashed trapezoid) compared with measured beam profiles from parent Li beam (open circles) and scattered signal at 20.8° (triangles). The peaks of the beam profiles were normalized to 1.0. The parent beam Stern-Gerlach deflection pattern (multiplied by a factor of 5.26) obtained with an energizing current of 96A is also shown (solid circles).

(b). Signal reaching detector at zero detector displacement as a function of the magnet energizing current.

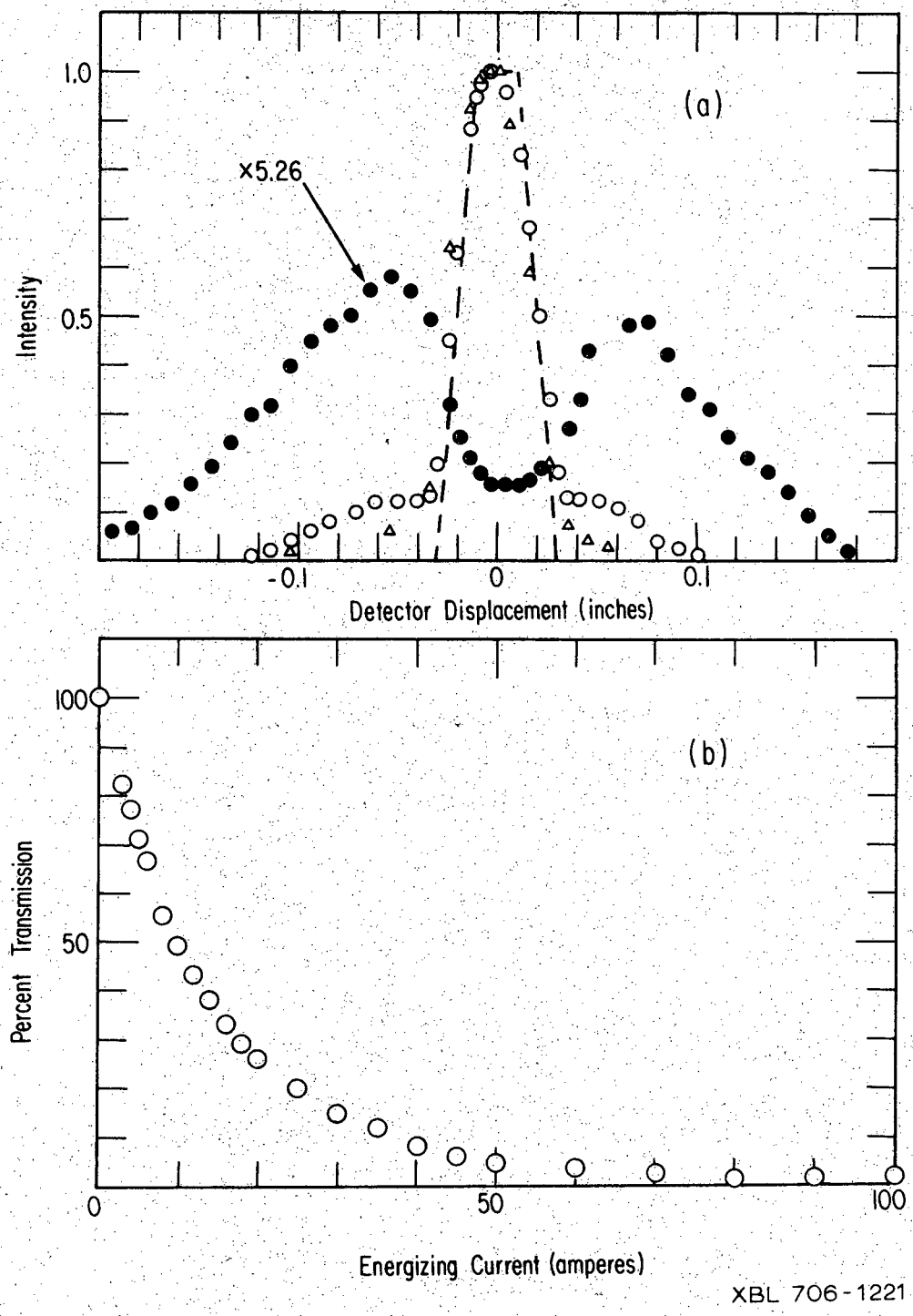
1.0
0.5
Intensity
(a)
×5.26
-0.1
0
0.1
Detector Displacement (inches)
100
50
Percent Transmission
(b)
0
50
100
Energizing Current (amperes)
XBL 706-1221

Figure 3

of the magnitude and gradient of the field (which is relatively tractable) shows that these two field characteristics are almost uniform over the beam height. Ramsey (Ref. 6) gives a full discussion of these magnetic fields. The approximate magnitude of the field is 15 kG with a gradient of about 90 kG/cm at maximum energizing current (100 amps).

The construction of this magnet is very similar to that of the mass spectrometer magnet. Armco Magnetic Ingot Iron is used in the fabrication of the yoke, while the pole pieces are constructed from Western Electric Permendur. Each piece has received a .001" nickel plating. The current coils are also similar: 36 turns of 1/4" copper tubing carry up to 100 amps dc current and cooling water; electrical insulation is provided by fiberglass sleeving. Ten volts are required to supply the maximum current; this power is supplied by Kepco Model KQ 12-100M regulated dc power supply capable of delivering 0-100 amp at 0-12 volts.

The entire magnet assembly is shielded in such a way that only species scattered out of the collision volume defined by the two intersecting beams can reach the detector. In front of the magnet are placed two slits (each 0.024 cm wide and 0.24 cm high); these two slits are spaced 10.2 cm apart and therefore insure a very narrowly collimated beam of scattered species entering the magnet. It is essential that, with the magnet off, the profile of the beam transmitted though the magnet be independent of the viewing angle θ; marked changes in the effective deflecting power of the magnet would occur if the beam profiles change. Figure 3(a) shows a typical check of this requirement. The profile of the parent beam exhibits wings on either side which are of undetermined origin; they were later greatly reduced by improved shielding. The

Stern-Gerlach deflection pattern also shown in Fig. 3(a) as well as the plot of the magnet transmission as a function of the magnet current in Fig. 3(b) indicates the effect of these wings was negligible. Ultimately, 99% deflection of the parent beam has been achieved. These wings are absent in the scattered signal profiles, and only a negligible broadening of the wings of the profile produced by collisions with the ambient background gas after passage through the first collimating slit (due to the continuous oxygenation of the W filament and outgassing of the high temperature oven the apparatus pressure was typically $\sim 1.5 \times 10^{-6}$ Torr) is observed. For angles within the profile of the gas beam, a higher background pressure is produced within the deflecting magnet collimating slit assembly. This produces a pressure broadening of the undeflected beam profile of the scattered signals for this range of Θ thereby producing an angle dependent transmission function.[22] This transmission function is determined periodically by measuring the transmission versus Θ of a Li-atom beam which has been scattered from the non-reactive gas, cyclohexane. One other feature of Fig. 3(a) deserves comment: the center of the undeflected beam is at a slightly negative detector displacement while the center of the deflection pattern is at a slightly positive displacement. This phenomenon is caused by a small shift of the slit assembly when the magnet is energized; the magnitude of this shift is so small (~.010") that it's effect is negligible.

A further complicating factor of this magnetic deflection analysis technique is that the detector sees only a small part of the collision zone and thus detects only a fraction of the scattered products. Since the collision zone is not cylindrically symmetric, this fraction varies

with observation angle. Consequently, it is necessary to measure the total scattering with the magnet removed from the path of the scattered species and then with the magnet in place, to determine the fraction of the scattered signal due to diamagnetic product. When the apparatus was originally designed, it was intended to have the magnet mounted so that it could be raised into the lowered out of the beam path. Due to lack of reproducibility of the magnet position, this design feature had to be abandoned; therefore, two separate experiments (with and without the magnet) must be run. In practice, the data analysis is carried out by multiplying the angular distributions measured with the magnet in place by an angle dependent viewing factor defined as

$$V(\Theta) = \frac{\text{Total scattering volume}}{\text{effective scattering volume seen by the detector}}$$

Theoretical values of $V(\Theta)$ calculated from slit geometries and from experimentally determined beam profiles are indicated in Fig. 4; these calculated values of V are almost symmetric about $\Theta = 0^\circ$ and $\Theta = 90^\circ$. These data indicate the importance of this correction, since V varies over a factor of 5 to 10 as Θ goes from 0° to 90°. However, these theoretical values of $V(\Theta)$ are not used for the data analysis; rather, values are determined individually for each reaction system from the two separate experiments mentioned above. In this case $V(\Theta)$ is given by the ratio of the signal without the magnet to the signal with the magnet in place but not energized. Figure 4 indicates that the average of these measured values of $V(\Theta)$ does agree roughly with the theoretical value. The lack of symmetry about $\Theta = 90^\circ$ as well as the large standard deviation in the measured $V(\Theta)$ curve are thought to arise from small, random, and incon-

sequential misalignments of the deflecting magnet collimating slits with respect to the center of the rotation of the oven assembly (COR). The departure of the experimental and calculated V (Θ) curves at small LAB angles is thought to be a resolution effect which arises because removal of the magnet slits reduces the effective angular resolution of the parent Li beam considerably, and thus alters the form of the small angle elastic scattering intensity.

Physically, the magnet is mounted on a platform whose height may be adjusted to allow proper alignment of the magnet. The detector system as well as the oven assembly is aligned by means of an optical cathetometer.

E. Preliminary Experiments

As a check of the techniques employed in this study against the more conventional two-filament differential surface ionization studies, the angular distribution of NaBr formed in the scattering of Na from Br_2 was measured. Comparison with the data of Ref. 3 is shown in Fig. 5 the overall shape of the curve as well as the peak position is well reproduced. This calibration experiment was run before certain modifications were incorporated to improve the signal to noise ratio in the apparatus; for this reason, the data in Fig. 5 are noisier and restricted to a narrower range of Θ values than are the data reported for the Li reactions.

Figure 6 shows the primary data for Li + Br_2 collected during three different experiments, at different absolute signal levels. The agreement in the small angle region between results of different experiments, the agreement between calculated and experimental viewing factors shown in Fig. 4, the calibration data shown in Fig. 5 and comparisons of the experimental and theoretical small angle elastic scattering angular

Figure 4. Plot of viewing factor (ratio of total collision volume to that seen by the detector) against Θ. The circles give calculated values of $V(\Theta)$ based upon the Li beam profile predicted by slit geometry and two gas beam profiles: (1) the profile calculated from slit geometries (open circles) and (2) a typical measured profile (13° FWHM; dark circles). The squares are experimental values of $V(\Theta)$ determined by averaging $V(\Theta)$ values measured during about twenty-five separate studies of the scattering of Li from various gases; the error bars give the standard deviations of these average values. The circles are normalized to the squares to give the best overall fit.

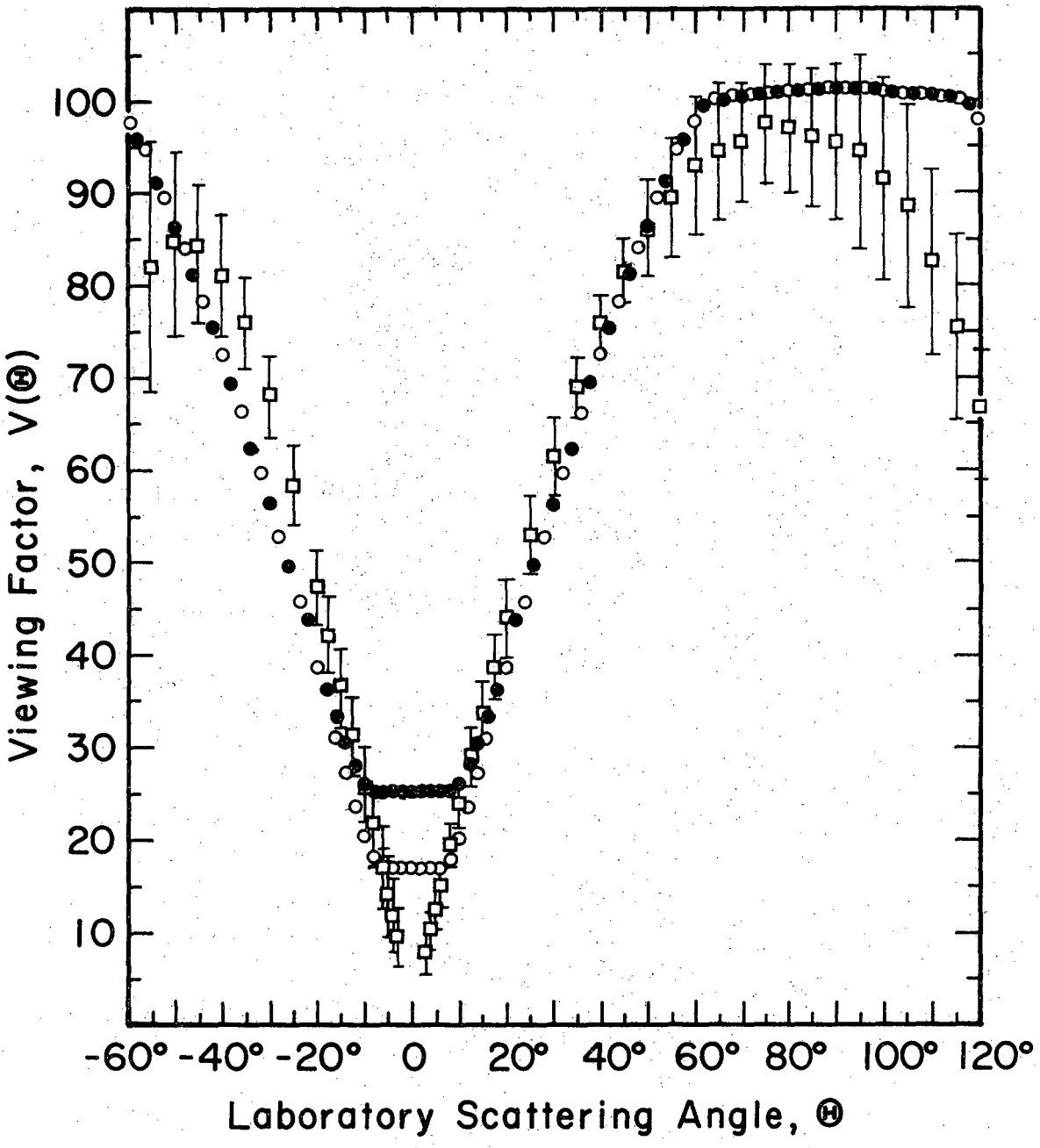

Figure 4

XBL 689-5827

Figure 5. Comparison of the angular distribution of NaBr from Na + Br_2 measured in this work by magnetic deflection analysis (open circles) normalized to the more conventional two-filament differential surface ionization results reported in Ref. 3 (dark circles).

Figure 6. Primary data for Li + Br_2, corrected for the viewing factor. The x's show the total intensity at zero magnetic field. Also shown are data for the transmitted intensity at high field (◇, ▽, ●) for three separate experiments and the derived nonreactive Li signal (□, ▲, ○ connected by the solid curve).

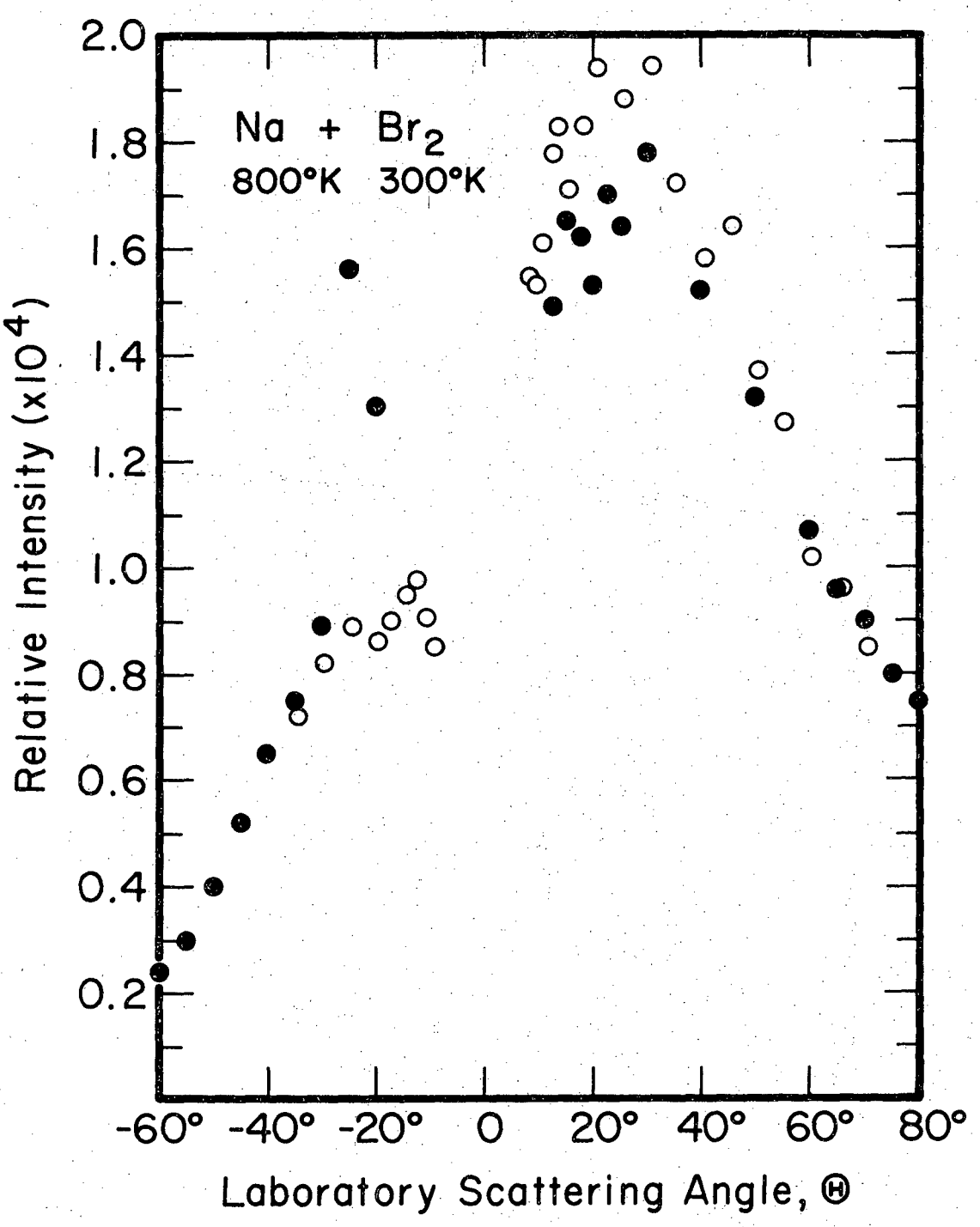

XBL 689-5828

Figure 5

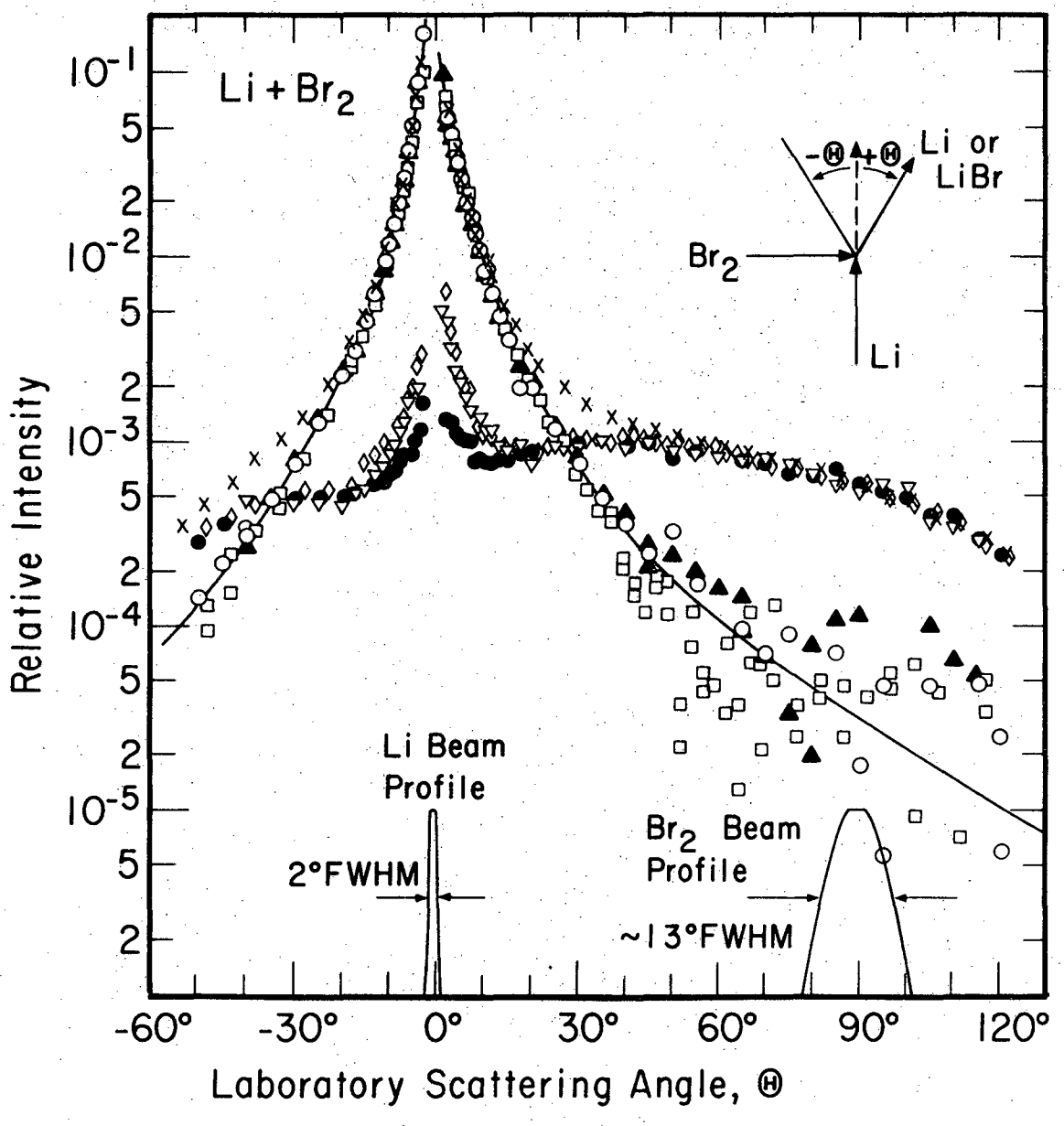
Li + Br2
Li or LiBr
Br2
Li
Relative Intensity
Li Beam Profile
2°FWHM
Br2 Beam Profile
~13°FWHM
-60°
-30°
0°
30°
60°
90°
120°
Laboratory Scattering Angle, Θ
XBL 6812-6449

Figure 6

distribution given in Ref. 26 all indicate an absence of any appreciable non-linear detector response. The lack of precision in the wide angle non-reactive scattering data shown in Fig. 6 illustrates one of the handicaps of the magnetic deflection analysis technique. In the study of scattering partners with large reactive cross sections, the wide angle elastic scattering is severely attenuated by reaction and is much smaller than the reactive scattering at these large angles; consequently, the signal with the magnet on differs only slightly from when the magnet is off. In this case small errors in individual determinations of deflected and undeflected signals can result in a very large uncertainty in the derived non-reactive scattering intensity. For this reason, the derived non-reactive scattering distribution shown in Fig. 6 is of limited quantitative use, but does indicate that the predominant scattered species at wide laboratory angles is LiBr rather than Li. The complete results for Li + Br_2 as well as Li with Cl_2, ICl, $SnCl_4$ and PCl_3 have been given in Ref. 2. The reactions of Li with NO_2, CH_3NO_2, CH_3I, SF_6, and CCl_4 are discussed in the next chapter.

REFERENCES

1. See, for example, the following reviews: (a) D.R. Herschbach, Adv. Chem. Phys. 10, 319 (1966); (b) E.F. Greene and J. Ross, Science 159, 587 (1968); (c) J.P. Toennies, Ber. Bunsenges. Physik. Chem. 72, 927 (1968).
2. Preliminary results of the first five Li atom reactions have been reported in: (a) D. D. Parrish and R.R. Herm, J. Chem. Phys. 49, 5544 (1968); and a complete discussion has appeared in:(b) D. D. Parrish and R. R. Herm, J. Chem. Phys. 51, 5467 (1969). The remaining five reactions will be discussed in a later chapter.
3. J. H. Birely, E. A. Entemann, R. R. Herm, and K. R. Wilson, J. Chem. Phys. 51, 5461 (1969).
4. R. J. Gordon, R. R. Herm, and D. R. Herschbach, J. Chem. Phys. 49, 2684 (1968).
5. A. Guthrie and R. K. Wakerling, ed., Vacuum Equipment and Techniques (McGraw-Hill, New York, 1949) p. 51.
6. N. F. Ramsey, Molecular Beams (Oxford University Press, London, 1963) p.11.
7. R. C.Miller and P. Kusch, Phys. Rev. 99, 1314 (1955).
8. R. C. Miller and P. Kusch, J. Chem. Phys. 25, 860 (1956).
9. H. Pauly and J. P. Toennies, Advan. At. Mol. Phys. 1, 195 (1965).
10. S. Datz and E. H. Taylor, J. Chem. Phys. 25, 389 (1956).
11. S. Datz and E. H. Taylor, J. Chem. Phys. 25, 395 (1956).
12. S. G. Andresen and C. A. Shipley, Rev. Sci. Instr. 36, 858 (1965).
13. J. R. Pierce, Theory and Design of Electron Beams (D. Van Nostrand Co., Inc., Princeton, N.J. 1954) p. 174.
14. This mass spectrometer is patterned after that described by: C. F. Giese and W. B. Maier, II, J. Chem. Phys. 39, 739 (1963).

15. M. E. Rose, Phys. Rev. 53, 715 (1938).

16. H. Hintenberger, Rev. Sci. Instr. 20, 748 (1949).

17. F. R. Touw and J. W. Trischka, J. Appl. Phys., 34, 3635 (1963).

18. K. R. Wilson and R. J. Ivanetich, UCRL Rept. 11606 Lawrence Radiation Laboratory, Berkeley, 1964.

19. K. T. Gillen and R. B. Bernstein, Theoretical Chemistry Institute, University of Wisconsin, Report No. WIS-TCI-377X (1970); J. Chem. Phys. (to be published).

20. This magnet w s almost identical to that described in: M.A.D. Fluendy, R. M. Martin, E. E. Muschlitz, Jr., and D. R. Herschbach, J. Chem. Phys. 46, 2172 (1967).

21. Details of the magnet of Ref. 12 as well as a full calibration have been given in: R. R. Herm and D. R. Herschbach, UCRL Rept. 10526, Lawrence Radiation Laboratory, Berkeley, 1962.

22. Even in the absence of this pressure broadening effect, the transmission would be expected to vary slightly with Θ because the laboratory energy of elastically scattered Li varies with Θ; this effect is analyzed in Ref. 4.

APPENDIX A

LIST OF APPARATUS DRAWINGS AND UCRL NUMBERS*

1. Vacuum Chamber

Main Chamber	12M 9426
Rotating Lid	12M 9414
Large Front Flange	12M 9394
Large Front Flange (with mounting holes drilled and tapped)	12N 3653
Small Side Flanges	12M 9384
Small Side Flange (with 3-3/4" port)	12N 3673
Small Side Flange (with sliding flange port)	12N 3663
Medium Back Flange	12M 9374
Medium Back Flange (with 3-1/2" port)	12N 1442
Ion Guage Flange	12M 9342
High Temperature Oven Flange	12M 9353
Fixed-Length Oven Mount	10J 6893

2. Liquid Nitrogen Traps and Cold Shields

Large Liquid Nitrogen Trap Stand	12M 9494
Large Liquid Nitrogen Trap	12M 9484
Large Liquid Nitrogen Shield Chassis	12M 9464
Large Flange Liquid Nitrogen Shield	12M 9474
Oil Diffusion Pump Baffles	12M 9453
Small Flanges Liquid Nitrogen Shields	12M 9443
Medium Flange Liquid Nitrogen Shield	12N 1452
Large Trap Fill Tube	12M 9363
Large Trap Support Straps	12M 9432
Rotating Lid Liquid Nitrogen Trap	12M 9404

3. Ovens

High Temperature Oven-Lower Chamber	12M 9241
High Temperature Oven-Upper Chamber	12M 9251
Upper Chamber Clamp	12M 9261

3. Ovens (continued)

Laval Slit	12N 1411
High Temperature Oven Clamp	12M 9181
Gas Oven	12M 3552
Gas Oven Support Tube	12M 3811
High Temperature Oven Slit Jaws	12M 4491

4. Oven Cold Shields

High Temperature Oven Cold Shield	12N 0303
High Temperature Oven Cold Shield Supports	12N 0252
Gas Oven Upper Cold Shield	12N 0293
Gas Oven Lower Cold Shield	12N 0221

5. Mass Spectrometer and Surface Ionization Assembly

Ion Lens	12N 0191
Ion Focusing Element	12N 0201
Surface Ionization Detector Support and Mass Spectrometer Shield	12N 0242
Mass Spectrometer Magnet Yoke Base	12M 9282
Mass Spectrometer Magnet Yoke Sides	12M 9292
Mass Spectrometer Magnet Poles	12M 9271
Mass Spectrometer Magnet Lift Plates	12N 0211
Electron Multiplier Mount	12N 1331
Mass Spectrometer Magnet Mount	12N 0273
Mass Spectrometer Support Plate	12N 0283
Rotating Lid Mass Spectrometer Mount	12N 1321
Rotating Lid Surface Ionization Assembly Mount	12N 1311
Rotating Lid Mass Spectrometer Exit Slit Mount	12N 1301
Rotating Lid Detector Mount Plate	12N 1473

6. Sliding Flange

Sliding Flange	12N 0263
Sliding Flange Mount Bars	12N 0181

7. Deflecting Magnet

Deflecting Magnet Yoke - Base	12M 9312
Deflecting Magnet Yoke - Sides	12M 9302
Deflecting Magnet - Yoke to Pole Adapters	12M 9322
Deflecting Magnet Poles	12M 9332
Deflecting Magnet Pole Clamps	12M 9221
Primary Slit Mount	12M 9171
Primary Slits	12M 9231
Secondary Slit Mount	12M 9211
Deflecting Magnet Support	12N 0161
Deflecting Magnet Support Rods	12N 0141
Deflecting Magnet Support Bars	12N 0151
Deflecting Magnet Thrust Bar	12N 1361
Deflecting Magnet Forward Guide	12N 0232
Deflecting Magnet Support Shelf	12N 0323
Deflecting Magnet Flange	12N 1462
Magnet Mount	12N 3643

8. Miscellaneous

High Temperature Oven Collimating Slit	12N 1431
High Temperature Oven Beam Flag	12N 1341
Gas Beam Flag	12N 1421
Gas Beam Flag Sliding Seal	12N 1351
Rotating Gas Line Seal	12N 1371
Modified UCRL Fitting for Electrically Insulated 1/4" Vacuum Seal	12M 4681
Inner Sleeve for 1/4" Seal	12M 4671
Outer Sleeve for 1/4" Seal	12M 4661
Vernier Scale for Rotating Lid	10J 6632

*Copies of UCRL drawings whose numbers are cited here and throughout this thesis may be obtained (for a nominal fee) by writing to: Lawrence Radiation Laboratory, Technical Information, Building 90, Room 1046, Berkeley, California, 94720.

APPENDIX B

LIST OF APPARATUS ELECTRONICS DIAGRAMS AND UCRL NUMBERS

System Wiring Diagram	8S 6475
Liquid Nitrogen Level Control	8S 4362
Single Vacuum Interlock	8S 2803-1
Hastings Guage Dual Vacuum Interlock	6Z 4664
Dual Vacuum Control Power Interlock	8S 5754A
11 Position Hastings Guage Panel	6Z 3604C
Ion Guage Switch Panel	8S 7392
Voltage Divider	8S 6193
Model 30/31 Electrometer Output Control	8S 6323
Model 31 Electrometer (Applied Physics Corp.)	6Z 3434

III. MOLECULAR BEAM KINETICS II. MAGNETIC DEFLECTION ANALYSIS OF REACTIONS OF Li WITH NO_2, CH_3NO_2, SF_6, CCl_4, and CH_3I.*

A. Abstract

Thermal energy crossed molecular beam studies have been made of the reactions of Li with NO_2, CH_3NO_2, SF_6, CCl_4 and CH_3I. An inhomogeneous deflecting magnet between the collision zone and detector was used to distinguish elastic scattering of Li from reactive scattering of LiX. The total reaction cross sections and the reactive attenuations of the wide-angle Li elastic scattering for all of these gases are considerably smaller than are the corresponding features previously reported for the reactions of Li + XY (XY = Cl_2, Br_2 and ClI). However, interesting differences are observed in the LiX center-of-mass (CM) angular distributions for the five gases studied here. The LiO product of the NO_2 reaction is more sharply peaked in the direction of the Li atom than are the corresponding LiX products of the Li + XY reaction. The $LiNO_2$ and LiF products of the CH_3NO_2 and SF_6 reactions exhibit very broad, almost isotropic CM angular distributions. The LiCl and LiI products of the CCl_4 and CH_3I reactions are predominantly scattered into the backward hemisphere in the CM coordinate system. The features of the NO_2 reaction are discussed in terms of the electron transfer mechanism which has been advanced to account for the features of the reactions of the alkali atoms with the halogen molecules.

B. Introduction

This paper describes our continuing[1] crossed molecular beam studies of Li atom reactions and presents results obtained from angular distribution

*Preliminary version of paper to be submitted to Journal of Chemical Physics.

measurements for the reactions of Li with NO_2, CH_3NO_2, SF_6, CCl_4 and CH_3I. These five reactants have been found to span a wide range of chemical behavior. As a consequence of the high electron affinity of NO_2 and the resultant formation of NO_2^-, a stable negative ion,[2] the reaction with NO_2 promised to be especially interesting. This situation should provide a further test of the electron transfer mechanism which has been advanced to explain the features of the alkali atom-halogen molecule reactions. These reactions are characterized by scattering of the product predominately into the forward hemisphere with respect to the approach of the attacking alkali atom; this behavior has been phenomenologically labeled "stripping." A recent investigation[3] has yielded a limited amount of information concerning the characteristics of the reactive scattering of the four heavier alkali atoms from NO_2, but the present work represents the first measurement of a product angular distribution. Studies of the K, Rb, and Cs+CH_3I reactions yielded the first measurements of product angular distributions from crossed molecular beams,[4,25] and indeed, proved to be prototype examples of a so-called "rebound" reaction where the product MX rebounds opposite to the direction of the incoming M reactant. A later study[5] indicated similar characteristics for the Na+CH_3I reaction. The Cs+CCl_4 reaction was the first chemical reaction of neutral species to be observed in a molecular beam experiment.[6] Crossed beam product angular distribution measurements of the K, Rb, and Cs+CCl_4 reactions[7] indicated that these reactions are intermediate in behavior between the rebound and stripping reactions; also velocity analysis[19] indicates that these are the first neutral systems to exhibit significant coupling between the product angular and translational energy distributions. A series of investigations

of the $Cs+SF_6$ reaction[8] has recently shown that the product translational, rotational, and vibrational energy distributions as well as the angular distribution are all consistent with a collision complex reaction model; the diversity of the methods employed and the quality of the results obtained perhaps establishes this system as the most completely investigated chemical reaction mechanism. A previous crossed beam study of the $K+CH_3NO_2$ reaction[3] yielded the only reported case of a neutral reaction producing a practically isotropic product angular distribution.

C. Experimental Conditions

Only a brief description of the apparatus and experimental procedures will be given here; details are included in Part I.[9] The two beams were crossed at an angle of 90° with their full thermal velocity distributions. The Li beam was prepared by thermal effusion from a conventional two-chamber oven source with standard knife-edge slits; the Li_2 concentration in the beam was negligible. The reactant gas was prepared on an external line at the desired pressure and emerged from a variable temperature, "crinkly foil" many channel source.

The angular distributions of scattered Li and LiX were measured by surface ionization on a continuously oxygenated W filament; only scattering in the plane of the reactant beams was measured. Arguments presented in Part I indicate that this W surface ionized Li and LiX with very nearly equal effeciencies. When energized, an inhomogenous electromagnet placed between the collision zone and detector deflected aside a known fraction of the Li atoms, thereby providing a measure of the scattered Li and LiX separately.

Correction was made for the fact that the measured angular distributions were distorted by the angle dependent fraction of the collision zone seen by the detector through the collimating slits of the magnet (the viewing factor correction discussed in Part I); the experimentally determined correction factor was in all cases in satisfactory agreement with that calculated from the slit geometry. Each scattered signal was plotted as a relative intensity, a dimensionless quantity which is defined as the measured scattered intensity divided by the attenuation of the Li beam produced by the cross beam. Experiments were always run at a relative Li beam attenuation of less than 10%. The measured laboratory (LAB) angular distributions are shown in Fig. 1.

D. Results and Kinematic Analysis

1. Elastic Scattering

Figure 2 shows the center-of-mass (CM) elastic scattering of Li atoms obtained by transforming the LAB angular distributions by the conventional procedure[10] of assigning to the two scattering partners their most probable source velocities and assuming that all non-reactive scattering was due to elastic collisions. As Fig. 2 indicates, the two CM branches do give the same intensity, except at points obtained by transforming wide negative LAB angles where the approximate transformation procedure employed is known to be especially bad. With the exception of the NO_2 case, the wide-angle Li elastic scattering produced by the reactive gases is less than that produced by cyclohexane. This attenuation of the elastic scattering is a well known phenomenon and is generally interpreted as a depletion of the Li scattering due to reaction[11]; however, the reactive attenuations shown in Fig. 2 are appreciably less than those reported in Part I for the

Figure 1.

Measured LAB angular distributions derived by magnetic deflection analysis and corrected for the viewing factor. The X's show the total scattered intensity (Li + LiX); the circles show the derived Li intensity. The solid lines indicate the "smoothed" Li angular distributions.

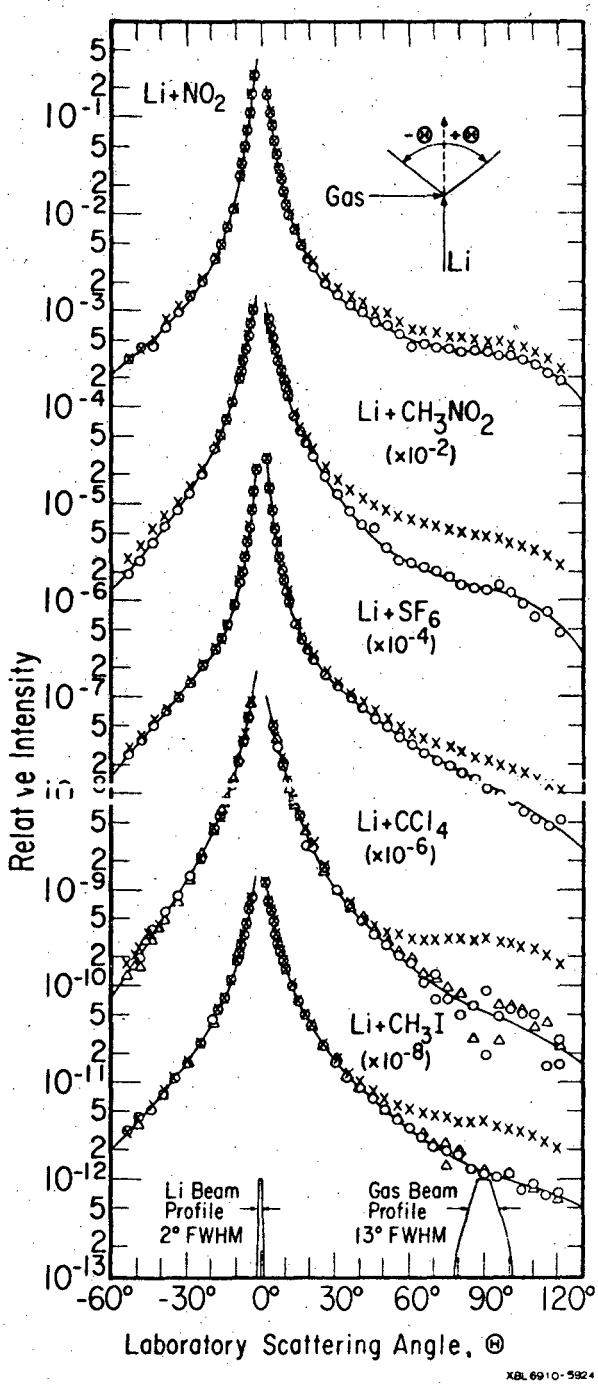
Li+NO2
Gas
Li
Li+CH3NO2
(×10-2)
Li+SF6
(×10-4)
Li+CCl4
(×10-6)
Li+CH3I
(×10-8)
Li Beam
Profile
2° FWHM
Gas Beam
Profile
13° FWHM
Relative Intensity
-60° -30° 0° 30° 60° 90° 120°
Laboratory Scattering Angle, Θ
XBL 6910-5824

Figure 1

Figure 2.

Plot of CM angular distributions (plotted as $I(\theta)$ sin θ) for the elastic scattering, derived by transforming the smooth solid curve fits to the LAB data for Li scattering shown in Fig. 1; data taken from the LAB curves at 5° intervals were transformed. The open circles were obtained from LAB data with $\Theta > 0°$, the dark circles from LAB data with $\Theta > 0°$. The data were linearly extrapolated to $\theta = 180°$ (dotted lines). Data for the scattering from Li+ cyclohexane not shown in Fig. 1 were also transformed; the derived CM angular distribution is shown as the dashed lines. The Li+ cyclohexane data were normalized to the Li scattering produced by each of the reactive gases at narrow angles ($0 < \theta < 10°$) by normalizing each curve to the small angle form factor given in Eq. (16) of Part I.

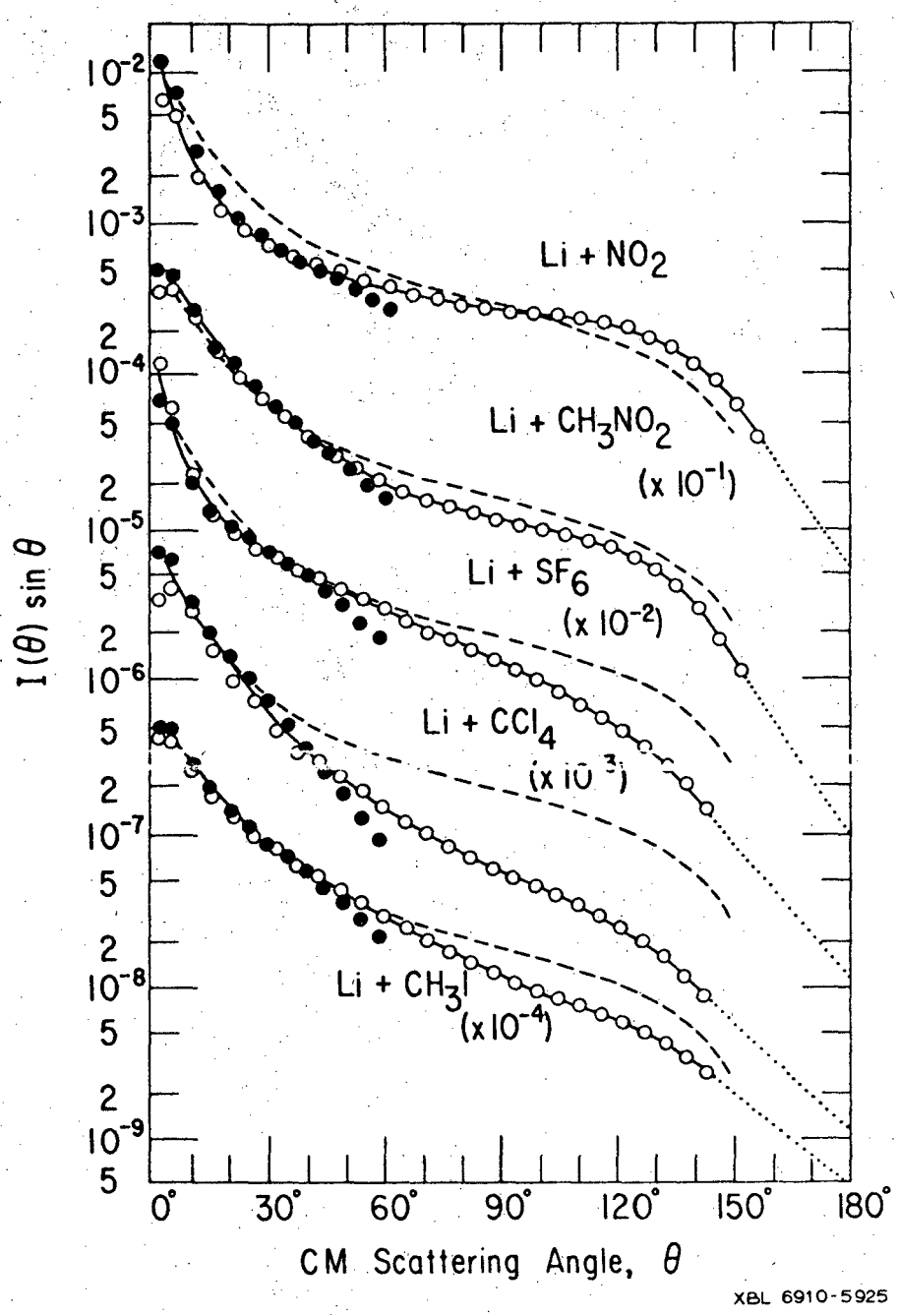
Li + NO2
Li + CH3NO2
(x 10-1)
Li + SF6
(x 10-2)
Li + CCl4
(x 10-3)
Li + CH3I
(x 10-4)
I(θ) sin θ
CM Scattering Angle, θ
0°
30°
60°
90°
120°
150°
180°
XBL 6910-5925

Figure 2

reaction of Li with halogen molecules. A particularly interesting feature is that NO_2 apparently produces more wide angle Li scattering than does cyclohexane.

2. Reactive Scattering

Figures 3-7 show the LAB angular distributions of the halide, oxide, and nitrite products (arguments concerning product identities will be presented later.) The error bars indicate only the uncertainty introduced by errors in the determination of the transmission of the Li atoms through the magnetic field; this is the primary source of error near the primary beam but other inaccuracies certainly dominate at wide angles. Also shown are kinematic diagrams indicating LiX recoil velocities for some of the possible final relative translational product recoil energies, E'. The total energy available to the products must be partitioned between E' and internal excitation W' and is given by

$$E' + W' = E + W + \Delta D_0,$$

where $E = \mu V^2/2$ is the initial relative kinetic energy, W is the initial thermal internal excitation of the reactant gas, and ΔD_0 is the difference in LiX and R-X bond dissociation energies.

Figures 3-7 also show the calculated[12] distributions in centroid angles, for an energy independent collision cross section, resulting from the thermal velocity distributions in both beams. These figures indicate that for NO_2 most of the product appears in the LAB to the left of the centroid distribution; for CH_3I and CCl_4 the product is scattered predominantly into angles to the right of the centroid distributions; whereas for CH_3NO_2 and SF_6 there are appreciable product intensities on both sides of the centroid distributons. These qualitative observations indicate that

the Li+NO_2 product predominantly scatters into the forward hemisphere in the CM system (i.e. in the same direction as that of attacking the Li atoms); Li+CH_3I and CCl_4 predominantly scatter products into the backward CM hemisphere; while Li+SF_6 and CH_3NO_2 must produce very broad CM product angular distributions.

The LAB product angular distributions were transformed to the CM coordinate system by the same fixed velocity approximation (FVA) procedure used to transform the elastic scattering. Here again the reactants were assumed to have their most probable source velocities; however, owing to the distribution of final translational energy as well as scattering angle for the reaction products, two additional approximations are required to utilize the FVA transformation procedure: it is initially assumed that the angular and E' distributions are independent; then it is further assumed that the E' distribution may be approximated by a delta function. The value of E' is varied until positive and negative CM scattering angles gives a consistent CM angular distribution. Extensive computer studies[13] have indicated that the CM angular distributions obtained from the FVA procedure are usually reliable, although somewhat broader than the true distributions; the values of E' derived may be relatively inaccurate (somewhat too low), although they do provide a qualitative indication of the energy partitioning.

Table I lists the values of the product recoil energies which provided the best FVA-CM product angular distributions; also listed are the ranges of E' values for each reaction which provided satisfactorily consistent FVA-CM product angular distributions. Table II gives the coefficients of an expansion of the derived LiX CM product angular dis-

Figure 3.

LAB angular distribution of LiO product derived from data points shown in Fig. 1; the solid curve through the data points indicates the "best" distribution based on analysis of the errors in the data points. The dotted curve gives the calculated distribution in centroid angles for an energy independent collision cross section. The dashed curve is back-calculated from the derived CM angular distribution shown in Fig. 8. Also shown is a kinematic diagram indicating the most probable reactant source velocities, the corresponding centroid vector $\underset{\sim}{C}$, and the relative velocity vector $\underset{\sim}{V}$; the circles indicate the lengths of the LiO recoil velocities for four of the possible product recoil energies, E' (kcal/mole). The two Li temperatures refer respectively to runs without and with the deflecting magnet and indicate the range of uncertainty in the Li temperatures.

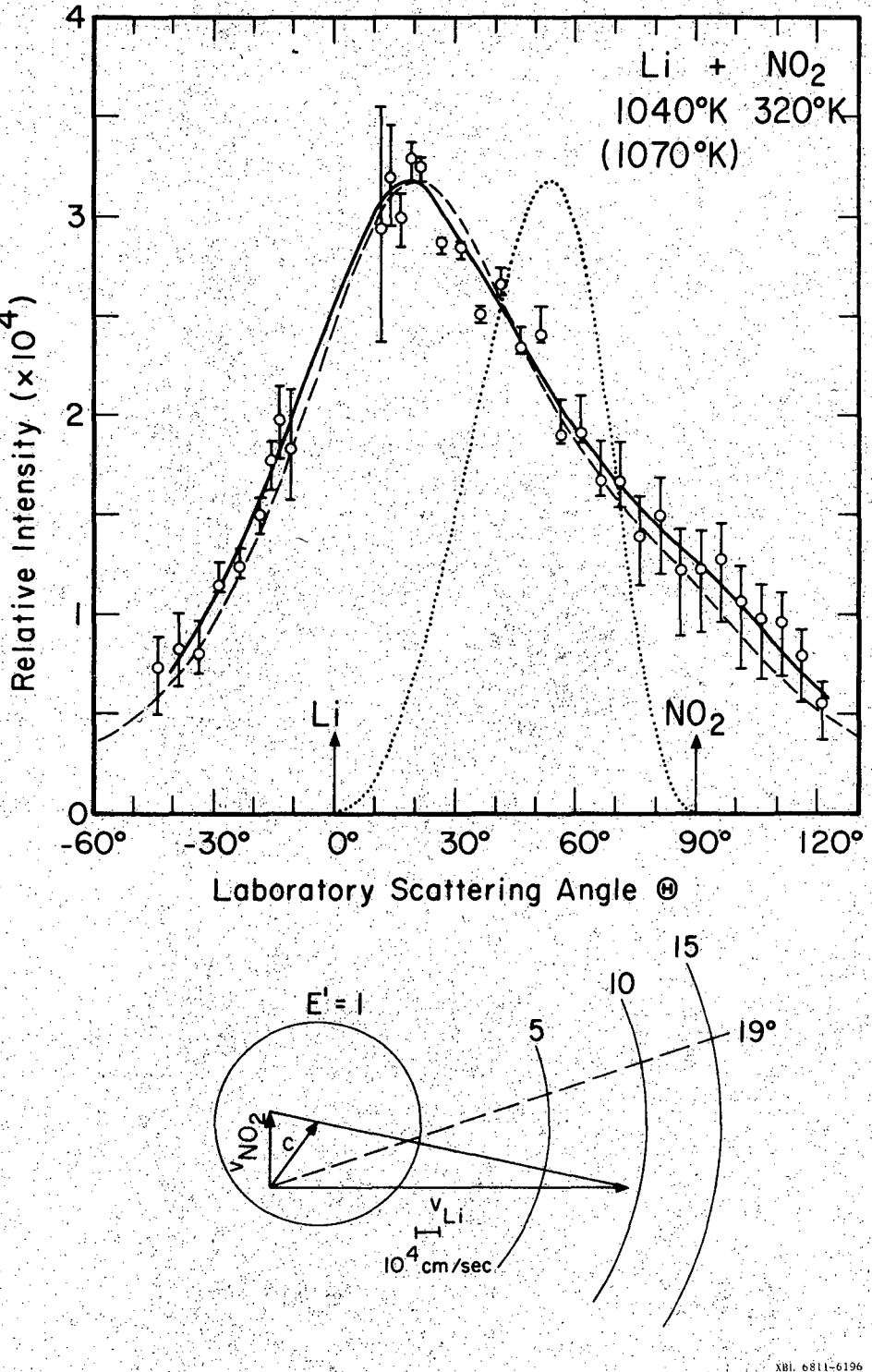
Li + NO2
1040°K 320°K
(1070°K)
Relative Intensity (×10^4)
Laboratory Scattering Angle Θ
Li
NO2
-60°
-30°
0°
30°
60°
90°
120°
0
1
2
3
4
E' = 1
5
10
15
19°
v NO2
c
v Li
10^4 cm/sec
XBL 6811-6196

Figure 3

Figure 4.

Calculated centroid distribution, kinematic diagram, and LAB angular distribution of $LiNO_2$ derived from the data of Fig. 1. The solid curve indicates the "best fit" to the data; the dashed curve was back-calculated from the CM angular distribution shown in Fig. 9.

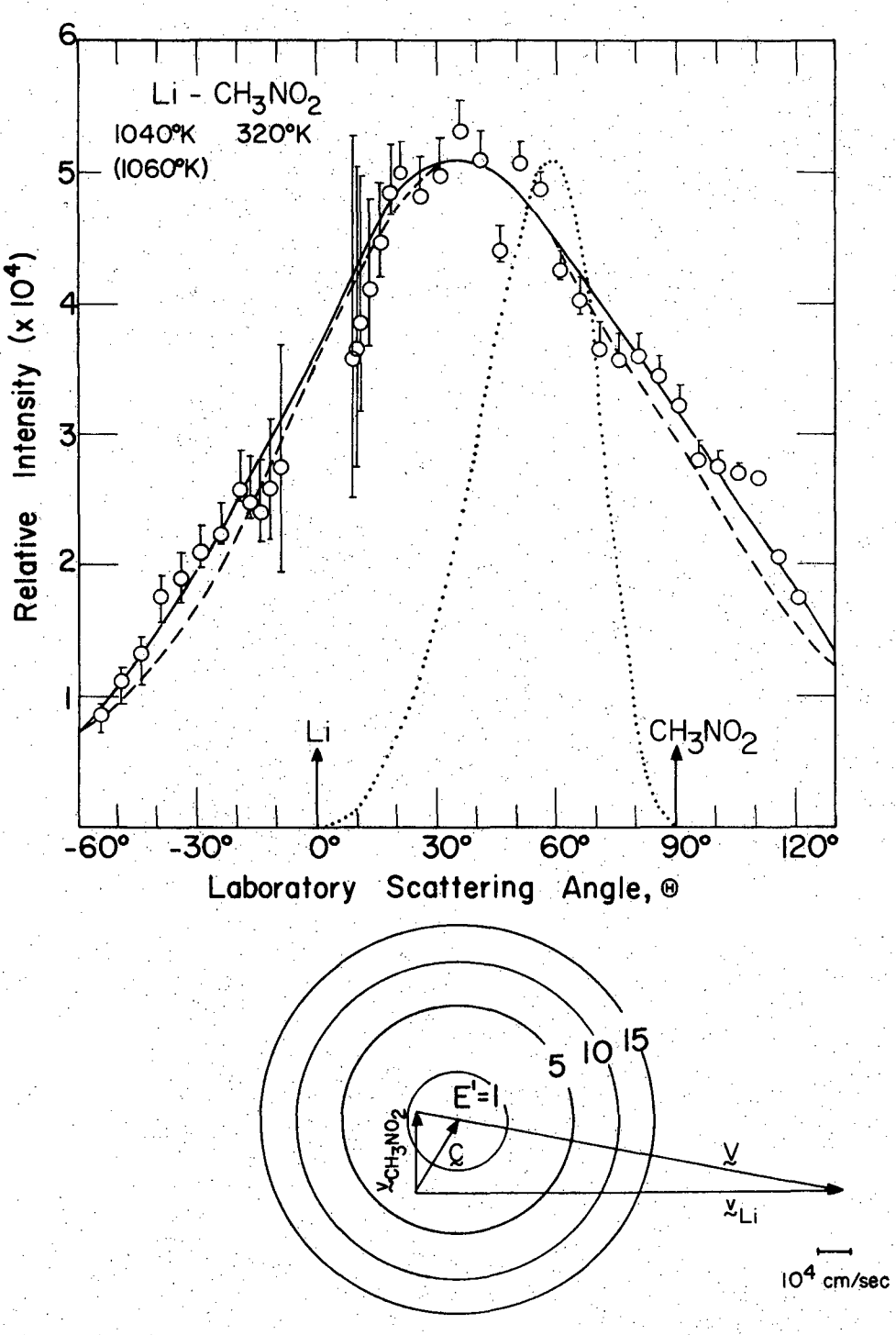
Li - CH3NO2
1040°K 320°K
(1060°K)
Relative Intensity (x 10⁴)
Li
CH3NO2
-60° -30° 0° 30° 60° 90° 120°
Laboratory Scattering Angle, Θ
5 10 15
E'=1
v CH3NO2
c
v
v Li
10⁴ cm/sec
XBL 694-417

Figure 4

Figure 5.

Calculated centroid distribution, kinematic diagram, and LAB angular distribution of LiF derived from data of Fig. 1. The solid curve indicates the "best fit" to the data. The other two curves (dashed and dash-dot-dash which coincide for $\theta \leq 70^{\circ}$) were back calculated from the LiF CM angular distributions shown in Fig. 9 (solid and dash-dot-dash respectively.)

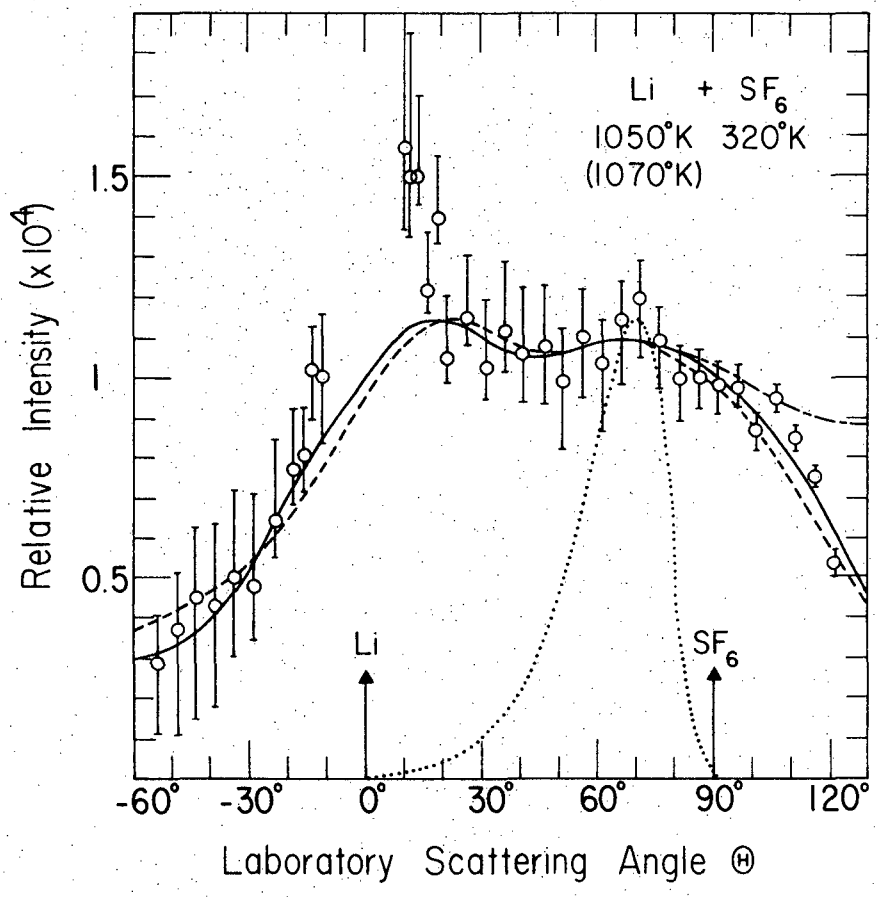
Li + SF6
1050°K 320°K
(1070°K)
Relative Intensity (x 10⁴)
1.5
1
0.5
Li
SF6
-60°
-30°
0°
30°
60°
90°
120°
Laboratory Scattering Angle Θ

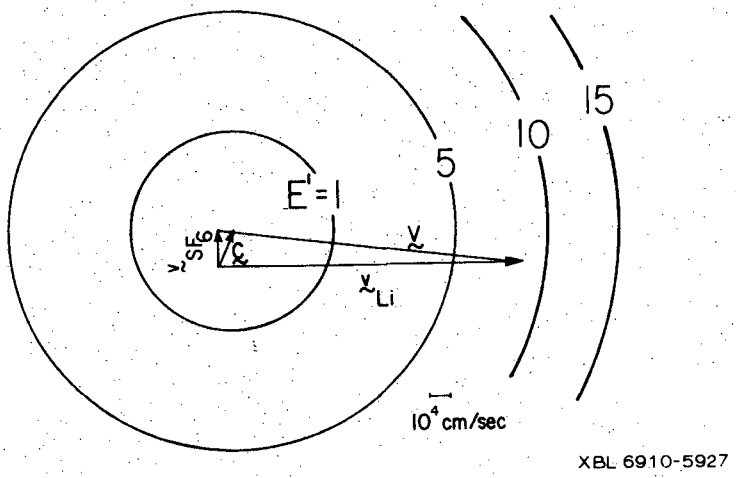
5
10
15
E'=1
v SF6
v Li
10⁴ cm/sec
XBL 6910-5927

Figure 5

Figure 6

Calculated centroid distribution, kinematic diagram, and LAB LiCl angular distribution derived from the data of Fig. 1. The solid curve indicates the "best fit" to the data. The other two curves (dashed and dash-dot-dash) were back-calculated from the LiCl CM angular distributions shown in Fig. 9 (solid and dash-dot-dash respectively); these latter two curves coincide for $\theta \leq 100^{\circ}$.

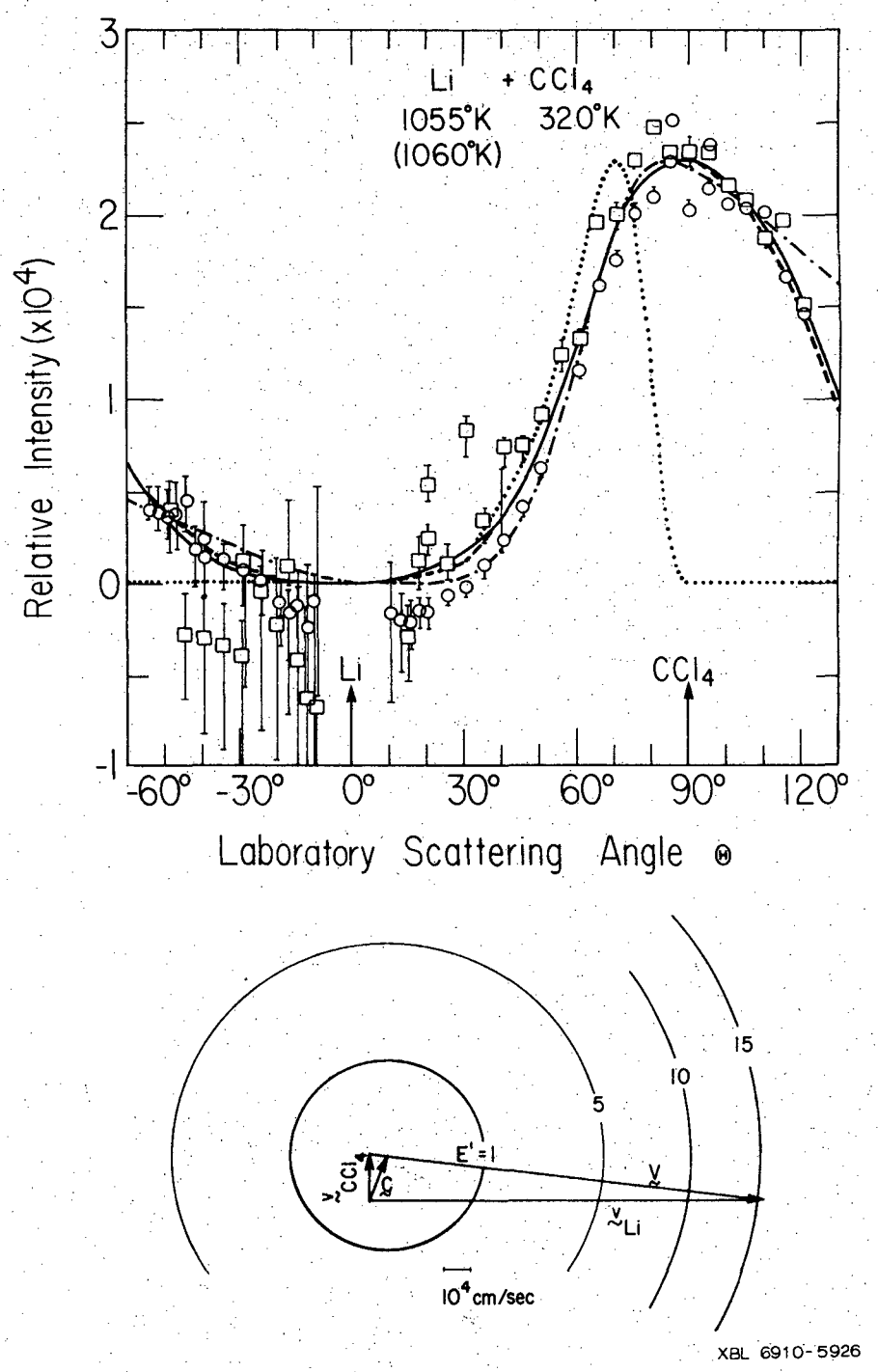
Li + CCl4
1055°K 320°K
(1060°K)
Relative Intensity (x10⁴)
3
2
1
0
-1
Li
CCl4
-60° -30° 0° 30° 60° 90° 120°
Laboratory Scattering Angle Θ
5
10
15
E' = 1
v CCl4
v Li
10⁴ cm/sec
XBL 6910-5926

Figure 6

Figure 7

Calculated centroid distribution, kinematic diagram, and LAB LiI angular distribution derived from the data of Fig. 1. The solid curve indicates the "best fit" to the data. The other two curves (dashed and dashed plus dash-dot-dash) were back-calculated from the LiI CM distributions shown in Fig. 9 (solid and solid plus dash-dot-dash curves respectively.)

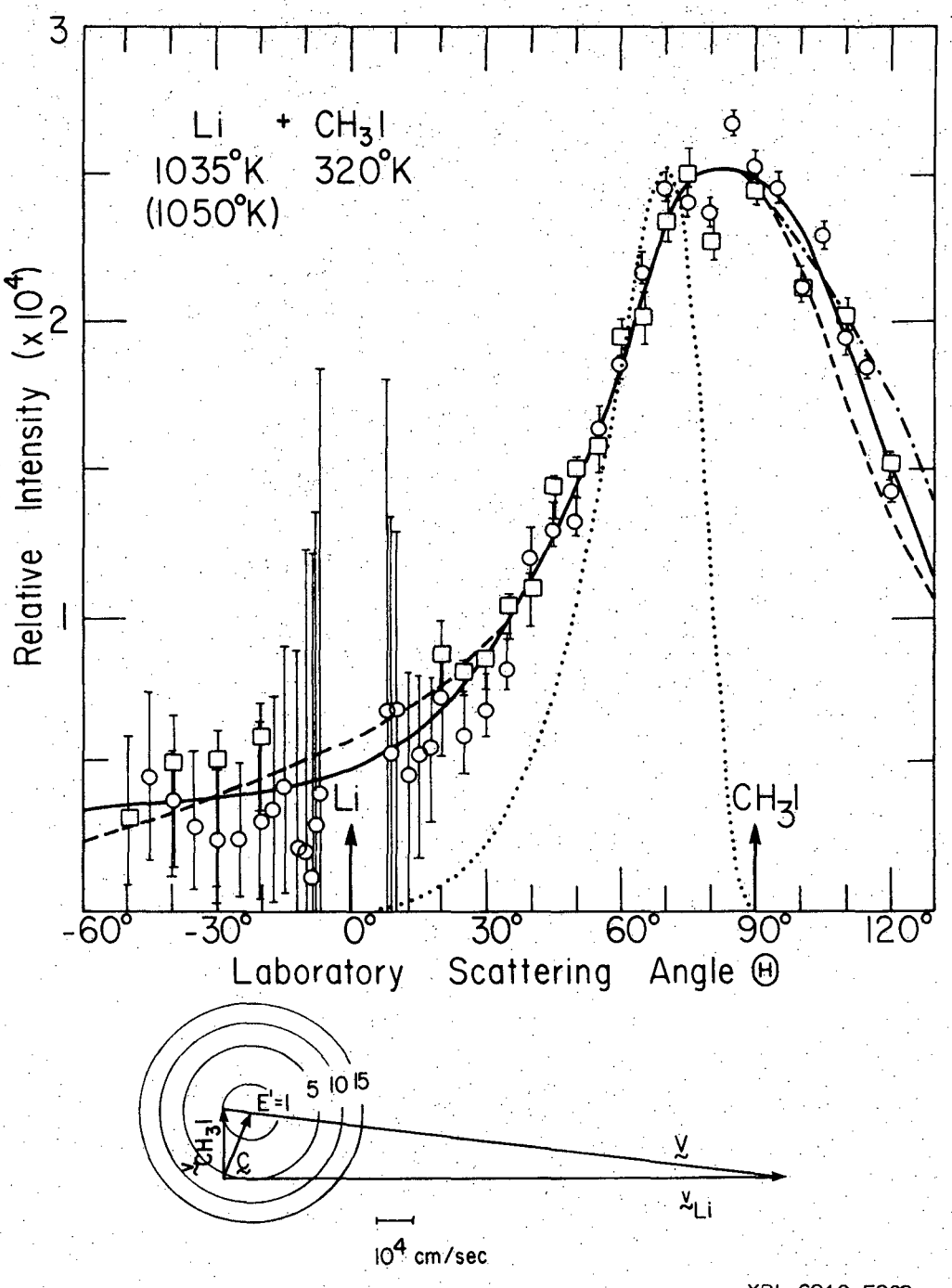
Li + CH3I
1035°K 320°K
(1050°K)
Relative Intensity (x10^4)
3
2
1
Li
CH3I
-60°
-30°
0°
30°
60°
90°
120°
Laboratory Scattering Angle Θ
E'=1
5 10 15
v CH3I
c
v
v Li
10^4 cm/sec
XBL 6910-5928

Figure 7

tributions given in Figs. 8 and 9 in terms of the Legendre polynomials. As a partial check of these derived CM LiX distributions, they were used to back-calculate the LAB distributions by holding E' fixed and averaging over assumed Maxwellian velocity distributions in both beams. This procedure is less than ideal because at the high source pressures employed here the velocity distribution from the many-channel array[36] and that from the knife edge source slit[37] are expected to deviate from the theoretical Maxwell distribution. These effects are expected to be minimal however. A large change in the Li velocity has only a very slight effect on the centroid velocity vector (see the vector diagrams in Figs. 3-7). A shift toward higher velocities of less than three percent[36] is expected in the non-alkali beam velocity distribution. Even a significantly larger shift than that predicted in Ref. 36 would have little effect because the velocity that corresponds to the nominal E' is large with respect to the centroid velocity vector for all systems with the possible exception of $Li+CH_3I$. Thus the averaging does give added credence to the FVA procedure results. It should be stressed that the primary justification for applying the FVA method is that the results are in qualitative agreement with the more extensive computor calculations[13] and are in accord with the only published cross sections that have been derived from velocity analysis of reactive scattering.[38]

Owing to the different chemical behaviors of the five gases studied here, separate discussions of the FVA derived CM distributions and back-calculated LAB distributions must be given.

a. $\underline{Li + NO_2}$ The reaction of Li and NO_2 almost certainly produces LiO product, i.e.

TABLE I. Estimates of Recoil Energies[a]

Reaction	E	ΔD_0	E' Best	E' Range
$Li + NO_2 \rightarrow LiO + NO$	1.88	10±4	2.4	2-3
$Li + CH_3NO_2 \rightarrow LiNO_2 + CH_3$	1.94		10.4	9-11
$Li + SF_6 \rightarrow LiF + SF_5$	2.02	56±7	1.6	1-2
$Li + CCl_4 \rightarrow LiCl + CCl_3$	2.03	43±5	17	1-43
$Li + CH_3I \rightarrow LiI + CH_3$	1.99	30±2	15	12-20

[a]All energies are given in kcal/mole. The initial relative translational kinetic energy of the reactants corresponding to the most probable source velocities is denoted by E; E' is the product recoil energy estimated from the FVA transformation procedure. $\Delta D_0 = D_0(LiX) - D_0(RX)$ is the reaction exoergicity. Bond dissociation data were taken from: for LiF, LiCl, and LiF, L. Brewer and E. Brackett, Chem. Rev. 61, 425 (1961); for LiO, Ref. 3; for NO_2 and CH_3I, G. Herzberg, Molecular Spectra and Molecular Structure III. Electronic Spectra and Electronic Structure of Polyatomic Molecules (D. Van Nostrand Co., Inc., Princeton, N.J., 1966); for SF_6, Ref. 8; for CCl_4, T. L. Cottrell, The Strengths of Chemical Bonds (Butterworth Scientific Publications, London, 1958).

TABLE II. LiX CM Distribution Expansion in Legendre Polynomials[a]

Reactant	a_0	a_1	a_2	a_3	a_4	a_5
NO_2	0.499	0.279	0.114	0.086	0.006	0.016
CH_3NO_2	0.721	0.246	0.031	0.023	-0.027	0.006
SF_6	0.704	0.186	-0.087	0.131	0.012	0.054
CCl_4	17.658	-7.239	-19.952	6.880	2.049	1.604
CH_3I	2.061	-0.627	-0.659	0.173	-0.027	0.079

[a]These coefficients are defined by $I_{LiX}(\theta) = \Sigma_n a_n P_n(\cos\theta)$ and are normalized such that $\Sigma_n a_n = 1$.

Figure 8.

Comparison of CM product angular distributions. The LiO product angular distribution from $Li+NO_2$ was obtained by transforming the solid curve of Fig. 3 at 5° intervals by the FVA procedure; the open circles give data for positive CM angles (rotations of the recoil velocity vector counter-clockwise from the original Li direction); the dark circles refer to negative values of θ; the data was extrapolated to $\theta = 180°$ from the last open circle data point. The K, Rb, and $Cs+Cl_2$ data were taken from Ref. 24. The LiX angular distributions reported in Part I for $Li+Cl_2$, Br_2 and I Cl all lie within the shaded region denoted Li+XY. All distributions were normalized to unity at $\theta = 0°$.

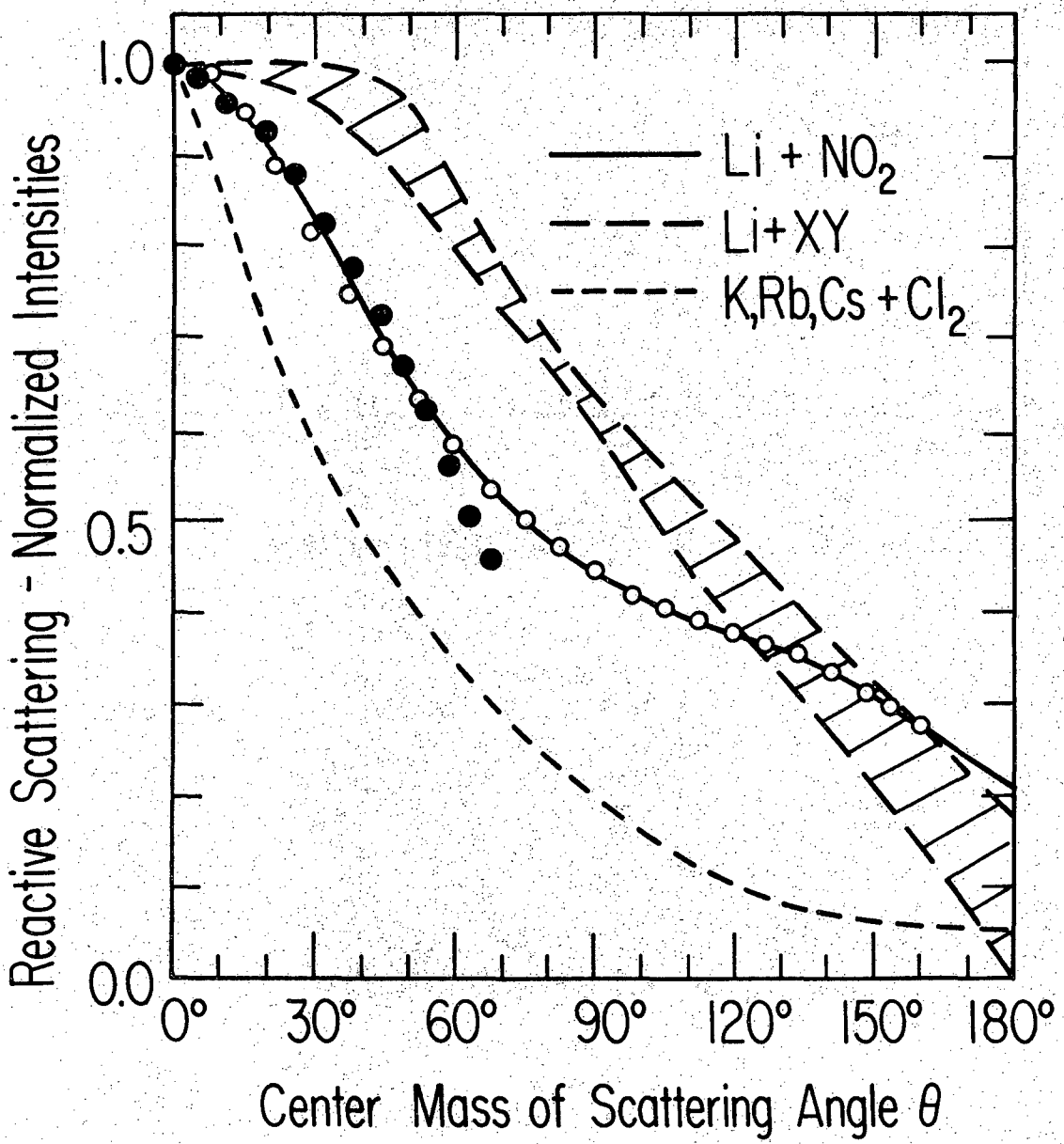
1.0
0.5
0.0
Reactive Scattering - Normalized Intensities
Li + NO2
Li+XY
K,Rb,Cs + Cl2
0°
30°
60°
90°
120°
150°
180°
Center Mass of Scattering Angle θ
XBL 6910-5929

Figure 8

Figure 9.

Comparisons of CM product angular distributions; all distributions normalized to unit peak height. The Li data were obtained from Figs. 4-7; the transformation procedure was the same as for Fig. 8. The K, Rb, and Cs + CCl_4 curves were taken from Ref. 7; the Na+CH_3I curve from Ref. 5; and K+CH_3I curve from Ref. 25. For Li+CCl_4 and CH_3I, back-calculations (for comparison with the original LAB distributions) were performed for both the derived CM distributions (solid curves) and for distributions assumed to be level from the peak in the derived distributions out to $\theta = 180°$ (dash-dot-dash curves).

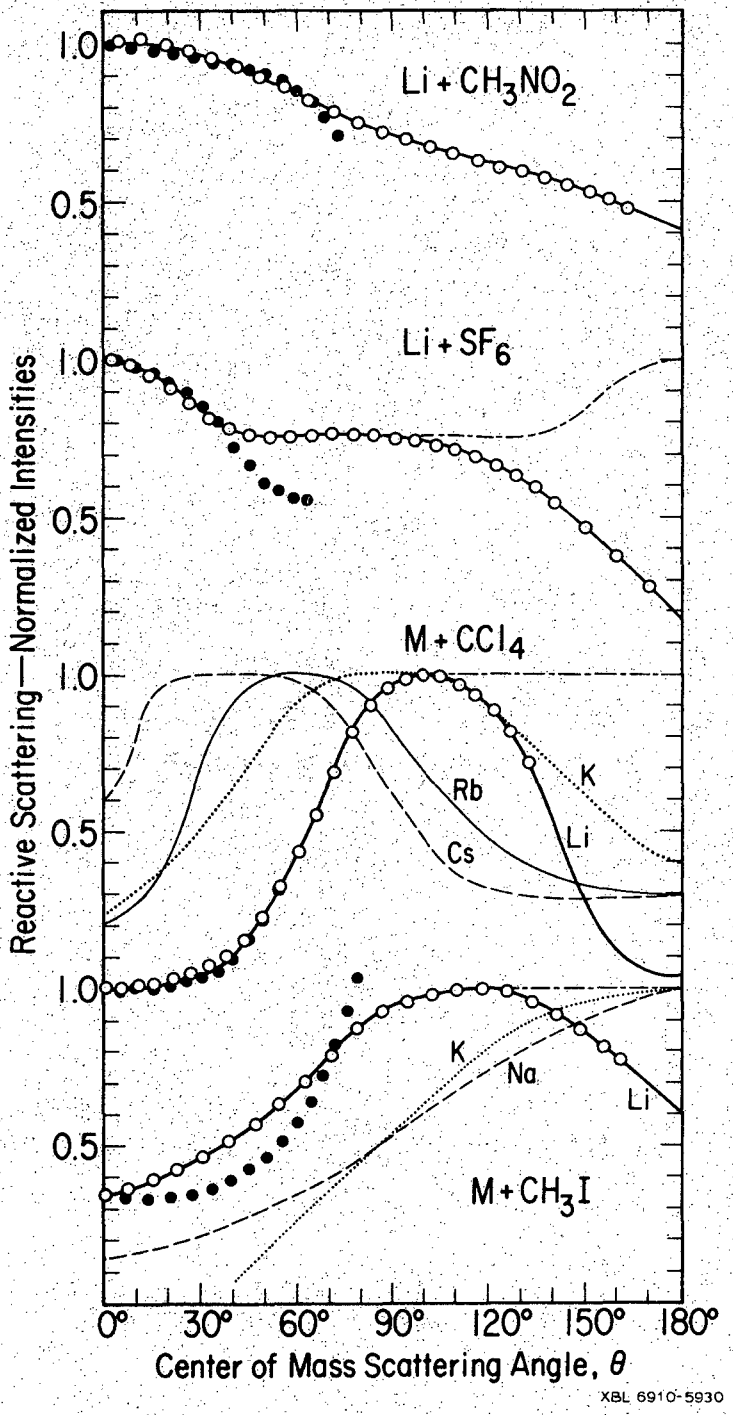
Li + CH3NO2
Li + SF6
M + CCl4
Rb
K
Li
Cs
K
Na
Li
M + CH3I
1.0
0.5
1.0
0.5
1.0
1.0
0.5
Reactive Scattering—Normalized Intensities
0°
30°
60°
90°
120°
150°
180°
Center of Mass Scattering Angle, θ
XBL 6910-5930

Figure 9

$$Li + NO_2 \rightarrow LiO + NO;$$

thermochemical arguments advanced in Ref. 3 eliminate the possibility of LiN or LiNO as the product of the reaction. The possibility of a $LiNO_2$ product which could be formed from N_2O_4 was precluded by maintaining conditions in the reactant beam such that only a negligible amount of the dimer could be present.[14]

The use of magnetic deflection analysis to derive the $Li+NO_2$ elastic and reactive angular distributions shown in Figs. 1, 2, 3 and 8 required the assumption that LiO is diamagnetic. In view of the fact that LiO has an unpaired electron, this assumption deserves close scrutiny. The LiO molecule is known to have a $^2\pi$ ground state.[15] Since the interaction of the electron spin with the external field would be ~0.7 cm^{-1} (for a field of ~15 kG), the spin-orbit intramolecular interaction is probably considerably greater than the interaction of either spin or orbital angular momentum with the external field. Under these conditions, the spin angular momentum would be coupled to the internuclear axis via the orbital angular momentum provided that the rotational excitation was insufficient to uncouple the spin; Hund's coupling case (a)[16] would then be applicable. The $^2\pi_{1/2}$ state would have no magnetic dipole moment while the $^2\pi_{3/2}$ state would have a magnetic dipole that would be rotationally averaged to near zero. This averaging is not complete however; for example, for a total angular momentum ~15$\hbar$, the absolute value of the time averaged component of the magnetic moment in the field direction, averaged over all M states, is approximately 10% of the Bohr magneton, μ_0, and some M states would have effective magnetic dipoles of up to 0.05 μ_0 for total angular

momentum up to 60ħ. Since rotational excitation of 2 kcal/mole (the approximate value found for KBr from K + Br_2[17,18]) corresponds to approximately 23ħ and an upper limit of about 56ħ is imposed by energy conservation, at least a small fraction of the LiO product is expected to be deflected in this experiment. Two possible further complications must also be considered, however. First the spin may become uncoupled from the internuclear axis at high rotational excitation. Under complete uncoupling, Hund's coupling case (b)[16] would apply, indicating a distribution of time averaged effective magnetic moments from $-\mu_0$ to $+\mu_0$ for both the $^2\pi_{1/2}$ $^2\pi_{3/2}$ states. The second consideration is that although LiO is known to have a $^2\pi$ ground state, KO and CsO apparently have $^2\Sigma$ ground states;[3] this suggests that perhaps LiO has a low lying $^2\Sigma$ excited state[19a] that could be appreciably populated in the reaction. Both of these effects would, of course, increase the fraction of product deflected by the magnet and thus be interpreted as elastic Li scattering rather than LiO scattering. The rotational excitation of reactively scattered products has been investigated for many systems,[31] and in no case has there been any observable coupling between the angle of deflection and the rotational energy distribution; therefore one may reasonably expect that there would be no very strong coupling in this system either. Since any $^2\Sigma$ product would be virtually completely deflected and, unless there is an unexpected, very strong coupling of the rotational excitation to the product deflection angle, the fractional deflection of the $^2\pi$ product is independent of scattering angle, Fig. 3 shows the angular distribution of only the $^2\pi$ ground state product and excludes any product in the $^2\Sigma$ excited state. An apparatus is currently being assembled which

will allow velocity analysis and perhaps electric deflection as well as magnetic deflection of the reaction products in order to more fully characterize all features of this system.

The LiO LAB distribution shown in Fig. 3 was transformed into the CM system by the FVA procedures. Consistent CM angular distributions were obtained for E' in the range of 2 to 3 kcal/mole; the angular distribution shown in Fig. 8 refers to E' = 2.4 kcal/mole, but the shape of the angular distribution changed only slightly as E' was varied from 2 to 3 kcal/mole. The LAB angular distribution back-calculated by averaging over the thermal velocity distributions in both beams with E' = 2.4 kcal/mole is shown in Fig. 3; here again, back-calculations for E' in the ranges 2-3 kcal/mole gave similar agreements with the original LAB distribution.

b. Li + CH_3NO_2 The magnetic deflection analysis presented in Ref. 3 and an electric deflection investigation[18] indicate that the products from the reactions of Na, K and Cs+CH_3NO_2 are the corresponding alkali nitrites; by extrapolation we expect the product for the present reaction to be $LiNO_2$. However, for all these reactions the formation of the alkali oxide is also an exoergic reaction path, and for Li it is expected to be more exoergic. Future electric deflection experiments should be able to determine if there is any LiO contribution to the reactive scattering; all analysis and discussion here assumes only $LiNO_2$ product. The CM distribution shown in Fig. 9 obtained by FVA transformation with E' = 10.4 kcal/mole is very similar to the consistent CM angular distributions provided by FVA for E' in the range 9-11 kcal/mole. Figure 4 shows the back calculated LAB distribution with E' = 10.4 kcal/mole.

c. Li+SF_6 The derivation of the CM angular distribution and back-calculation were performed with E' = 1.6 kcal/mole; once again, consistent CM angular distributions were obtained for a range of E', 1-2 kcal/mole, and these angular distributions were very similar to that shown in Fig. 9. In addition a symmetric distribution (dash-dot-dash curve in Fig. 9) was obtained by reflecting $\theta < 90^\circ$ through $\theta = 90^\circ$; back-calculation with this curve for E' = 1.6 is also shown in Fig. 5.

d. Li + CCl_4 Recent product velocity analysis experiments on the reactions of the heavier alkali metals with CCl_4 have indicated[19] that the E' distribution varies markedly with scattering angle for these reactions. Consequently, the FVA transformation procedure is expected to be an especially bad technique in the case of Li+CCl_4; nevertheless, the FVA derived CM angular distribution for E' = 17 kcal/mole is shown in Fig. 9 to give a qualitative indication of the product angular distribution. The FVA transformation of the data of Fig. 6 yields consistent CM angular distributions for a range of E' values from 1 to 40 kcal/mole. The qualitative shape of the CM angular distribution obtained is independent of the E' value taken, although the location of the peak does vary from $\theta = 120^\circ$ to 110° to 100° as E' is varied from 1 to 2 to 25 kcal/mole respectively. Figure 6 shows the back calculation at E' = 17 kcal/mole for the solid curve of Fig. 9; the dash-dot-dash curve extended flat to 180° from the peak of the solid curve of Fig. 9 was used with E' = 2 kcal/mole to back-calculate the dash-dot-dash curve of Fig. 6. These two curves demonstrate the lack of sensitivity of the LAB distribution to the assumed value of E'. However, back-calculations with a CM angular distribution symmetric about $\theta = 90^\circ$ (i.e. translate the solid curve of

Fig. 9 by -10° and reflect $\theta < 90°$ thorough $\theta = 90°$) do not reproduce the LAB distribution for any value of E'.

e. Li + CH_3I Figure 9 shows the FVA derived CM distribution for E' = 15 kcal/mole. The FVA transformation provided consistent CM distributions (similar to that shown in Fig. 9) for E' in the range 12-20 kcal/mole. The FVA transformation also provided a consistent CM distribution for a second, lower range to E' values; in this energy range, the LAB → CM transformation was doubled valued and the fit was rejected because back-calculations failed to reproduce the LAB distribution at negative values of Θ. Figure 7 shows back-calculations for E' = 15 kcal/mole of both of the LiI CM angular distributions shown in Fig. 9. The FVA derived CM distribution provided an adequate fit to the measured LAB distribution for E' in the range 15-20 kcal/mole; back-calculations with the CM distribution flat from $\theta = 120°$ to 180° adequately fit the LAB distribution for E' in the range 10-15 kcal/mole.

3. Total Reaction Cross Sections

Table III gives values of the total reaction cross reactions calculated by the two methods described in Part I ($Q_R(A)$ and $Q_R(B)$ calculated by Methods A and B respectively); also listed are the van der Waal's coefficients, C, for the interaction of the two gases, the total collision cross sections, $Q_{t,abs}$, and the resolution corrected total collision cross-sections $Q^{eff}_{t,abs}$. The reactive cross sections were calculated assuming equal Li and LiX ionization efficiencies; the geometric parameters required for the calculations were the same as those reported in Part I. The force constants, C, were calculated from the Slater-Kirkwood approximation with 1, 17, 24, 48, 32 and 14 effective numbers of electrons for

TABLE III. Total and Reactive Cross Sections[a]

System	$\langle E^{-1/3} \rangle^{-3}$	C	$Q_{t,abs}$	$Q_{t,abs}^{eff}$	$Q_R(A)$	$Q_R(B)$
Li + NO_2	2.45	320	390	210	15	16
Li + CH_3NO_2	2.53	740	550	280	58	55
Li + SF_6	2.71	650	520	260	17	18
Li + CCl_4	2.73	1110	650	320	37	43
Li + CH_3I	2.67	780	560	280	27	27

[a]The mean elastic collision energies, $\langle E^{-1/3} \rangle^{-3} = 1.36\ (\mu/m_{Li})\ k\ T_{Li}$ are given in kcal/mole, the van der Waals force constants in 10^{-12} erg - $\mathring{A}^6$, and the cross sections in $\mathring{A}^2$. The total cross sections were calculated for relative velocities corresponding to $\langle E^{-1/3} \rangle^{-3}$.

Li, NO_2, CH_3NO_2, SF_6, CCl_4, and CH_3I. The polarizability values used were (in $\mathring{A}^3$) 20 for Li;[20] 3.1 for NO_2;[21] 7.2 for CH_3NO_2;[22] 6.2 for SF_6;[22] 11.1 for CCl_4;[22] and 8.0 for CH_3I.[22] The induction terms were calculated using dipole moments of 0.29, 3.1, and 1.65 Debyes[23] for NO_2, CH_3NO_2, and CH_3I respectively. Probable sources of error in the calculated total cross sections are discussed in Part I; in general, the quoted total reaction cross sections are estimated to be closer than a factor of two to the true values. Moreover, the ratio of derived Q_R values for any two gases is expected to be somewhat more accurate than are the individual values.

As may be seen from Fig. 2 the shape of the CM elastic scattering for these five reactions showed significant deviations from each other and from the elastic scattering from cyclohexane. These deviations caused the normalization of the elastic scattering to the form factor employed in Method A to be less unambiguous than in Part I; but in view of the good agreement achieved with Method B, evidently no large errors were introduced.

E. Discussion

1. Li + NO_2

This reaction appeared likely to be of special interest for comparison with the alkali atom-halogen molecule reactions which are strongly exoergic and are believed to proceed by a long-range electron transfer followed by almost immediate separation of the products,[26]

$$M + X_2 \rightarrow M^+ + X_2^- \rightarrow M^+X^- + X.$$

The electron transfer occurs at the distance of separation where the Coulomb potential energy compensates for the difference between the ionization potential of M and the electron affinity of X_2. The electron affinity of NO_2 is high,[2] probably higher than that of the diatomic halogen molecules, but the electron affinity of O is much less than that of a halogen atom. Thus, the Li + NO_2 reaction is much less exoergic; whereas the electron transfer can take place at large separation of the reactants, the Li^+ NO_2^- ion pair formed must approach to within much closer distances before the LiO and NO products can begin to separate. The potential energy surface for this reaction is, therefore, expected to exhibit relatively restricted entrance and exit channels with a deep chemical well corresponding to the formation of the strongly bound $LiNO_2$ intermediate. On the other hand, the expected potential energy surfaces for alkali atom-halogen molecule reactions exhibit no appreciable well and a wide exit channel.[27]

These features of the potential energy surface of the Li + NO_2 system might have been expected to favor a reaction which proceeded via formation of an intermediate, long-lived complex. However, the observed sharp foward peaking of the LiO product is characteristic of the ultra-direct mechanism found for the M+X_2 reactions and indicates that the reaction is complete in a time shorter than the rotational period of the complex. The observation of such similar product distributions for both the Li+NO_2 reaction and the alkali metal-diatomic molecule reactions which have such qualitatively different potential surfaces provides further evidence that the mechanism of the M+X_2 reactions is more general than a "spectator stripping" behavior because the Li+NO_2 potential surface implies appreciable interaction during the separation of the NO and LiO products.

The sharp forward product peaking observed here has previously been characteristic of reactions with very large total reaction cross sections so that most of the reactive events corresponded to collisions with relatively large impact parameters. The Li + NO_2 total reaction cross section observed here ($15\mathring{A}^2$) is in striking contrast to the much larger reaction cross sections reported in Part I for the Li + XY reactions (eg. $Q_R = 85\mathring{A}^2$ for Li + Cl_2). The high electron affinity of NO_2 would lead one to predict a crossing of the covalent and ionic potential curves at large Li-NO_2 separations; the electron transfer mechanism should, therefore produce reactive collisions at very large impact parameter. Owing to the unpaired spins of both Li and NO_2, however, the total spin of the collision partners may be 1 or 0; the electron transfer mechanism is applicable only to the spin singlet potential energy surface because the triplet covalent curve is not perturbed by the ionic curve. Assuming only non-reactive scattering from the triplet potential energy surface at these energies, the measured total reaction cross section must be 25% of that appropriate to the spin singlet potential energy curve. The measured cross section thus corresponds to a cross section of $60\mathring{A}^2$ for the singlet collisions; however, in view of the high NO_2 electron affinity, an even bigger cross section would be expected. As suggested in Ref. 26, the covalent-ionic curve crossing for this system may occur at too large a separation to allow an efficient electron transfer, thereby reducing the magnitude of the reaction cross section. Alternatively, some of the collision events that cross to the ionic surface may produce non-reactive scattering. The observation that the Li + NO_2 produces more wide-angle elastic scattering than does cyclohexane, may indicate that the wide-angle

Li scattering proceeds via formation of an intermediate $LiNO_2$ long-lived complex; studies of the elastic scattering of K and Cs from NO_2 and related compounds[28] have been interpreted in terms of formation of such complexes. Finally, one must also realize that any $^2\Sigma$ electronically excited product produced is not measured and if a fraction of the $^2\pi$ ground state is deflected by the magnet, it would not be detected either; both of these factors would reduce the magnitude of the derived reaction cross section. These ambiguities will be minimized when velocity and rotational analysis becomes available.

2. Li + CH_3I

The LiI is scattered predominately backward in the CM system in agreement with the previously reported behaviors for the Cs and Rb[32] as well as the K[25] and Na[5] reactions with CH_3I; however the present results leave little doubt that the LiI CM product angular distribution is considerably broader than that of the corresponding NaI and KI. The high translational product recoil energy of LiI is also in approximate accord with the values found for NaI and KI; FVA results are not available for the Cs and Rb reactions.

The total reaction cross section reported for Li + CH_3I in Table III is comparable to the value of 35$\mathring{A}^2$ reported for K+CH_3I in Ref. 21; the total reaction cross sections evaluated from the attenuation of the elastic scattering of K + CH_3I also lie in the same range (25 - 47$\mathring{A}^2$).[29] The behavior of Na + CH_3I appears somewhat anomalous; a value of 5$\mathring{A}^2$ was reported in Ref.20.

There are extensive trajectory calculations on several potential surfaces for the M + CH_3I reactions;[30] these calculations predict the

observed backward scattering of the products, but fail to reproduce the high product translational energies observed, presumably because the surfaces do not have enough repulsive character between the products. Further calculations on improved surfaces would be desirable to determine if the broader LiI CM angular distribution is due to the effect of the small mass of Li on the reaction dynamics; such a mass effect was suggested in Part I as the reason that the LiX product distributions from reactions with diatomic halogens were broader than the corresponding distributions of the heavier alkali metals.

3. Li + CCl_4

Quantitative comparisons of the M+CCl_4 distributions shown in Fig. 9 could be misleading owing to the reported strong coupling of the E' and θ distributions for these reactions;[19] however the present results clearly indicate that the Li+CCl_4 reaction produces appreciably less product scattering into the forward CM hemisphere than do the corresponding K, Rb, and Cs + CCl_4 reactions. The total reaction cross section listed in Table III correlates well with the values of 150, 100 and 60$\mathring{A}^2$ for Cs, Rb and K+CCl_4 respectively reported in Ref. 7. The two trends, decrease in reaction yield and shift of preferred CM recoil angle to larger values as the atomic number of the alkali metal is decreased, that were observed in Ref. 7 hold for the Li+CCl_4 reaction as well. These systems present another opportunity for theoretical calculations to elucidate evident trends.

4. Li+SF_6

An intermediate long-lived $LiSF_6$ complex would be expected to be an approximate prolate top with three similar rotation constants. Forma-

tion of such an intermediate complex would, according to the statistical complex model,[33] produce a symmetric CM LiF product distribution with peaking at $\theta = 0^\circ$ and 180°; a LAB distribution back-calculated from such a curve fit the experimental data except at wide positive angles (see Fig. 5). The signal to noise ratio is particularly bad at these angles, but if the scattering is less than that expected from the statistical complex model, it could indicate that a $LiSF_6$ complex with a lifetime comparable to a rotational period is formed. Such "osculating complexes" have been observed.[34] The complex model would predict only a small amount of energy in translation of the products because the total energy must be divided among many degrees of freedom; the crude value of E' found for this reaction conforms with this prediction.

The reaction of $Cs+SF_6$ has been extensively investigated[8] and all features of the reaction dynamics correspond to the predictions of the statistical complex model; thus the two members at the extremes of the alkali family both apparently react with SF_6 by the same mechanism. It is also of interest to note that the $Li+PCl_3$ reaction also produces a nearly symmetric CM product distribution, but in this case peaking at $\theta = 90^\circ$ is observed; it has been suggested that this might be understood in terms of the formation of an intermediate oblate top complex.[1]

The total reaction cross section given in Table III correlates nicely with the values derived from the elastic scattering of K from SF_6 reported in Ref. 29 ($Q_R(K) \sim 21\text{-}50\text{Å}^2$).

5. Li + CH_3NO_2

This reaction bears many resemblances to the $Li+CH_3I$ reaction. In both cases, a reactive group is abstracted from a methyl radical by the

attacking Li atom and the product is formed with a high translational energy. Moreover, the strengths of the CH_3-I and the CH_3-NO_2[35] bonds are virtually identical; although the Li-NO_2 bond strength is unknown, it seems likely that it is comparable to that of an alkali halide so that the reaction exoergicities are similar for these reactions. Moreover, Table III indicates that the long range van der Waals interactions between the reactants are quite similar for the two cases. The enhanced CH_3NO_2 reaction cross section shown in Table III might simply be a consequence of the larger geometric size of the NO_2 group relative to that of an I atom. Trajectory calculation studies[30] have shown that the product angular distribution should change from a strong anisotropic backward peaking to an isotropic CM distribution as the total reaction cross section is increased; this prediction is in qualitative accord with the trends observed here.

These five reactions demonstrate the wide diversity of the reactions of Li atoms; further studies to extract product velocity and rotational energy distributions are planned which should more clearly elucidate the dynamics of these reactions.

ACKNOWLEDGEMENT

We are indebted to Mr. Shen-Maw Lin, L. C-H Loh, and C. A Mims for help in the collection and analysis of some of the data and for many informative discussions. This work was supported by the Atomic Energy Commission.

REFERENCES

1. D. D. Parrish and R. R. Herm, J. Chem. Phys. 51, 5467 (1969); this article is referred to in the text as Part I.
2. Values between 45 and 90 kcal/mole have been measured for the electron affinity of NO_2. References 3 gives a complete discussion. Considerable debate still exists over the exact value.
3. R. R. Herm and D. R. Herschbach, J. Chem. Phys. 52, 5783 (1970).
4. D. R. Herschbach, Disc. Far. Soc. 33, 144 (1962)
5. J. H Birely, E. A. Entemann, R. R. Herm, and K. R. Wilson, J. Chem. Phys 51, 5461 (1969).
6. T. H. Bull and P. B. Moon, Disc. Far. Soc. 17, 54 (1954).
7. K. R. Wilson and D. R. Herschbach, J. Chem. Phys. 49, 2676 (1968).
8. S. M. Freund, G. A. Fisk, D. R. Herschbach, and W Klemperer, J. Chem. Phys.(to be published).
9. See also: D. D. Parrish, Ph.D. Thesis, University of California, Berkeley, 1970; Chapter II.
10. J. H. Birely, R. R. Herm, K. R Wilson and D. R. Herschbach, J. Chem. Phys. 47, 993 (1967).
11. For reviews, see: E. F. Greene, A. L. Moursund, and J. Ross, Adv. Chem. Phys. 10, 135 (1966); and E. F. Greene and J Ross, Science 159, 587 (1968).
12. S. Datz, D. R. Herschbach, and E. H. Taylor, J. Chem. Phys. 35, 1549 (1961).
13. (a) E. A. Entemann, Ph.D. Thesis, Harvard University, 1967; (b) E. A. Entemann and D. R. Herschbach, Disc. Far. Soc. 44, 289 (1967).

14. The NO_2 pressure in the oven, as read on a thermocouple gauge, was 1.1 Torr; this would correspond to an equilibrium N_2O_4/NO_2 source pressure ratio of ~ 1%. However, owing to the possible contamination of this gauge by the corrosive gases employed in this study, it is desirable to get other estimates of the N_2O_4 concentration in the beam. In Part I the ICl was immersed in an ice bath at 0°C; thus, the ICl pressure was certainly no more than it's equilibrium vapor pressure at this temperature, and was probably considerably lower, as a flow situation existed. Comparisons of the Li beam attenuations in the NO_2 and ICl experiments and of the Li-NO_2 and Li-ICl resolution corrected total cross sections provide an upper limit of 6.2 Torr for the NO_2 pressure. This indicates that the N_2O_4/NO_2 ratio had to be less than 6% in the oven, and actually was probably considerably less. Perhaps the best argument against any measurable role of N_2O_4 in this experiment is provided by a previous crossed beam study (Ref. 3) of Cs + NO_2; using a combination of magnetic and electric deflection analysis, these workers reported appreciable CsO signal, but no $CsNO_2$ signal. Since the gas oven design employed here was identical to that used in Ref. 3, and both experiments were certainly run with very similar NO_2 pressures, this observation indicates a negligable N_2O_4 concentration in experiments reported here.

15. R. A. Berg, L. Wharton, W. Klemperer, A. Buchler, and J. L. Stauffer, J. Chem. Phys. 43, 2416, (1965).

16. G. Herzberg, Molecular Spectra and Molecular Structure I. Spectra of Diatomic Molecules (D. van Nostrand Co. Inc., Princeton N. J. 1950).

17. R. R. Herm and D. R. Herschbach, J. Chem. Phys. 43, 2139 (1965).

18. C Maltz and D. R. Herschbach, Disc. Far. Soc. 44, 176 (1967).

19. S. Riley, P. E. Siska, and D. R. Herschbach, to be published.

19a. An electronic structure calculation for LiO predicts a $^2\Sigma$ state lying only ~8 kcal/mole above the ground state; P. Cade and A. Wahl, as cited in footnote 38 of Ref 3 above.

20. B. Bederson and E. J. Robinson, Adv. Chem. Phys. 10, 1 (1966).

21. J. E. Boggs, J. Phys. Chem. 68, 2379 (1964).

22. Landolt-Bernstein Zhalenwerte und Functionon, A. M. Hellwege and K. H. Hellwege, Eds. (Springer-Verlag, Berlin), Vol. 1, Part 3 (1951); pp. 510 ff.

23. C. H. Townes and A. L. Schawlow, Microwave Spectroscopy (McGraw-Hill, New York, 1955).

24. R. Grice and P. B. Empedocles, J. Chem. Phys. 48, 5352 (1968).

25. G. H. Kwei, J. A. Norris and D R. Herschbach, J. Chem. Phys. 52, 1317 (1970).

26. D. R. Herschbach, Adv. Chem. Phys. 10, 319 (1966).

27. See the surfaces used in the Monte Carlo investigations of the alkali atom-halogen molecule systems; N C. Blais, J. Chem. Phys. 49, 9 (1968); M. Godfrey and M Karplus, J. Chem. Phys. 49, 3602 (1968); P. J. Kuntz, E. M. Nemeth and J. C. Polanyi, J. Chem. Phys. 50, 4607 (1969); and P. J. Kuntz, M. H. Mok, and J. C. Polanyi, J. Chem. Phys. 50, 4623 (1969).

28. D. O. Ham and J. L. Kinsey, J. Chem. Phys. 48, 939 (1968); D. O. Ham, Ph.D. Thesis, Massachusetts Institute of Technology, 1968; D. O. Ham and J. L Kinsey, J. Chem. Phys. 53, 285 (1970).

29. J. A. Airey, E. F. Greene, G. P. Reck, and J. Ross, J. Chem. Phys. 46, 3295 (1967).

30. See, for example, M. Karplus, in Linus Pauling Festschrift (W. H. Freeman and Co., San Francisco, 1967), and other work cited therein.

31. C. Maltz, Ph.D. Thesis, Harvard University, 1969.

32. G. H. Kwei, Ph.D. Thesis, University of California, Berkeley, 1967.

33. W. B. Miller, S. A. Safron, and D. R. Herschbach, Disc. Far. Soc. 44, 108 (1967).

34. G. A Fisk, J. D. McDonald, and D. R. Herschbach, Disc. Far. Soc. 44, 228 (1967).

35. T. L. Cottrell, The Strengths of Chemical Bonds (Butterworth Scientific Publications, London, 1958).

36 D. R. Olander, R. H. Jones and W. Siekhaus, UCRL Rept. 19084, Lawrence Radiation Laboratory, Berkeley, 1969; J. Appl. Phys. (to be published); and W. J. Siekhaus, R. H. Jones and D R. Olander UCRL Rept. 19637, Lawrence Radiation Laboratory, Berkeley, 1970; J. Appl. Phys. (to be published). Their experimental measurements and theoretical calculations agree that a 5.5% energy enhancement should occur in flow from channel sources at the high pressure limit. There is a monotonic increase toward this limit as the pressure is increased.

37. The Laval-nozzle effect is known to narrow the distribution and shift the peak toward higher velocities; see R. J Gordon, R. R. Herm and D. R. Herschbach, J. Chem. Phys. 49, 2684 (1968). This Laval effect will be discussed further in Chapter VII of this thesis.

38. For the $K+I_2$ reaction the FVA-CM product angular distribution and the nominal product recoil energy which were derived in Ref. 10 have been found to be in very good qualitative agreement with the more nearly exact product CM angular distribution and most probable recoil energy which were extracted from velocity analysis of the reactive scattering of this system. These velocity analysis data are presented in K. T. Gillen, Ph.D. Thesis, University of Wisconsin, 1970.

IV. HARMONIC FORCES, NORMAL MODES MODEL FOR INVESTIGATION OF CHEMICAL REACTION DYNAMICS

A. Introduction

A wide variety of detailed experimental features of gas phase bimolecular exchange reactions have been obtained from molecular beam and chemiluminescence studies in the last five or ten years. This rapid growth in our experimental knowledge of these reactions has been paralleled by an increasing number of three-dimensional, exact classical trajectory studies, employing extensive numerical integrations on a digital computer, which have reproduced many of the experimentally observed reaction features. In this way, these classical trajectory studies have already been instrumental in elucidating the important features of the interatomic forces in a number of these reactions and will, no doubt, continue to extend our knowledge of these forces for some time to come. Nevertheless, concomitant with this growing body of exact numerical trajectory calculations, it seems worthwhile to continue to examine simple models of the reaction dynamics in order to (1) provide greater physical insight into the possible range of values assumable by a given reaction feature, (2) possibly attempt to correlate different physical phenomena, as, for example, the energy partition in bimolecular exchange reactions and photodissociation, and (3) provide a starting point for estimates of the magnitude of the interatomic forces which could serve as input information for the more sophisticated, exact trajectory calculations.

One such model will be described here. Basically five gross simplifications are made. The dynamics are treated completely classically; this enhances the achievement of physical insight into the features of the

dynamics and simplifies the mathematical treatment. Secondly all interatomic and intermolecular forces are treated as if they were harmonic, i.e. consider all particles at their equilibrium position except for the one particle of interest; the force on this particle can be expressed as a sum of terms, each of which is directly proportional to the displacement of the particle from its equilibrium position. Thus the complete reaction system is treated as one large molecule. The presence of only harmonic forces allows an approximatate solution of the dynamics of the reaction to be found by expressing the overall motion of the particles as a superposition of normal modes of oscillation, thereby facilitating the integration along the classical trajectories. Thirdly, the geometry of the system is greatly simplified; in all applications of this model so far attempted by this writer, all particles have been constrained to a linear configuration. Thus, the number of normal modes that must be handled is greatly reduced; this of course, further reduces the mathematical complexity. A further advantage of the linear configuration is that the normal modes analysis is valid (within the harmonic forces assumption,) even for large particle displacements because the magnitude of the internuclear distances do not enter the calculation; the solution is dependent only upon the displacement of the internuclear distances from their equilibrium values. This model could certainly be extended to two or three dimensions if the investigation of a suitable system warrented the additional complexity. Assuming that only adjacent particles interact constitutes the fourth simplification. This approximation allows most of the force constants of the harmonic oscillator potentials to be set equal to values determined by spectroscopic techniques. Finally the distribution of initial states which exists

in any experimental system is ignored; a representative, simplified initial state is taken and the single resulting final state is assumed to be reasonably indicative of the most probable final experimental state. This fifth assumption is convenient but not necessary; any distribution of initial conditions could be integrated over by a systematic or a Monte Carlo technique.

This model is certainly not new to the chemical literature and was employed extensively by N. B. Slater to discuss the dynamics of unimolecular decomposition. More recently, it has been applied to the problem of the vibrational excitation of a diatomic molecule by collision with an atom[1] and to the problem of the energy partitioning in reactions of the alkali atoms with the halogen molecules.[2] The work in Ref. 2b will be more extensively discussed in Section C of this chapter. A recent application of this model to the energy partitioning in the reactions of Cs with the alkyl iodides has been published;[3] this work is incorporated with some extensions to constitute Chapter V of this thesis. A very similar model has been applied to the interaction of a gas atom with a crystal lattice.[4]

The formulation and application of the simplest such model will be discussed here; this is the three particle, one-dimensional model. The following chapter will discuss the extension of the linear model to four particles.

B. Formulation of the Linear, Three Particle Normal Modes Model

The system is treated as three particles which are constrained to a linear, one-dimensional collision with the notation as shown in Fig. 1.

Figure 1. Coordinates used in treatment of the normal modes model. All indicated distances are vector quantities. k_1 represents the force constant of the harmonic oscillator potential between particles 1 and 2 while k_2 refers to that between particles 2 and 3.

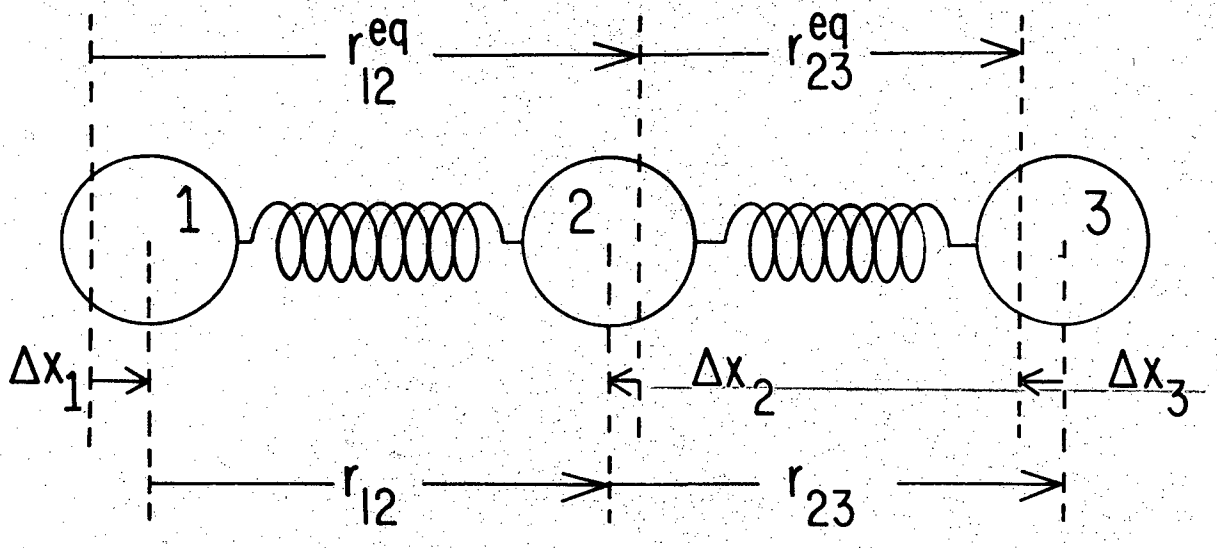
r_{12}^{eq}
r_{23}^{eq}
1
2
3
Δx_1
Δx_2
Δx_3
r_{12}
r_{23}
XBL 709-6669

Figure 1

The masses of the particles (denoted by m_1, m_2, m_3) are set equal to the atomic masses appropriate to the atoms of the system under study, or to the sum of the atomic masses of a radical if a multiatom group is being represented by a single particle. The force constants of the harmonic oscillator bonds are symbolized by k_1 and k_2, and each is either given its empirical value if it is known, or if unknown, varied as a parameter of the model; there is assumed to be no interaction between particles 1 and 3.

The dynamics of any particular problem are solved in essentially three steps. First the initial conditions are described in a convenient coordinate system and then transformed to the initial values of the normal coordinates of the system. Secondly, the motion of the system is treated by a normal modes analysis[5] and followed until the time that a critical configuration is first reached. This time is considered to be the termination of the interaction of the system. Finally, the instantaneous values of the normal coordinates and their velocities at the termination time are transformed to an appropriate coordinate system to define the final state of the system.

The initial conditions are most easily formulated in terms of Cartesian coordinates; for the present system the X coordinate (i.e. the position on the single dimension) of each particle is appropriate. However, rather than using the normal Cartesian system, the utilization of mass weighted coordinates simplifies the conversion from Cartisian coordinates to normal coordinates; this mass weighted system is defined by:

$$q_i = m_i^{1/2} \Delta X_i \qquad i = 1, 2, 3$$

where ΔX_i is the displacement of the ith particle from its equilibrium position as indicated in Fig. 1. The initial conditions can now be formulated. The initial values of the position and velocity of the center of mass may be set equal to zero without loss of generality; thus,

$$\sum_{i=1}^{3} m_i^{1/2} q_i^0 = 0 \text{ and } \sum_{i=1}^{3} m_i^{1/2} \dot{q}_i^0 = 0.$$

(Here and elsewhere the dot above a coordinate represents the time rate of change of that coordinate, and the superscript zero denotes the initial value.) To specify completely the initial conditions of the three coordinates, six independent equations are necessary; two of them are given above. The initial magnitudes of the total potential energy (V) and kinetic energy (T) yield two more equations:

$$2T = \sum_{i=1}^{3} \dot{q}_i^{0\,2}$$

$$2V = \sum_{i,j=1}^{3} f_{ij} q_i^0 q_j^0$$

where the f_{ij}'s are constants given by

$$f_{ij} = \left(\frac{\partial^2 V}{\partial q_i \partial q_j} \right).$$

For this model their values are given by

$$\underset{\sim}{f} = \begin{vmatrix} \frac{k_1}{m_1} & -\frac{k_2}{(m_1 m_2)^{1/2}} & 0 \\ \frac{-k_2}{(m_1 m_2)^{1/2}} & \frac{k_1 + k_2}{m_2} & -\frac{k_2}{(m_2 m_3)^{1/2}} \\ 0 & \frac{-k_2}{(m_2 m_3)^{1/2}} & \frac{k_2}{m_3} \end{vmatrix}$$

In an application of this model to a chemical reaction the total potential energy will be set equal to ΔD_0, the difference between the product and reactant bond dissociation energies. Now only two other equations are necessary; one must specify the coordinate values, e.g. by giving the partitioning of V between the two bonds, and the other must relate the particle velocities, e.g. by indicating the division of T between relative translational and vibrational energy. It should be noted that the initial conditions may be specified by many different sets of six equations; the above set is the easiest to define because it is the most closely related to the physically interesting parameters of the system under investigation. From all such sets, the initial values of each of the three coordinates and their velocities may be derived; this final set is the most convenient one for transformation to the intial conditions of the normal modes.

The standard methods of normal modes analysis as presented by Wilson, Decius and Cross[5] are used to follow the dynamics of the system; these methods will now be quickly sketched as they apply to this particular model. The problem is most easily formulated in terms of the two internal coordinates, $\vec{s}_1 = \vec{r}_{12} - \vec{r}_{12}^{eq}$ and $\vec{s}_2 = \vec{r}_{23} - \vec{r}_{23}^{eq}$ where $\vec{r}_{12}^{eq}$ and $\vec{r}_{23}^{eq}$ are the equilibrium distances between atoms 1 and 2 and between atoms 2 and 3 respectively (see Fig. 1). Since no bond angles need be considered in the linear model the G matrix is a function only of the atomic masses and is given simply by

$$\underset{\sim}{G} = \begin{vmatrix} \frac{1}{\mu_{12}} & -\frac{1}{m_2} \\ -\frac{1}{m_2} & \frac{1}{\mu_{23}} \end{vmatrix},$$

μ_{12} and μ_{23} are the reduced masses of atoms 1 and 2 and atoms 2 and 3 respectively. The assumption of harmonic forces only between adjacent atoms requires that the potential energy, V, be given by

$$2V = k_1 \vec{s}_1^{\,2} + k_2 \vec{s}_2^{\,2}.$$

The F matrix is thus diagonal and is given by

$$\underset{\sim}{F} = \begin{vmatrix} k_1 & 0 \\ 0 & k_2 \end{vmatrix},$$

and its inverse is simply

$$\underset{\sim}{F}^{-1} = \begin{vmatrix} 1/k_1 & 0 \\ 0 & 1/k_2 \end{vmatrix}.$$

One form of the secular equation given in Ref. 5 is

$$|\underset{\sim}{G} - \underset{\sim}{F}^{-1} \lambda| = 0,$$

where $\lambda = 4\pi^2 \nu^2$ and ν is the vibration frequency of the normal coordinate. The solution of this secular equation yields two values of λ corresponding to the two vibrational normal modes. Thus the solution to the equations of motion for these normal modes are simply

$$Q_k = K_k \cos (\lambda_k^{1/2} t + \epsilon_k) \qquad k = 1,2$$

where K_k and ϵ_k are arbitrary constants giving the amplitude and phase of the normal coordinate, Q_k, motion. Since this normal modes analysis has been formulated in terms of the internal coordinates only the two normal coordinates corresponding to the two vibrational degrees of freedom have been obtained. The required third degree of freedom is the motion of the center of mass of the system, and this corresponds to a third normal mode with $\lambda = 0$. As discussed earlier the initial conditions are defined so that the amplitude of this normal mode is intially zero and therefore it must remain at zero for all time.

Equation (13) of Section 2-4 of Ref. 5 gives the linear transformation from mass weighted Cartesian coordinates to normal coordinates, i.e.

$$Q_k = \sum_i \ell_{ik} \, q_i \qquad (1)$$

where

$$\ell_{ik} = \frac{A_{ik}}{\left[\sum_{i=1}^{3} (A_{ik})^2\right]^{1/2}}$$

and the A_{ik}'s are any solution for the set of algebraic equations

$$\sum_{i=1}^{3} (f_{ij} - \delta_{ij} \lambda_k) A_{ik} = 0 \qquad j = 1, 2, 3$$

(δ_{ij} indicates the Kronecker delta). There are, of course, three sets of ℓ_{ik}'s, one for each λ_k. Now, by the linear transformation given in Eq. (1) the initial magnitudes and velocities of the Cartesian coordinates yield the initial magnitudes and velocities of the normal modes. Simple algebraic manipulation then allows the derivation of the values of K_k and ϵ_k for each normal coordinate.

The next step is to determine the time that the interaction between the products is assumed to terminate. Since harmonic oscillator potentials have been taken to approximate the true interaction potentials, the system cannot, of course, completely separate, but would continue to oscillate indefinitely. Therefore, a critical configuration must be chosen, and at the time that the system first reaches this configuration the interaction is considered terminated. The instantaneous magnitude and velocity of each Q_k can then be calculated and the inverse transformation back to the q_i's may be made by

$$q_i = \sum_{k=1}^{3} \ell_{ik} \, Q_k \qquad i = 1, 2, 3.$$

These Cartesian coordinates and their velocities completely define the final state. Any desired parameters of this final state such as relative velocity of separation of the particles or amplitude and phase of vibration of a possible product diatomic may be easily extracted.

C. Application to "Harpooning" Mechanism

1. Introduction and Formulation

Center of mass angular distributions and nominal relative translational energies of the products have now been measured for many of the alkali atom-halogen molecule reactions.[6] The foward peaking of the MX product, the large total reactive cross section, and the relatively low translational energy of the products are all consistent with an electron transfer model.[7] Due to the high electron affinity of the halogen molecule and the low ionization potential of the alkali metal the valence electron of the alkali metal may be transfered to the molecule at relatively large internuclear distances (5 to 10Å); this transfer occurs at the distance of separation where, neglecting second order effects, the Coulomb potential energy compensates for the difference between the ionization potential and the electron affinity. The reaction then continues as an ion recombination collision. The approaching alkali ion picks up the nearest halogen atom which, because of the electrostatic attraction, must have the extra electron. The product MX then separates from the other X atom without interacting with it to a great extent. However, the angular distribution is wider and the product translational energy is larger than would be predicted for no interaction; these effects are very likely caused by repulsion between the X^- and X which are separating under the influence of the approaching M^+ ion.

The measured nominal product recoil energies, although in all cases only a small fraction of the large (typically 50 kcal/mole) exoergicities of these reactions, exhibit a general decrease with increasing alkali mass; e.g. the results for the Br_2 reactions are 6.6, 5.1, 3.7, 2.8 and 1.8 kcal/mole for Li, Na, K, Rb and Cs respectively. The great degree of similarity found for all these reaction dynamics suggests that very similar forces control the dynamics of all these reactions, and that the small, observed differences may be due to the effect of the variation of the alkali mass.

The normal modes model provides a very simple vehicle for investigating this possible mass effect. Particle 1 is assigned to be the attacking alkali atom and particles 2 and 3 represent the halogen molecule. The reactants are intially approaching each other (in a linear configuration) with a prescribed initial translational energy, E_i. The halogen molecule is assumed to be nonvibrating; thus the zero point vibrational energy is ignored. The initial positions of the three particles are set so that the exoergicity of the reaction is present as an extension of the MX bond and a compression of the X_2 bond; the fraction in each bond may be varied as desired. This configuration is intended to approximate the state of the reaction partners at the moment that the electron is transfered. These specifications in conjunction with the constraints mentioned in the preceeding section completely determine the initial position and velocity of each particle. It should be mentioned here that k_2 and r_{23}^{eq} are not expected to be the values found for the X_2 molecule; when the electron is transferred, it is very likely that the resultant X_2^- ion will have considerably different bonding characteristics from the neutral X_2

molecule. The absolute value of r_{23}^{eq} (as well as that of r_{12}^{eq}) does not enter the calculation, but the magnitude of k_2 which does require an explicit value will be varied as a parameter of the model.

The reaction is now allowed to proceed until r_{23} reaches r_{23}^{eq}. At this time particle three is assumed no longer to interact with the MX molecule. Expansion of r_{23} into normal coordinates and solution for the termination time results in a transcendental equation. If $E_i = 0$, analytical expression for the upper and lower bounds on the first solution may be determined; then this solution may be calculated to as high a degree of accuracy as desired. However, for nonzero E_i an iterative process is necessary. The value of r_{23} is calculated at each incremental time spacing until it passes through r_{23}^{eq}; then, as in the former case, the time may be found to any degree of accuracy. The time spacing used in the iterative process is 1 to 4 percent of the period of the normal mode with the largest vibrational frequency. Once this termination time has been evaluated, the relative translational energy of the products and the vibrational excitation of the MX molecule are easily calculated.

2. Results and Discussions

Figure 2 shows the results of the calculations of the product translational energies for these systems. The abcissa of this graph is the ratio of the alkali mass to the halogen mass. This is appropriate because, for a given potential energy surface, the classical trajectories are not altered if the masses of all the particles of the system are changed by the same factor;[8] the speed at which these trajectories are traversed, however, varies as the inverse of the square root of that factor. Each of the calculated curves of Fig. 2 are labeled with a

Figure 2. Prediction of energy partitioning as a function of particle mass ratio. The decimal and percentage numbers labeling the curves give the value of the ratio k_2/k_1 and the percent of the reaction exoergicity included as X-X repulsion, respectively. The data points give the experimental measurements of the nominal energy partitioning of the indicated reactions.

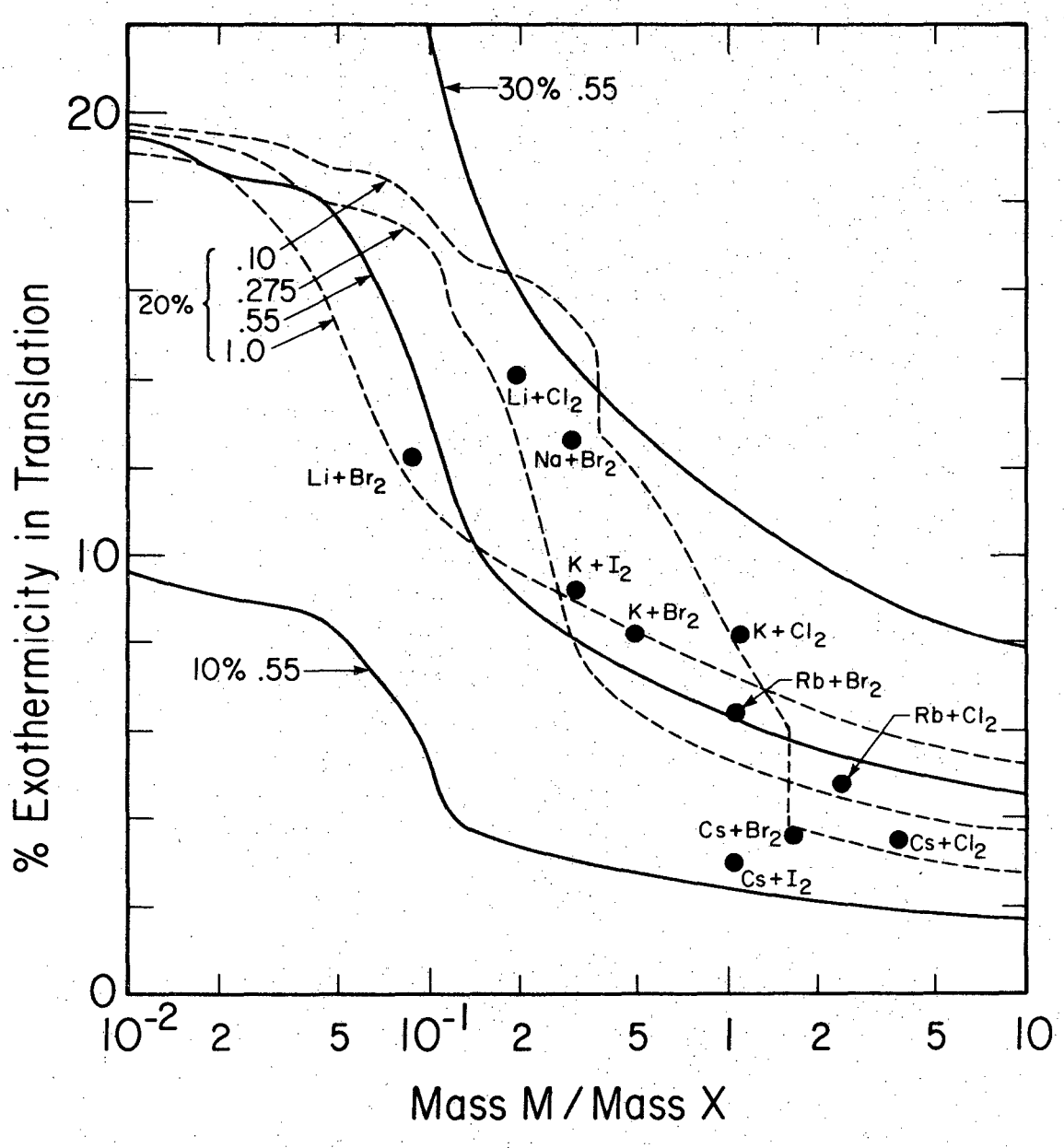

XBL 709-6670

Figure 2

decimal number indicating the ratio of k_2/k_1 and a percentage giving R which denotes the fraction of the reaction exoergicity included as repulsion between the two halogen atoms. Changing both force constants by the same factor is equivalent to multiplying each of the coordinates of the potential energy surface by the square root of that factor (for an example of such a potential energy surface see Fig. 1 of the following chapter.) Such a coordinate scale change does not affect the energy partioning which is a function of the ratio of the force constants; however, the trajectory transversal time, for a given force constant ratio, is directly proportional to the inverse of the square root of the magnitude of the force constants. As one would expect from the harmonic oscillator characteristics of this model, the fractional energy partitioning and the time to traverse the trajectory are constant if both V and T are multiplied by the same factor. This multiplication simply increases the amplitude of each normal coordinate by a proportional amount, but it does not affect the frequencies nor the phases of the normal modes. Consequently, for $E_i = 0$ the curves of Fig. 2 are independent of the total reaction exoergicity. The percent of reaction exoergicity that appears in product translation may be calculated for the reactions of the alkali atoms with the homonuclear halogen molecules from experimentally measured quantities. Thus, the available experimental results may be directly compared with the predictions of the model on the single graph presented in Fig. 2.

All of the calculated curves for the reasonable range of parameters have several features in common. If the attacking alkali has a very light mass, one hundred percent of R enters the translational energy of product

separation. This feature arises because the relatively slow separation of the X_2 molecule takes place essentially independently of the rapid vibration of the MX molecule. This limit is closely approached on the left side of Fig. 2 by all of the calculated curves. This effect of the light mass has been noted previously,[8] and has been labeled the "light-atom anomaly". As the alkali mass becomes comparable to the mass of the halogen atom, the translational energy decreases rapidly due to the heavier mass of the alkali atom allowing it to act as an anchor and thereby pulling the nearest halogen toward itself. Since the transferred halogen ion is departing from the spectator halogen atom at an increased rate, the repulsive force is less effective in imparting translational energy to the departing atom. This can be explained by the fact that the repulsive force acts on the spectator atom through a smaller distance than it would if the massive alkali atom were not present. Thus, all of R does not appear as product translation; a significant fraction is converted into MX vibration. This effect has been labeled "mixed energy release" and has been discussed previously.[8] As the mass of the alkali atom is increased still further, the translational energy continues to decrease but approach a non-zero limit for infinite mass. Second order effects due to the varying number of oscillations of the MX bond during the period of X-X interaction are responsible for the small undulations superimposed on the general decrease. The slope of this general decrease is not constant however; a precipitous drop is common to all of the calculated curves. This drop occurs when the magnitude of the vibration of the MX molecule during the X-X separation approaches one-half of a vibrational oscillation. If the MX bond is contracting during the complete

time that the halogens are separating, the mixed energy release is greatly enhanced. Since as r (the alkali to halogen mass ratio) is increased this half period criterion is approached first by the largest k_2/k_1 ratio, the resultant translational energy is smallest for this largest k_2/k_1 ratio at small r.

It is useful to consider the results presented in Fig. 2 with reference to the impulsive limit. At this limit all of R is initially released as translational energy of relative motion of the two halogens. Thus the X-X separation takes place without any influence from the presence of the M^+ ion. The free X^- ion then combines with the M^+ ion to form the MX molecule. This limit is approached when $k_2 \gg k_1$. At this limit the final partitioning of R between relative product translational kinetic energy and internal excitation of the MX molecule may be easily determined from conservation of momentum considerations (this determination is fully discussed in the following chapter). Alternatively, the f_m factor which is defined in Eq. 12 of Ref. 2a gives the fraction of R that appears as vibrational excitation of the product diatomic at the impulsive limit. If r is allowed to represent the ratio of the alkali mass to the halogen mass, Eq. 12 of Ref. 2a reduces to

$$f_m = \frac{r}{2r + 2} .$$

Thus, at the impulsive limit, light M($r \ll 1$) gives $f_m = 0$ and all of R appears as product translation, but for heavy M($r \gg 1$) $f_m = 1/2$ and fifty percent of R is channeled into product translation. As r is increased f_m monotonically increases. On the right of Fig 2, it is evident that less product translational energy is present than would be predicted at the impulsive limit. For a larger value of k_2/k_1, the system is closer

to the impulsive limit; this is the reason that the product translation is greatest for the largest k_2/k_1 ratio at large r.

As may be seen in Fig. 2, the experimental data exhibit a rough correlation with the model results for 20 percent repulsive energy release and a force constant ratio of approximately 0.275 to 0.55. This correlation is by no means exact, but in view of the very approximate nature of the nominal recoil energy measurements, it is certainly as good as could have been hoped. In short the experimental results are certainly consistent with a mass effect of the magnitude predicted by this model. Furthermore the departures from an exact correlation cannot be due completely to a failure of this model to account adequately for all important facets of the reaction dynamics; it is evident that the same potential energy surface cannot reproduce the experimental results for all these systems. The reaction pair, $Na+Br_2$ and $K+I_2$, and the three reactions, $K+Cl_2$, $Rb+Br_2$ and $Cs+I_2$, form two sets of systems such that each member of a given set has nearly the same alkali to halogen mass ratio. As mentioned previously the energy partitioning is independent of the magnitude of the mass of the reactants, and therefore observed experimental differences within each set can only be attributed to differences in the systems' potential energy surfaces or to a failure of the measured, nominal product translational energy to reflect adequately the true energy partitioning.

It should be emphasized that the linear configuration does not limit this model to treatment of solely collisions occurring with zero impact parameter. Reactive events may occur with M and X_2 in a linear configuration but traveling (in the center of mass system) in parallel but non-coincident

paths; these collisions would be much more probable than "head-on" collisions. For this reason all the calculations presented here are for zero initial kinetic energy since the kinetic energy appropriate to this model is that due to the component of relative velocity of approach that lies along the line defined by the colinear configuration. The magnitude of this energy would vary between the total initial relative translational kinetic energy and zero; the lower values would have a higher probability. Calculations have been carried out with E_i = 1, 2, 4 and 6 percent of ΔD_0 for k_2/k_1 = .55 and 20% repulsion; the resultant curves were very similar in shape to that for E_i = 0 shown in Fig. 1 but at large mass ratio much lower limit were approached.

One other interesting feature of these calculations deserves comment. The reaction lifetime (i.e. the time for the X-X distance to reach its equilibrium value) generally decreases as the mass ratio increases. Thus one must reach the striking conclusion that the lifetime of a reaction of Li must be longer than the lifetime of the same reaction with Cs. This effect is present because the alkali atom pulls the nearest halogen atom to itself; when the mass ratio is large, this tug is relatively efficient and the halogen atoms quickly separate, but when the alkali atom is very light relative to the halogen, the force rapidly accelerates the alkali atom but only slightly affects the halogens. Concomitant with the longer reaction lifetime at low mass ratios is a greater complexity of interaction between the alkali and the nearest halogen. The light alkali more rapidly approaches the separating halogen molecule, but before it can completely separate, the M atom reaches its equilibrium position and then begins to repel the halogen atom. This retards the separation of the halogens and

enhances the likelihood of secondary encounters. This effect would be expected to correlate roughly with the width of the angular distribution of the products, and the reactions with the smallest mass ratios have indeed exhibited the broadest distributions.[6] An extended discussion of these more complex interactions has been given to explain some results observed in three dimensional trajectory studies of these experimental systems.[9c]

Polanyi and co-workers[2a] have utilized a model very similar to that presented here to investigate the dependence of the energy partitioning on the percent repulsive energy release and on the ratio of the initial attractive M-X force to the repulsive X-X force. The parameters of their model were not intended to represent directly any physical system, but were selected to investigate conveniently the effect of mixed energy release. Without repeating their calculations our results cannot be quantitatively compared with theirs, but qualitative comparisons indicate that the conclusions are mutually consistent. Since their model assumes three particles of equal mass, comparisons should be made to our calculations for the mass ratio equal to one. Several common conclusions appear in the two studies: if the fraction of repulsive energy release is small ($\leq 30\%$), very little energy is channeled into product translation and thus the repulsion must be efficient for exciting vibrational motion in the MX bond; the principal effect of increasing E_i is the reduction of the resultant product translational energy; an increase of the force constant ratio generally yields an increase of product translational energy, but for low force constant ratio values singularities in the calculated results are observed (see Fig. 2).

In summary it appears that a significant mass effect may be a large factor in the cause of the observed differences in the energy partitioning observed for this set of reactions. From the parameters necessary to fit the data a prediction may be made for the general features of the potential energy surface that would be required for exact, classical trajectory calculations. The energy released as product repulsion should be near 20% and the force between the halogen atoms during the initial part of the separation when the majority of R is released, and the magnitude of the initial attractive force between M and X must reflect the relative values of the initial forces that correspond to the range of force constant ratios that was found to be appropriate here. Three trajectory calculation studies have been reported;[9] each used a different surface to approximately fit the experimental results. Surface III-A of Ref. 9(b) is the best surface found in that study; a qualitative glance indicates that it does indeed approximately conform to the predictions made above.

When detailed product velocity analysis becomes available, for these reactions[10] much more reliable values of the energy partitioning can then be compared with the results of this model. It may then be of value to investigate these systems in greater detail. In particular it would seen likely that the repulsive energy release would be primarily a function of the halogen molecule and relatively independent of the alkali atom. If this is the case, comparison of the reactions of all the alkali atoms with a given halogen molecule would perhaps yield significant information concerning the amount of repulsive energy release and the magnitude of the repulsive force for each halogen diatomic negative ion.

REFERENCES

1. This work is reviewed in D. Rapp and T. Kassel, Chem. Rev. 69, 61 (1969).

2. (a) P. J. Kuntz, E. M. Nemeth, and J. C. Polanyi, J. Chem. Phys. 50, 4607 (1969) interpret their exact trajectory calculations of the energy partitioning for these reactions in terms of such a model; (b) D. D. Parrish and R. R. Herm, J. Chem. Phys. 51, 5467 (1969) qualitatively discuss the experimentally observed variations in energy partitioning with changing alkali mass for these reactions in terms of this model.

3. D. D. Parrish and R. R. Herm, J. Chem. Phys. 53, 2431 (1970). See also the following chapter which incorporates some extensions with the above work.

4. R. W. Zwanzig, J. Chem. Phys. 32, 1173 (1960); B. McCarroll and G. Ehrlich, J. Chem. Phys. 38, 523 (1963).

5. E. B. Wilson, Jr., J. C. Decuis, and P. C. Cross, Molecular Vibrations (McGraw Hill Book Co., New York, 1955).

6. See D. D. Parrish and R. R. Herm, J. Chem. Phys. 51, 5467 (1969) for the latest results. The earlier studies are cited therein.

7. See the review article: D. R. Herschbach, Adv. Chem. Phys. 10, 319 (1966).

8. This fact was pointed out in P. J. Kuntz, E. M. Nemeth, J. C. Polanyi, S. D. Rosner, and C. E. Young, J. Chem. Phys. 44, 1168 (1966).

9. (a) N. C. Blais, J. Chem. Phys. 49, 9 (1968), N. C. Blais, J. Chem. Phys. 51, 856 (1969). (b) M. Godfrey and M. Karplus, J. Chem. Phys. 49, 3602 (1968). (c) Ref. 2a and P. J. Kuntz, M. H. Mok, and J. C. Polanyi, J. Chem. Phys. 50, 4623 (1969).

10. For two systems these results have been published: (a) $K+Br_2$, A. E. Grosser and R. B. Bernstein, J. Chem. Phys. 43, 1140 (1965), and J. H. Birely and D. R. Herschbach, J. Chem. Phys. 44, 1690 (1966). (b) $K+I_2$, K. T. Gillen, Ph.D. Thesis, University of Wisconsin, 1970.

V. APPLICATION OF LINEAR, NORMAL MODES MODEL TO THE REACTIONS OF THE ALKALI METALS WITH ALKYL IODIDES

A. Introduction

The reactions of the alkali metals with the alkyl iodides have been the subject of extensive investigations in crossed molecular beams.[1] Product velocity analysis of the reactive scattering of these systems was not included in the studies of Ref. 1(a)-(d), but these additional data have now been collected for the reactions of the heavier alkali metals.[2] The full results of these later experimental studies have not yet been published, but two striking qualitative results have been revealed. In the reactions of the series $Cs+I\text{-}R' \rightarrow CsI+R'$, where R' is methyl, ethyl, n-propyl, or n-butyl radical, the CsI is observed to be formed with roughly the same center-of-mass (CM) speed irrespective of the R' group.[3] Since the exoergicity of these four reactions are very nearly equal, energy conservation requires that in order for the above observation to be true, the internal excitation of the products must increase as R' is varied from methyl to butyl. Secondly, in the series of reactions $M+I\text{-}CH_3 \rightarrow MI+CH_3$ where M is Cs, Rb or K, the MI product is observed to be formed with approximately the same CM momentum regardless of the mass of the alkali atom.[4] The model developed in the preceeding chapter is here extended and applied to these two series of reactions.

The $M+ICH_3$ reactions have been extensively investigated by exact, classical trajectory studies.[5] Unfortunately, the potential energy surfaces chosen for these studies were selected to yield product translational energies in agreement with the experimental results that were indicated at the time the theoretical investigations were initiated. Improved

kinematic analysis techniques[1a] have shown that these early experimental results were significantly lower than the presently accepted values. Consequently, the theoretical investigations can no longer be taken as indicative of the dynamics of these particular reactions. Much less attention has been given to the reactions of the heavier alkyl iodides, although Raff[6] did report exact three-dimensional trajectory study comparisons of the $K+IC_2H_5$ and ICH_3 reactions. In addition, Ottinger[3] has reported exact computer solutions of the energy partitioning in the Cs + methyl, ethyl, n-propyl, and n-butyl iodide reactions for a one-dimensional linear collision; his model treated each CH_2 or CH_3 group as a separate particle and his potential energy of interaction between the particles is more sophisticated than that considered here. Nevertheless, his calculation failed to fit the observed constancy of the CsI product CM speed with changing R' group.

The following application of the harmonic oscillator model to the Cs+IR' reactions will (1) show that the observed approximate constancy of the CsI CM speed can be accounted for in the impulsive limit, where the R'-I repulsion is the dominant force in the collision, (2) argue that the model should, in fact, provide fairly reliable estimates of the actual energy partitioning because the observed reaction features are so near the impulsive limit, (3) indicate that one should observe substantial internal excitation in the R' product, with the possible exception of the methyl group, and (4) provide a qualitative indication of the important forces, which should help to provide guidelines for the selection of an appropriate potential energy surface for any future exact trajectory calculations for these reactions.[7] In addition, the model parameters that prove most successful

in reproducing the constant CsI velocity, will be taken without further adjustment to account for the approximate equality of the product CM momentum for the reactions of K, Rb and Cs with methyl iodide. This trend will be predicted to continue for the two lightest members of the alkali family, Li and Na, but the predicted reaction dynamics are significantly different for these two alkalis and observable differences in the product energy distributions may result. Experimental studies intended to determine these as yet uninvestigated features are currently planned in this laboratory.

B. Formulation

The methyl iodide reactions may be treated directly by the model formulated in the preceding chapter, but the reactions of the heavier alkyl iodides with Cs are more reasonably treated by an extended model. The reaction of Cs+I-CH_3 has been treated by both models to allow comparison of results. The extended model will now be discussed.

The reaction is treated as that of four particles, with R' = CH_2-R, which are constrained to a linear, one-dimensional collision with the bonds labeled as shown in Fig. 1. The particles are given the atomic masses of Cs and I for the first two particles and the sum of the atomic masses of CH_2 and R for the second two particles, where R is H, CH_3, C_2H_5, or C_3H_7. Thus, this model treats the hydrocarbon radical, CH_2-R, as a diatomic molecule and so predicts the same behavior for Cs + n-butyl and i-butyl iodide, whereas Cs + i-propyl, s-butyl, and t-butyl iodides are not considered. The potential energy is given in terms of Δ_1, Δ_2, and Δ_3, the displacement of each bond length from its equilibrium value, r_i^e (i.e. $\Delta_i = r_i - r_i^e$), as

Figure 1. Effective potential energy surface, with energies given in kcal/mole, for r_3 held at its equilibrium configuration. The " + " mark denotes the starting point of a reactive trajectory for 19.0 kcal/mole repulsion; Δ_i equals the displacement of r_i from its equilibrium value.

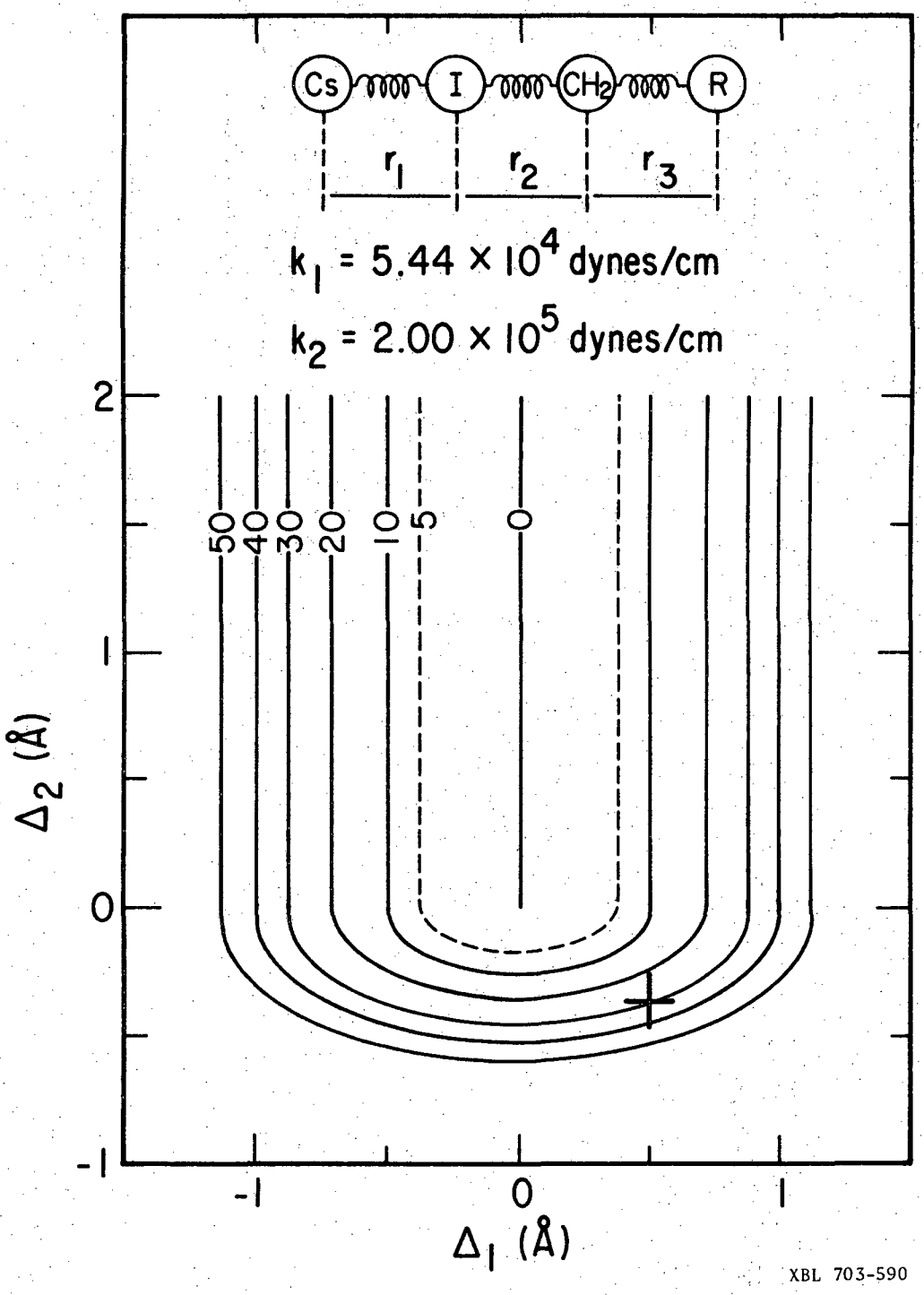
Cs
I
CH2
R
r1
r2
r3
k1 = 5.44 × 10^4 dynes/cm
k2 = 2.00 × 10^5 dynes/cm
50
40
30
20
10
5
0
2
1
0
-1
Δ2 (Å)
-1
0
1
Δ1 (Å)
XBL 703-590

Figure 1

$$V(\Delta_1, \Delta_2, \Delta_3) = 1/2\, k_1\Delta_1^2 + 1/2\, k_2\Delta_2^2 + 1/2\, k_3\Delta_3^2 \;,\; \Delta_2 < 0$$
$$= 1/2\, k_1\Delta_1^2 + 1/2\, k_3\Delta_3^2, \quad \Delta_2 \geq 0. \qquad (1)$$

The force constants k_1 and k_3 are taken as equal to those in a conventional Cs-I and C-C bond respectively, whereas r_1^e and r_3^e do not enter into the calculations; thus, k_1 and k_3 are 5.44×10^4 dynes/cm^8 and 4.33×10^5 dynes/cm^3 respectively. The I-CH_2 force constant, k_2, is varied as a parameter of the model.

At the start of the reaction all four particles are stationary, i.e., $\dot{\Delta}_1^{(0)} = \dot{\Delta}_2^{(0)} = \dot{\Delta}_3^{(0)} = 0$. Further, $\Delta_3^{(0)} = 0$, $\Delta_2^{(0)} < 0$ and $\Delta_1^{(0)} > 0$ such that ΔD_0, the difference in CsI and I-CH_2 bond dissociation energies, is equal to $V(\Delta_1^{(0)}, \Delta_2^{(0)}, 0)$. Thus, $V(\Delta_1, \Delta_2, \Delta_3)$ has the correct limit of zero as $\Delta_2 \rightarrow +\infty$ for $\Delta_1 = \Delta_3 = 0$; however, the limiting behavior for separated reactants ($\Delta_1 \rightarrow +\infty$) is wrong and this model effectively assumes that the very slowly approaching Cs and I-CH_2-R feel no force until a critical Δ_1 is reached, whereupon Eq. (1) applies and reaction is certain to take place. The energy intially present in compression of the I-CH_2 bond, $1/2\, k_2\Delta_2^{(0)2} = P$, is referred to as the repulsion and can be easily varied as a second parameter of the model while maintaining the total exothermicity, ΔD_0, constant by simultaneously changing the value of $\Delta_1^{(0)}$. The exothermicities of all these reactions are approximately the same and were taken as $\Delta D_0 = 28.7$ kcal/mole.[9]

Having fixed these initial conditions, the subsequent classical motion of the system is followed by a normal coordinates analysis; the reaction is assumed to be completed when Δ_2 goes through zero. At this point the products are assumed to stop interacting and the partitioning of

the reaction exothermicity is determined by decomposing the instantaneous vales of the normal coordinates and their time derivatives into vibrational energy in each of the two product diatomics and relative translational kinetic energy of separation, E'. Figure 1 shows an effective potential energy surface for a k_2 value which is found to best fit the experimental observations. The initial r_2 distance is 2.18Å, the equilibrium C-I distance in ethyl iodide,[10] representing a .36Å compression from the C-I distance where the I-CH_2 repulsion drops to zero; the initial r_1 distance is 3.82Å, the resultant of a .50Å extension of the 3.32Å equilibrium Cs-I distance reported in Ref. 8.

It is very artificial to treat the methyl group as CH_2-H where the force constant is set equal to the C-C bond force constant. Consequently the calculations for the methyl iodide reactions have been carried out using the three particle model of the preceding chapter. Particle three represents the methyl radical and its mass is set equal to the sum of the atomic masses of CH_3.

C. Results

The solid curves of Fig.2 give the best results of the four particle model. The 19.0 kcal/mole in repulsion is dictated by the necessity of matching the observed CsI CM product speed from the Cs+CH_3I reaction; this velocity varies, approximately, as the square root of the repulsion over the whole range of I-CH_2 force constants. Figure 2 also presents the results for Cs+I-CH_3 when the more realistic three particle model is used for this reaction; over most of the range in k_2 the two calculations agree, and the slight difference at very high k_2 values is simply due to the greater velocity imparted to the I atom upon recoiling off of the heavier CH_3 group.

Figure 2. Plot of product CsI CM speed versus the I-CH_2 force constant for 19.0 kcal/mole repulsion. The solid curves give the results of the four particle Cs-I-CH_2-R calculations. The dashed curve deviating from the Cs-I-CH_2-H solid curve for high force constant values presents the results of the three particle calculation for Cs-I-CH_3; at lower force constants, this is indistinguishable from the four particle calculation. The dashed lines give the experimentally observed CsI CM speeds cited in Ref. 3. The dotted lines on the left give the adiabatic limits, where the repulsion is released so slowly that it must all appear as product translational energy. The dotted lines in the middle of the force constant range give the three particle impulsive limit (never reached) in which the I impulsively kicks off of the "CH_2-R particle."

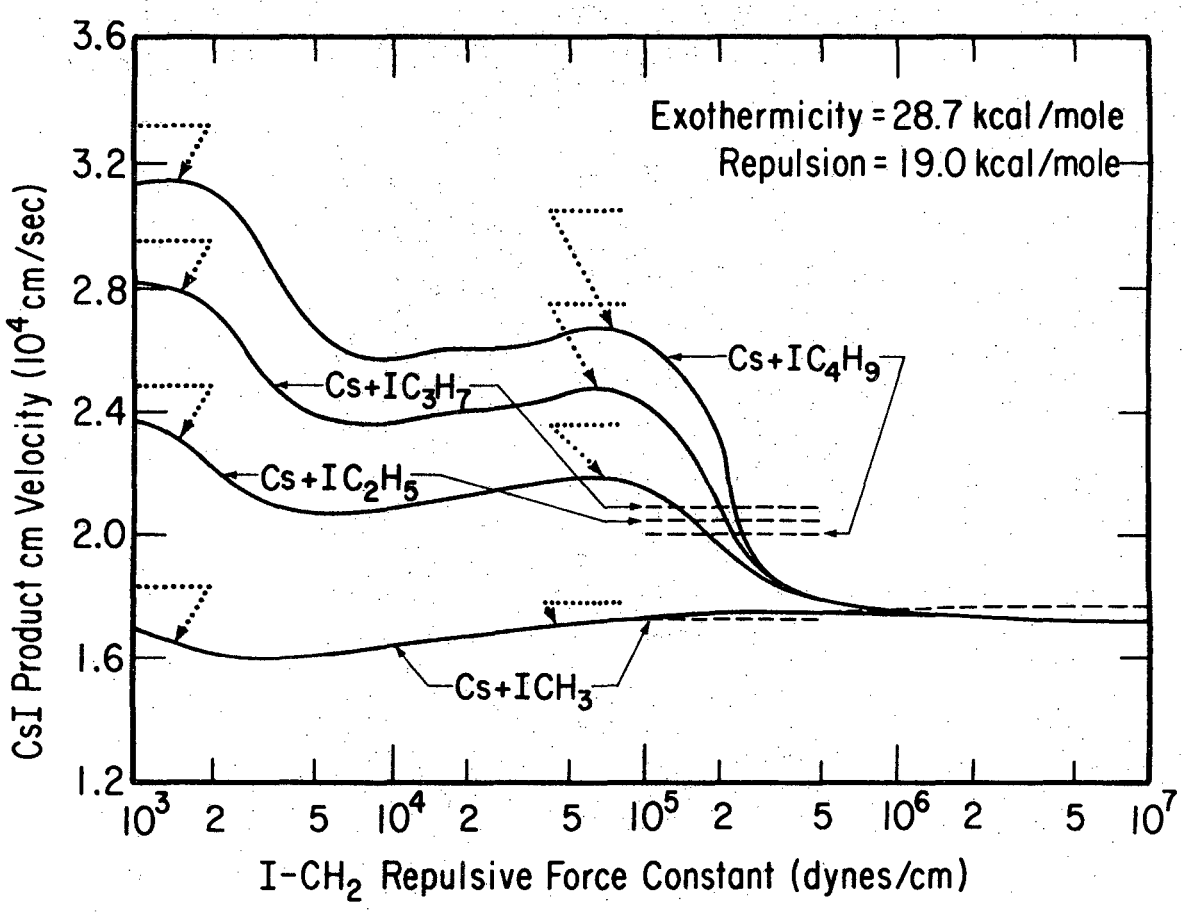

XBL 703-492

Figure 2

For the results presented in Fig. 2, it is possible to examine three limiting cases in which the dynamics may be understood as two particle interactions. The first of these, the adiabatic limit, is approached on the far left of the drawing where the I-CH_2 force constant is so weak relative to those of Cs-I and CH_2-R that these two diatomics separate as if they were single particles. Thus, the full repulsion must appear as kinetic energy of separation, E', so that the CsI CM product speed is given in terms of $\mu_{CsI-CH_2R} = m_{CsI}m_{CH_2R}/M$ ($M = m_{CsI}+m_{CH_2R}$) by

$$u_{CsI} = m_{CsI}^{-1}\{2P\mu_{CsI-CH_2R}\}^{1/2}; \qquad (2)$$

u_{CsI} can never exceed this limiting value. The striking aspect of Fig. 2, with respect to this limit, is the large deviation of the actual calculation from the limit even for the smallest value of k_2 examined. In the second limit, a three particle impulsive limit, the I-CH_2 force constant would greatly exceed that of CsI but be less than that of CH_2-R so that the I atom would recoil from the rigid CH_2R group and thus

$$u_{CsI} = m_{CsI}^{-1}\{2P\mu_{I-CH_2R}\}^{1/2} \qquad (3)$$

where $\mu_{I-CH_2R} = m_I m_{CH_2R}/(m_I+m_{CH_2R})$. Although this limit is never reached for the values of k_1 and k_3 chosen here, it indicates the physical origin of the rapid rise shown in Fig. 2 of the ethyl, propyl, and butyl iodide curves as k_2 is decreased from its high limit.

The third limit, the two particle impulsive limit, occurs when k_2 becomes much greater than either k_1 or k_3 so that the entire repulsion appears as recoil of I from CH_2; in this case,

$$u_{CsI} = m_{CsI}^{-1}\{2P\mu_{I-CH_2}\}^{1/2} \qquad (4)$$

where $\mu_{I\text{-}CH_2} = m_I m_{CH_2}/(m_I+m_{CH_2})$. The results of Fig. 2 show that this limit is reached for $k_2 \gtrsim 10^6$ dynes/cm where the curves for all four reactions coalesce to the value given by Eq. (4). The qualitative shapes of the curves shown in Fig. 2 are similar over a wide range of repulsions from 5 to 25 kcal/mole, although, of course, the magnitude of the CsI speed varies with the repulsion; in particular, the impulsive limit is reached for $k_2 \gtrsim 10^6$ dynes/cm over this entire range of repulsions.

The near equivalence of the experimental CsI CM speeds indicate that the reaction dynamics must be near this impulsive two particle limit.[11] This is of added interest to a model such as that presented here, which no doubt greatly oversimplifies the actual forces, because at the impulsive limit the energy partitioning is solely dependent on the fraction of the reaction exothermicity released as $I\text{-}CH_2$ impulsive repulsion; thus, the use of such a simple force model to explain small departures from the impulsive limit might be assigned a good deal of credence, whereas application of the same model to another reaction system far removed from this limit might be of much more questionable usefulness. Figure 2 indicates that the slight differences in the experimental CsI CM speeds for these four reactions are best fit by a k_2 somewhat below the impulsive limit, i.e., $k_2 = 2\times10^5$ dynes/cm; Table I indicates the quantitative extent of agreement of the experimental data and the model for this value of k_2. Although there is no a priori reason to expect it, it is interesting to note that this value of k_2 is close to the C-I force constant in the alkyl iodides, where $k_{C\text{-}I}=2.6\times10^5$ dynes/cm.

TABLE I. Product Energy Partitioning for the Cs + Alkyl Iodide Reactions[a]

Reaction	Experimental[b]	Calculated[c]		
	CsI CM Velocity	CsI CM Velocity	CsI Vibration Energy	CH_2-R Vibration Energy
$Cs + ICH_3$	1.73	1.74	11.49	.03
$Cs + IC_2H_5$	2.05	1.96	12.03	4.77
$Cs + IC_3H_7$	2.09	2.10	12.41	6.71
$Cs + IC_4H_9$	2.00	2.32	13.15	6.32

[a] Vibrational energies are given in kcal/mole, CsI CM velocities in units of 10^4 cm/sec.

[b] Experimental results cited in Ref. 3.

[c] Results for exothermicity = 28.7 kcal/mole, repulsion = 19.0 kcal/mole, and I-CH_2 force constant = 2.0×10^5 dynes/cm.

It is also of interest to examine the partitioning of the product vibrational excitation between Cs-I and CH_2-R. These data are presented in Fig. 3 and the particular values shown in Fig. 3 for $k_2 = 2\times10^5$ dynes/cm are presented in Table I as well. In the adiabatic limit, CH_2-R is unexcited and CsI appears with the vibrational energy initially put into Cs-I stretch, $1/2k_1\Delta_1^{(0)2}$. In the two particle (I-CH_2) impulsive limit, the vibrational excitation in Cs-I and CH_2-R may once again be calculated from conservation of energy and linear momentum; the curves in Fig. 3 are near these limits for $k_2 \gtrsim 10^6$ dynes/cm. Figure 3 illustrates that the Cs-I vibrational excitation is well above the adiabatic limit over the whole range of k_2 values studied. However, the most striking feature of Fig. 3 is the very sharp rise in the vibrational excitation of CH_2-R as k_2 is increased from 1 to 5×10^5 dynes/cm. Since this range includes the k_2 value necessary to best fit the CsI CM speed, it suggests that the CH_2-R internal excitation is probably the experimentally measureable energy partitioning parameter which is most sensitive to the form and strength of the I-CH_2 repulsion; unfortunately, this is the energy partitioning parameter which is probably most difficult to determine experimentally.

The CM momentum of the MI products from the alkali metal-methyl iodide reactions may now be calculated from the three particle model by setting the repulsive energy release equal to 19 kcal/mole and k_2 equal to 2×10^5 dynes/cm; these values best fit the former results and thus are not adjusted further. The results of these calculations are included in Table II; also shown are the empirical values of ΔD_0 and k_1. These experimental values were used to derive the results shown except for the Na+CH_3I reaction where

Figure 3. Vibrational excitation of the product diatomics: solid curves for Cs-I and long-dashed curves for CH_2-R. The short-dashed lines at the limiting low and high I-CH_2 force constants give the adiabatic and two particle impulsive limits for the Cs-I excitation.

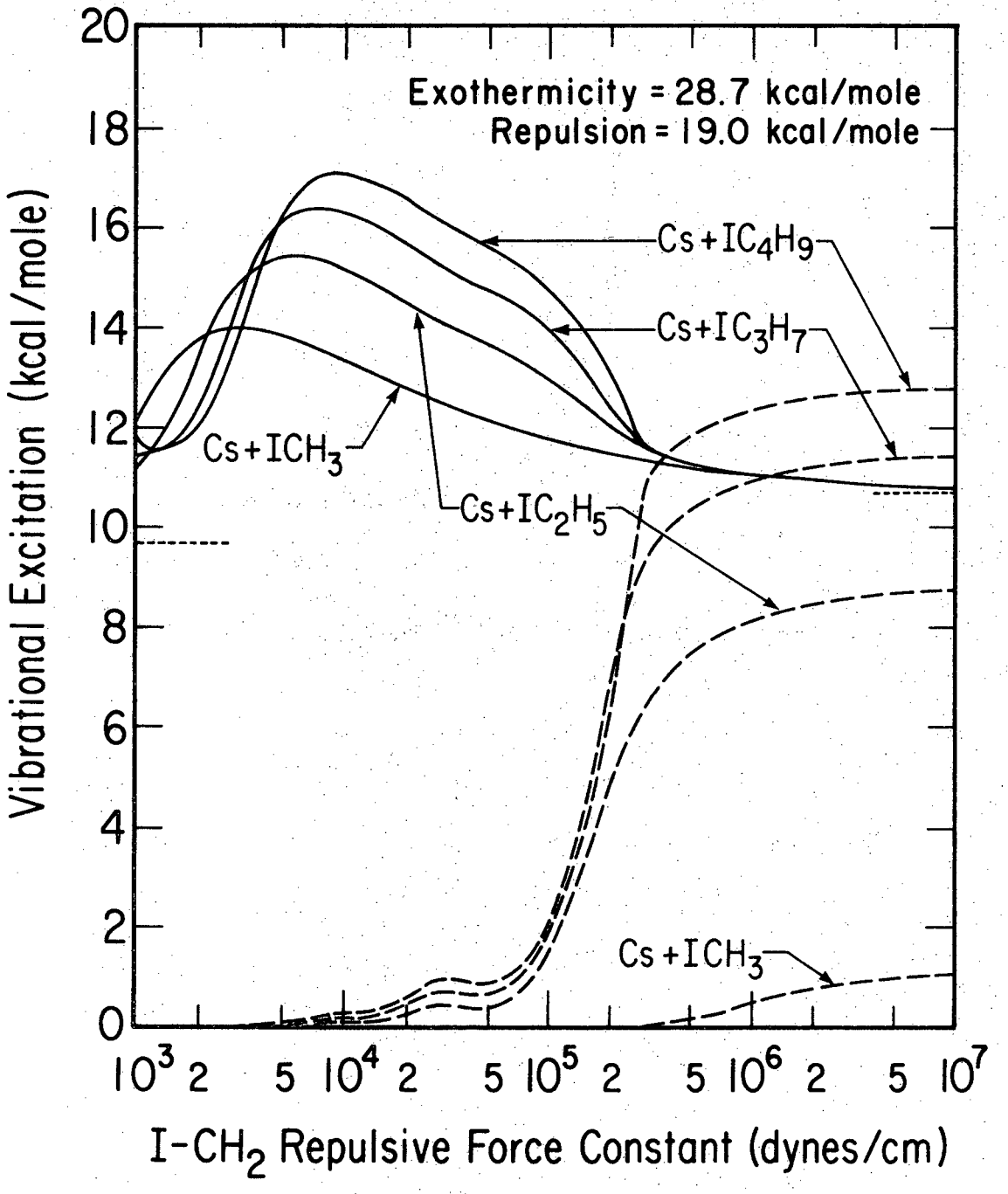

XBL 703 -491

Figure 3

TABLE II. Product CM Momentum for the Alkali Metal + Methyl Iodide Reactions[a]

Reactions	ΔD_0[b]	k_1[c]	Calculated[d] MI CM Momentum	Experimental[e] MI CM Momentum
Li + CH_3I	30.3±2	9.38	450.0	---
Na + CH_3I	18.4±2	7.70	462.6	---
K + CH_3I	22.5±2	6.11	456.1	---
Rb + CH_3I	22.4±2	5.75	456.4	---
Cs + CH_3I	28.1±2	5.43	452.8	449

[a] ΔD_0 given in kcal/mole. Momentum given in 10^4 gm-cm/sec/mole. k_1 given in 10^4 dynes/cm.

[b] $\Delta D_0 = D_0$ (MI) - D_0 (CH_3-I) is the reaction **exoergicity.** Bond dissociation data were taken from Ref. 9. For the Na + CH_3I reaction it was necessary to carry out the calculation for ΔD_0 = 19.0 kcal/mole in order to allow 19.0 kcal/mole to be included as product repulsion.

[c] Calculated from data given in Ref. 8.

[d] Results for repulsion = 19.0 kcal/mole and I-CH_2 force constant = 2.0×10^5 dynes/cm.

[e] Calculated from the results presented in Ref. 3.

ΔD_0 was set equal to 19.0 kcal/mole in order to allow the repulsive energy release to equal 19.0 kcal/mole. The results agree well with the one experimental value that is available and with the near constancy of the product MI CM momentum observed for the three heavier alkali metals. This constancy is a direct result of the fact that all three systems are very near the $I\text{-}CH_3$ two particle impulsive limit where the momentum is given by

$$\vec{M}_{IMP} = (2P\mu_{I\text{-}CH_3})$$

where $\mu_{I\text{-}CH_3} = m_I\, m_{CH_3}/(m_I+m_{CH_3})$. For P = 19.0 kcal/mole, $\vec{M}_{IMP} = 462.5$ (in units of 10^4 g-cm/sec/mole). Figure 4 presents the energy partitioning as a function of k_2 over a very extended range in order to fully demonstrate the impulsive and adiabatic limits with the intermediate region where the MI oscillator absorbs significant amounts of energy. The impulsive limits are indicated on the right by the dotted lines and were calculated from $\vec{M}_{IMP}$. At the adiabatic limit which is closely approached at the left of Fig. 4, the full P = 19.0 kcal/mole enters the product translational kinetic energy. The secondary undulations apparent in the curves are due to the varying number of MI vibrational oscillations that take place during $I\text{-}CH_3$ separation. The vibrational excitation of the MX molecule may be simply obtained by subtracting the product translational kinetic energy from ΔD_0.

D. Discussion

1. Cs + IR' Reaction Series

The model presented here is very simplified in many respects: linear, four-particle configuration, no initial translational energy or reactant excitation, and very idealized forces. Ottinger[3] presents arguments to

Figure 4. Energy partitioning in the M + $I\text{-}CH_3$ reactions as a function of k_2. The dotted lines on the right indicate the impulsive limit for each reaction; for Na + $I\text{-}CH_3$ this limit coincides with the solid curve. The Li + $I\text{-}CH_3$ results are presented as a dashed curve only to differentiate it from curves it crosses. The vertical dashed line indicates $k_2 = 2\times10^5$ dynes/cm which was used in the calculations presented in Table II.

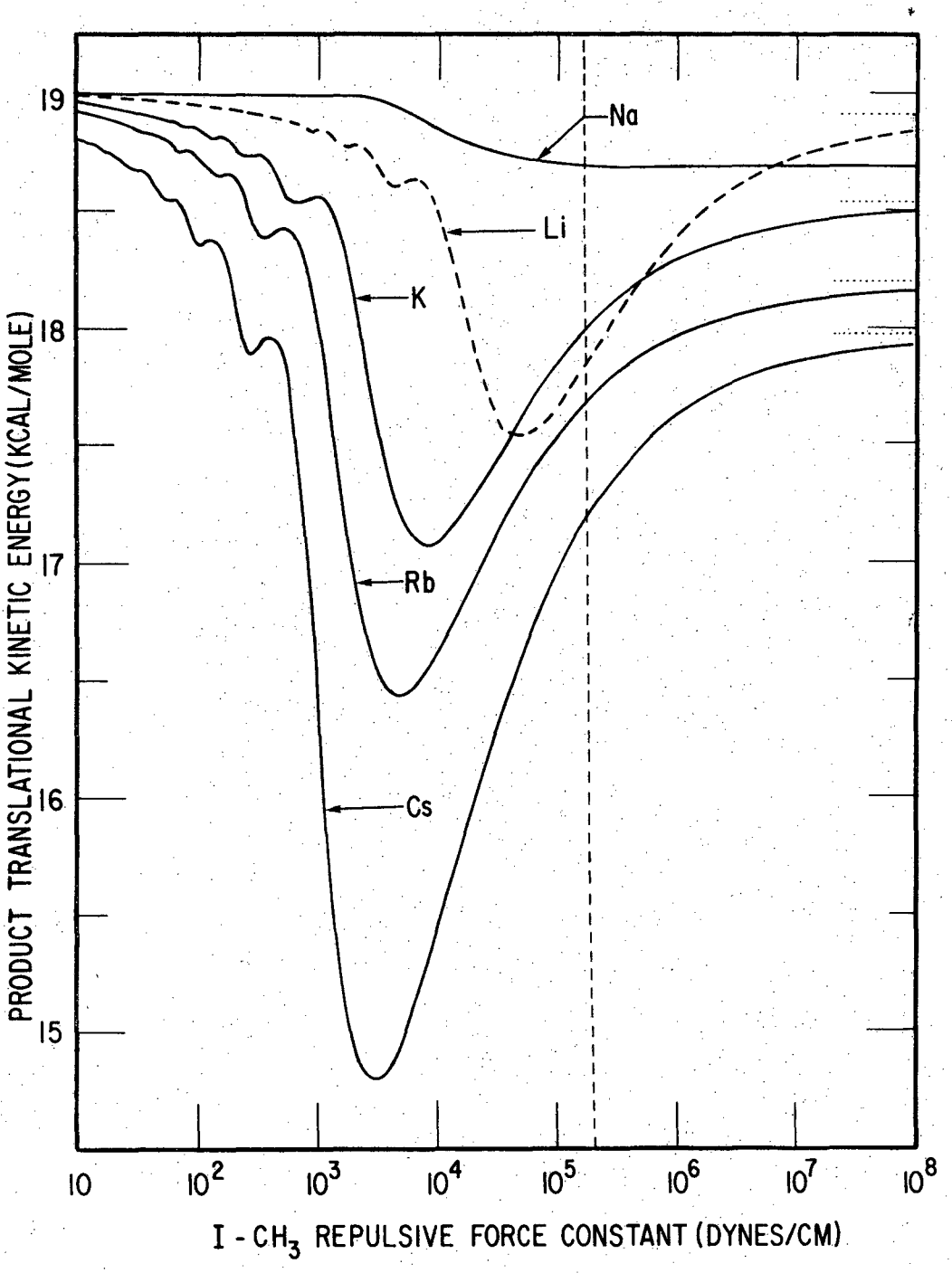

XBL 709-6673

Figure 4

justify a linear model. A more important realization is that these reactions are near the I-CH_2 impulsive limit where the energy partitioning should be independent of the actual intermediate configuration and detailed force laws, and should depend only on the I-CH_2 impulsive energy released. In Ref. 3, the effect of an initial reactant translational kinetic energy was studied and found to be relatively small. The effect of reactant kinetic energy on the present calculations is also readily estimated at the I-CH_2 impulsive limit; an initial relative velocity characteristic of the thermal energy in the experiments causes a decrease in the predicted CsI impulsive limit CM speed from ~5% for CH_3I to ~17% for C_4H_9I. Thus, incorporation of initial reactant kinetic energy into the calculations would probably allow better agreement with the experiments than is shown in Table I.

Ottinger's [3] calculations for these reactions, based on a similar, but somewhat more sophisticated, one-dimensional linear model, represented the alkyl radical as a chain of CH_2 particles with harmonic binding forces; in addition, a more complex potential function was used to represent the Cs-I-CH_2 interaction. These calculations were unable to match the experimental observations, almost certainly because of the potential energy function employed. For the potential surface of Fig. 1, Ottinger's p parameter[3] (ratio of initial I-CH_2 repulsion to Cs-I attraction) has a value of 2.68, which, by his criterion, represents considerably more repulsion than any case examined in Ref. 3. However, in contrast to the results of Ref. 3, the present calculations indicate that the fraction of the exothermicity appearing as product recoil increases monotonically with increasing repulsion P. This characteristic is due to the lack of

any "kink in the walls of our potential valley" shown in Fig. 1. Thus, the open exit channel of our surface allows the CsI speed to increase monotonically with the progress of the reaction rather than exhibiting the undulations apparent in Fig. 5 of Ref. 3. On our surface, the energy in repulsion is released over a short period of time, before the Cs atom or R group has moved appreciably; consequently, the I-CH_2 impulsive limit is approached. In contrast, the trajectories shown in Fig. 6 of Ref. 3 indicate that the "kink" in the potential surface employed there prevented a similar behavior and the CsI bond undergoes one half to one full oscillation before reaction is complete.

Another striking difference is the absence of any appreciable alkyl group excitation reported for the calculations of Ref. 3 in contrast to the appreciable alkyl group excitation predicted here. Although the representation of the alkyl group as a diatomic that is employed here is a rather crude model, the exitation appearing in it should, nevertheless, be indicative of the internal excitation (both rotation and vibration) of the radical in the actual reaction because the reaction is so near the I-CH_2 impulsive limit where conservation laws dictate that the internal excitation in the products can depend only on the impulsive I-CH_2 energy released. Actually, these reactions do deviate somewhat from this impulsive limit and the diatomic representation of the alkyl group employed here should underestimate somewhat the excitation transferred into this radical for a given I-CH_2 energy release; this effect should be more important for the larger radicals.

Raff's[6] three dimensional trajectory calculations for K + ICH_2CH_3 treated as a four particle reaction system employed a potential energy function chosen to match the early erroneous experimental reports of slow separation of highly excited products.[12] Since most of the energy was released as the reactants approached, Raff observed that the direct interaction trajectories produced large K-I excitation and little energy in either product recoil or internal excitation of the ethyl radical; a similar behavior is observed in the present model as both P and k_2 are decreased. Raff did however also observe a second mode of reaction, via formation of a long-lived complex, in which the ethyl radical was considerably excited; the present calculation fails to reproduce this second reaction mode for any values of P and k_2 considered, undoubtedly due to the lack of any attractive interaction in the r_2 coordinate.

2. M + I-CH_3 Reaction Series

Treatment of these reactions by a three particle, linear model with no initial energy of approach and with very simplified forces is very crude, but should yield reasonable results due to the fortuitous impulsive nature of the reaction dynamics. The three particle treatment is partially justified because it is likely that the CH_3 group behaves as a single particle due to the light mass of the hydrogen atoms. In particular it is expected that the CH_3 group will adiabatically relax to a planar, essentially non-vibrating configuration as the I atom departs at a relatively slow velocity. If the I atom were removed very rapidly with respect to the vibrational speed of the H atoms, the CH_3 radical would be expected to be left in a highly excited vibrational state due to the initial pyramidal distortion from its planar, equilibrium configuration. Because the cross section of

these reactions is relatively small,[1] the product is scattered predominately into the backward hemisphere,[1] and only the iodine end of the methyl iodide molecule is reactive,[13,14] it is very likely that the reaction does indeed occur for only approximately linear configurations with the iodine atom in the center. In the impulsive limit the effect of including a characteristic initial reactant energy is a small decrease of $\vec{M}_{IMP}$: 5.2% for CsI to 2.4% for LiI. Thus, incorporation of the initial product translational kinetic energy into the model would not affect the qualitative conclusions reached here.

The previous three-dimensional, exact trajectory claculations that were mentioned before[5] reach qualitatively different conclusions than are found here due to the choice of potential energy surface. For all these reactions 80 to 90% of the total energy was channeled into internal excitation of the products,[15] while here, 4 to 40% is the range of values. The wide range of values found here is due primarily to the difference of ΔD_0 among the reactions and secondly to the different fractions of P channeled into internal excitation. It is interesting to note that the reaction mechanisms on the potential surface which best fit the observed backward scattering were of the very direct type[15] that is found for this model. However, the average value of the angle defined by the three particles in the reactive collisions was only 108°;[15] the primary reason that such a small angle was observed is the sine probability weighting of the configuration angle. It should be again emphasized though, that the energy partitioning between translational energy and internal excitation at the impulsive limit is independent of the angular configuration.

In closing it is appropriate to speculate on the possible implications of the models presented here. By virtue of the light mass of Li and the relatively large force constant of LiI, the reaction of Li + I-CH_3 is expected to deviate from the impulsive limit to the greatest extent. Figure 4 (which emphasizes the deviations since it shows energy rather than momentum or velocity) does indeed show significant deviations. Careful studies of the velocity distribution of the scattered LiI product are planned at this laboratory to determine if the product translational energy is indeed less than that found for KI. If the trend of constant product CM momentum is strictly followed the LiI translational energy will be higher than that of KI. The angular distribution measured for the reactively scattered LiI in Chapter III shows a significantly broader distribution than that measured for the heavier alkali metals. A possible explanation is that the Li does indeed interact in a more complex manner with the dissociating I-CH_3 than would be the case at the impulsive limit.

The model predictions for the Na + ICH_3 reaction also exhibit qualitatively different behavior. It is the least exoergic of all the alkali-methyl iodide reactions with ΔD_0 = 18.4±2 kcal/mole. Since approximately 19.0 kcal/mole must appear in I-CH_2 repulsion, this reaction may be very restricted in the sense that the Na-I distance may be required to decrease all the way to its equilibrium value before reaction can begin; in contrast, the other M+ICH_3 reactions may be initiated at considerably larger M-I distances, consistent with the larger fraction of the exoergicity released as M-I attraction. Thus, within the framework of this model, one might expect a smaller reactive cross section for Na+ICH_3 and indeed, experimentally, the Na+ICH_3 reactive cross section is reported[1] to be

considerably smaller than that of Li or $K+ICH_3$. It is even possible that such a restricted approach would involve a significant activation energy for this reaction; no indication of an activation energy has yet been found for any of the reactions of the alkali metals with the diatomic halogens or alkyl iodides. An investigation attempting to measure the dependence of the reactive scattering of this reaction upon the initial translational kinetic energy will also be attempted. A further characteristic of this reaction may also be predicted. As shown in Fig. 4 the product translational kinetic energy is very close to the impulsive limit regardless of the assumed value of k_2; since the initial kinetic energy has such a small effect, the measured product recoil velocity should be simply the single impulsive velocity imposed upon the distribution in center of mass velocities in the crossed beams. An attempt will also be made to measure this velocity distribution. Deviations of the distribution from that predicted here should be very indicative of finer details of the potential energy surface.

Finally, the significance of the two derived model parameters should be discussed. The results can only be consistent with very close to 19.0 kcal/mole released as repulsion between the I atom and the CH_3 group. This assertion can now be made with the confidence of hindsight; by considering such data as bond dissociation energies, vertical electron affinities and probable shapes of potential energy curves, an estimate of the repulsive energy release was obtained by other workers and it was also 19 kcal/mole.[16] It should be emphasized that these two identical results were reached separately by independent studies. Secondly a value of $k_2 = 2\times10^5$ dynes/cm was found to best fit the available data

for the CsI product velocities. Not as much credence can be attached to the absolute value of this parameter, however, as there is no reason to believe that the potential surface is adequately represented by the parabolic surface appropriate to this model. However, it is believed that the repulsive force over the region on the true potential energy surface where the majority of P is released must be comparable with the force found in this model. These two parameters should certainly serve as valuable input information in the choice of a potential energy surface for future exact trajectory calculations.

REFERENCES

1. (a) G. H. Kwei, J. A. Norris, and D. R. Herschbach, J. Chem. Phys. 52, 1317 (1970); (b) G. H. Kwei, Ph.D. Thesis, University of California, Berkeley, 1967. (c) J. H. Birely, E. A. Entemann, R. R. Herm and K. R. Wilson, J. Chem. Phys. 51, 5461 (1969); (d) D. D. Parrish and R. R. Herm, to be published.
2. Ch. Ottinger, P. Strudler, and D. R. Herschbach, J. Chem. Phys., to be published.
3. Ch. Ottinger, J. Chem. Phys. 51, 1170 (1969).
4. This qualitative result was communicated by D. R. Herschbach.
5. For a review see M. Karplus, in Linus Pauling Festschrift (W. H. Freeman and Co., San Francisco, 1967).
6. L. M. Raff, J. Chem. Phys. 44, 1202 (1966); J. Chem. Phys. 50, 2276 (1969).
7. These results have been recently published: D. D. Parrish and R. R. Herm, J. Chem. Phys. 53, 2431 (1970).
8. Calculated from ω_e given in J. R. Rusk and W. Gordy, Phys. Rev. 127, 817 (1962).
9. Data taken from: for CsI, L. Brewer and E. Brackett, Chem. Rev. 61, 425 (1961); for CH_3I, G. Herzberg, Molecular Spectra and Molecular Structure (D. Van Nostrand Co., Inc. Princeton, N. J., 1966), Vol. 3.
10. H. J. M. Bowen, ed., Chem. Soc. (London), Spec. Publ. 11, M134 (1958).
11. This qualitative explanation was realized in Ref. 3 as well.
12. See Ref. 1(a). This paper traces the evolution of the analysis of the experimental data from relatively low E' value to substantial product translational energy.

13. P. R. Brooks and E. M. Jones, J. Chem. Phys. 45, 3449 (1966).

14. R. J. Buehler, R. B. Bernstein, and K. H. Kramer, J. Am. Chem. Soc. Soc. 88, 5331 (1966).

15. L. M. Raff and M. Karplus, J. Chem. Phys. 44, 1212 (1966).

16. D. R. Herschbach, private communication.

VI. APPARATUS FOR STUDY OF THE VELOCITY DEPENDENCE OF ELECTRONIC ENERGY TRANSFER IN ATOMIC COLLISIONS

A. Introduction

Processes of the type,

$$A^* + B \rightarrow A + B^* \quad (1)$$

$$A^* + B \rightarrow A^{*'} + B \quad (2)$$

$$A^* + BX \rightarrow AX + B^* \quad (3)$$

$$A^* + BX \rightarrow AX^* + B \quad (4)$$

$$A^* + B \rightarrow A + B^+ + e^- \quad (5)$$

$$A^* + B \rightarrow AB^+ + e^- \quad (6)$$

$$A^* + BX \rightarrow AB^+ + X^- \quad (7)$$

$$A^* + BX \rightarrow A + B^+ + X^- \quad (8)$$

present very attractive systems to study by the technique of crossed molecular beams. A^* is an atom in a metastable, excited electronic state with a lifetime long with respect to the time required to travel from the excitation region to the collision zone (approximately 10^{-3} sec). B^*, $A^{*'}$, and AX^* are species in electronically excited states with allowed radiative transitions with lifetimes short enough ($\lesssim 10^{-6}$ sec) that the excited species cannot move appreciably on a macroscopic scale in the time between collisional formation and emission of a photon. Providing that the wavelength of the emitted photon is in the proper range ($\sim$ 1500 Å to 8000 Å), positioning a photomultiplier with a narrow bandwidth, interference filter directly below the collision zone provides a specific detector for the excited product. For processes (5) - (8), where ions are the products of the collision, an electron multiplier in place of the photomultiplier would provide an extremely

sensitive detector with very little interfering background. An obvious extension would be to provide for optical excitation of atom A in the collision zone; with this excitation mode the lifetime restriction that was placed on A^* could be relaxed and a much wider choice of incident excited species would be available.

This chapter describes an apparatus that has been constructed to investigate the velocity dependence of the total cross sections of the processes (1) through (4). An investigation of a system that is a particular example of (1), $Hg^* + Tl \rightarrow Hg + Tl^*$, has been completed and will be discussed in the following chapter; the apparatus will be described here as it was constructed and operated for this particular system. The vacuum system as well as much of the auxillary equipment described in Chapter II was used in the assembly of this apparatus; for discussion of these parts see that chapter. The mechanical drawings, together with UCRL numbers, of the apparatus components constructed for this study are included in Appendix A, and the electrical drawings are given in Appendix B. Figure 1 shows a schematic of the essential parts of the apparatus that are contained in the vacuum chamber.

B. Beam Sources

1. Ovens

The two incident beams are each formed by molecular effusion from a double chamber oven very similar in design to the double chamber oven used for the Li atom source in Chapter II. One important difference is that each of these two ovens is constructed as one unit; the two chambers are connected by a thin walled tube with all welded construction. The charges are placed in the lower chambers by means of thimbles inserted from the bottom of the chamber and held in place by a yoke and screw

assembly. The thimbles are sealed with copper gaskets. In the case of the Hg oven, this seal has been found to give leak free performance, but Tl attacks copper at high temperature, necessitating the replacement of the copper gasket in the Tl oven after each experiment.

As indicated in Fig. 1, the Tl oven is constructed with the upper chamber beside, rather than above, the lower chambers. This design was deemed necessary in order to allow the oven to fit conveniently behind the velocity selector; however, it has been the cause of bothersome difficulties. When the source slit is aligned with the velocity selector, the oven is, of course, at room temperature; during operation, the Tl oven is at a high temperature and the accompaning thermal expansion results in a misalignment of the Tl oven with respect to the velocity selector. In order to correct for this, the amount of expansion is approximately calculated and the oven is aligned accordingly. Since the alignment strongly affects the velocity transmitted by the selector, calibration of the alignment is necessary; this calibration will be discussed later. If the upper oven were above the lower oven, expansion would take place along the length of the slit; alignment is much less critical in this dimension and thus no problem would arise. Perhaps the best configuration would place the upper oven in front of the lower so that expansion would take place along the beam path.

As with the Li upper oven, the Hg upper chamber has the connection tube extended above the level of the source slit to insure thermal equilibrium of the effusing gas. In the Tl oven, a rod screws into the upper chamber so that it blocks the direct path from the connecting tube to the source slit; this serves the same purpose as the tube extension in the Hg oven. This rod is also sealed by a copper gasket; such high temperatures

Figure 1.

Diagram of the apparatus as viewed from above. The beams effuse from double chamber ovens and cross at 90° at the scattering center. The entire surface ionization detector assembly (ionizing filament, ion optics, analyzing magnet, electron multiplier, and electrical shield) may be scanned in the horizontal direction in order to center the filament in the Tl beam profile.

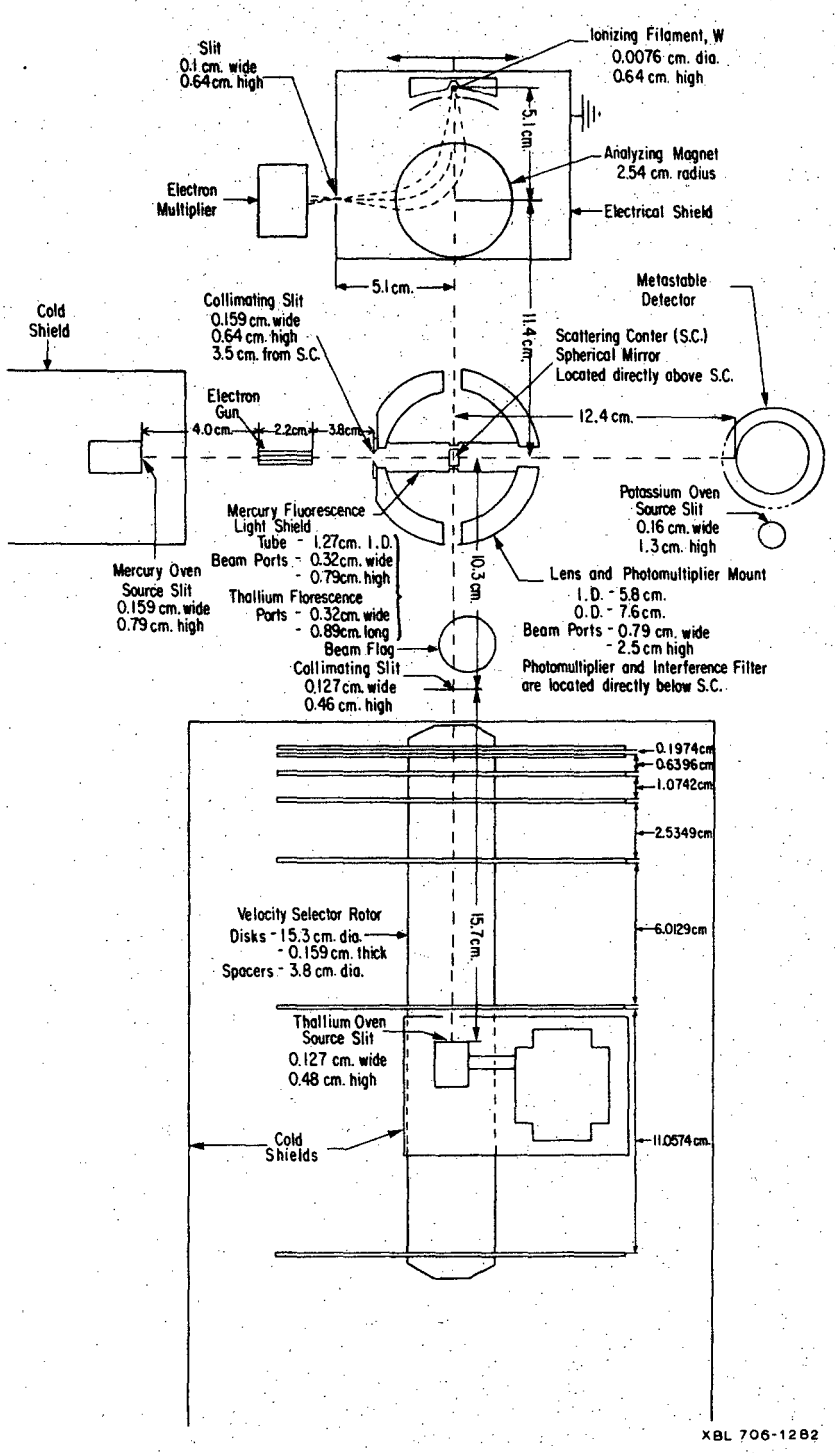
Slit
0.1 cm. wide
0.64 cm. high
Ionizing Filament, W
0.0076 cm. dia.
0.64 cm. high
5.1 cm.
Analyzing Magnet
2.54 cm. radius
Electron
Multiplier
Electrical Shield
5.1 cm.
Metastable
Detector
Cold
Shield
Collimating Slit
0.159 cm. wide
0.64 cm. high
3.5 cm. from S.C.
11.4 cm.
Scattering Conter (S.C.)
Spherical Mirror
Located directly above S.C.
Electron
Gun
4.0 cm.
2.2 cm.
3.8 cm.
12.4 cm.
Potassium Oven
Source Slit
0.16 cm. wide
1.3 cm. high
Mercury Fluorescence
Light Shield
Tube - 1.27 cm. I.D.
Beam Ports - 0.32 cm. wide
- 0.79 cm. high
Thallium Florescence
Ports - 0.32 cm. wide
- 0.89 cm. long
10.3 cm.
Mercury Oven
Source Slit
0.159 cm. wide
0.79 cm. high
Lens and Photomultiplier Mount
I.D. - 5.8 cm.
O.D. - 7.6 cm.
Beam Ports - 0.79 cm. wide
- 2.5 cm high
Photomultiplier and Interference Filter
are located directly below S.C.
Beam Flag
Collimating Slit
0.127 cm. wide
0.46 cm. high
0.1974 cm
0.6396 cm
1.0742 cm
2.5349 cm
Velocity Selector Rotor
Disks - 15.3 cm. dia.
- 0.159 cm. thick
Spacers - 3.8 cm. dia.
15.7 cm.
6.0129 cm
Thallium Oven
Source Slit
0.127 cm. wide
0.48 cm. high
Cold
Shields
11.0574 cm.
XBL 706-1282

Figure 1

have been achieved in this chamber that the copper gasket has melted, yielding a permanent, leakfree seal.

The Hg oven is supported by a thin-walled, stainless steel tube welded to the top of the upper chamber. The Tl oven is supported by a tube which is attached by screws to the lower oven. Provision has been made to allow this oven to be removed and then replaced in the same position. This is accomplished by holding the upper end of the oven support tube in a clamp that has a ridge around the inside; the end of the tube is inserted so that it is directly against the ridge, and thus the vertical height of the oven is defined. The sides of the clamp ensure that the tube is vertical. The other degree of freedom, rotation about the axis of the tube, is reproduced by a pin in the tube and one in the clamp; the oven is properly positioned when the oven and tube are rotated to where these two pins meet.

Heating of each chamber is accomplished with .020" tantalum wire strung with ceramic beads and energized with a variable voltage, a.c. powerstat. No heat shielding is required for the Hg oven since only low temperatures are required (generally 398 and 490°K in the lower and upper chambers, respectively), but extensive shielding is required by the Tl oven in order to achieve the high operating temperatures that are required (typically 1098 and 1173°K in the upper and lower chambers, respectively). The system that has been found to work best is to first wind heating filaments through the holes in the oven, attach several layers of heat shielding (.001" stainless steel foil), then add a second layer of heating coils around the outside of this heat shielding and finally adding more layers of shielding. This is done to the lower and upper chambers. Additional coils are required around the tube connecting the two ovens and the oven support tube

in order to prevent cold spots in the ovens. The temperature of each of the four chambers of these ovens is monitored by a chromel-alumel thermocouple.

2. Shields, Collimating Slits, and Beam Flag

The Hg oven is mounted on the liquid nitrogen trap attached to the rotating lid (see Chap. II for a discussion of these apparatus features); the rotating lid is held stationary throughout this experiment. Surrounding this oven is a nickel plated cold shield constructed from .0625" copper plate; the nickel plate is necessary to prevent amalgamation of the copper. This shield is attached to the liquid nitrogen trap, and is cooled by conduction to it. The bottom of the shield is constructed in the form of a leak-tight tray in order to collect Hg condensed inside the shield and thereby reduce contamination of the apparatus. Mercury contamination has not been a great problem. Upon opening after completion of an experiment, the apparatus is allowed to ventilate for a period of time and then all condensed Hg is cleaned up. Periodic checks for dangerous Hg vapor levels are made and except for immediately after opening, the chamber has been below prescribed tolerance levels.

The Tl oven, its surrounding cold shield, and a further cold shield surrounding the whole velocity selector assembly are mounted on an additional liquid nitrogen trap located directly above the selector. The oven shield is constructed of .125" copper while the outer shield is also copper but of only .0625" thickness; both these shields are cooled adequately by conduction to the LN_2 trap. The outer shield is effectively a cryogenically, differentially pumped chamber.

Both the Tl and Hg ovens are equipped with standard knife-edge, adjustable width source slits. Each beam is collimated with an adjustable width slit; the Tl slit is mounted on the velocity selector housing while the Hg slit is attached to the lens and photomultiplier mount. Only the Tl beam is equipped with a beam flag; it is simply an aluminum cylinder that may be moved into the beam path manually with the same arrangement used for the gas beam flag in the Li atom study.

C. Electron Gun

In order to excite the incident atom A to its metastable state, A^*, (in the experiment discussed later, A^* = Hg $6^3 P_{0,2}$) an electron gun is installed between the beam source and the scattering center. Electron impact readily produces electronic excitation of atoms,[1] and, in particular, theoretical[2] and experimental[3,4] studies have shown that the total cross section for the excitation of the low lying metastable states of Hg by low-energy electrons (5.5 to 10.0 eV) is fairly large (~3 $\mathring{A}^3$ for $^3P_2$ at 6 eV).[2]

Placement of the electron gun between the source slit and collimating slit does not significantly affect the collimation of the Hg beam. An upper limit for the deflection of a Hg atom in the plane of the beam may be set by considering a 10 eV electron undergoing an elastic collision with the atom and being scattered in a direction perpendicular to both the atom and the electron beams; a deflection of 2.5° would result. To excite the atom an inelastic collision must take place, and thus the deflection of the metastable atom would be significantly less than this value.

1. Design and Construction

It was desired to construct an electron gun with three characteristics: high current density, reasonably narrow electron energy distribution, and tractable mathematical description. A schematic of the electron beam design selected is shown in Fig. 2. The electrons are thermally emitted from the cathode and accelerated by the accelerating grid; when the cathode is operating such that the magnitude of the current emitted is space charge limited, the accelerating grid allows variable control of the magnitude of the current. The electron beam is decelerated by a second grid and enters the region bounded by the two plates and the two grids where it interacts with the atomic beam. Upon leaving this region through the second grid, the beam is collected by the collector. Throughout the length of the electron path, divergence of the beam is prevented by an intense magnetic field parallel to the direction of the electron flow. Brillouin[5] has shown that a sufficiently strong magnetic field will prevent the beam from diverging under the effect of space charge; the electrons spiral around the "lines of force" rather than acquiring a perpendicular velocity component. Haeff[6] has presented a complete mathematical treatment for an electron beam flowing between two infinite parallel plates; the design of this gun approximates this situation. Table I gives the physical characteristics of the electron gun. The width of the electron beam is defined by the length of the accelerating grid while the thickness is determined by the width of the opening between the plates; thus, the electron beam completely fills the space between the plates.[7]

Figure 2.

Schematic of the electron gun. The electron beam is emitted from the cathode, passes through the accelerating grid, and enters the region between the two plates where it interacts with the atomic beam. Finally, it is collected at the collector after leaving the plates through the grid at the top. A magnetic field, indicated by H, is parallel to the electron flow and confines the beam.

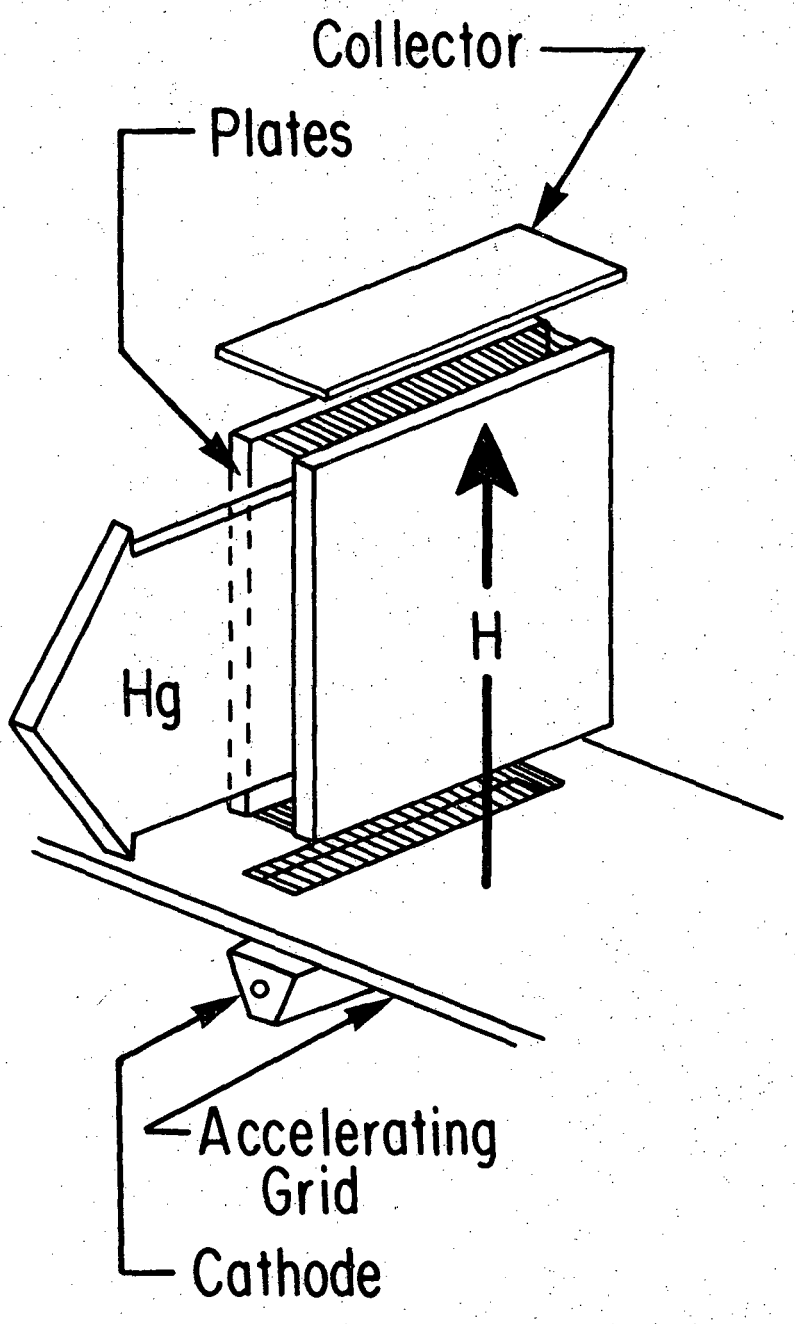

XBL 706-1277

Figure 2

TABLE I. Summary of Characteristics of Electron Gun

Cathode Emitting Surface	
Width	0.406 cm
Length	2.38 cm
Distance from Accelerating Grid	0.9 cm
Typical Operating Voltage	0.0 volts
Accelerating Grid	
Width	0.48 cm
Length	1.27 cm
Distance from Plates	0.159 cm
Grid Plate Width	1.905 cm
Typical Operating Voltage	50 to 80 volts
Plates	
Distance Between Plates	0.238 cm
Thickness of Each	0.159 cm
Height	1.905 cm
Length	2.222 cm
Distance from Collector	0.159 cm
Collector	
Length	1.905 cm
Width	0.318 cm
Thickness	0.0025 cm
Electron Beam (between Plates)	
Width	1.27 cm
Thickness	0.238 cm

TABLE I (continued)

Atomic Beam	
Height	0.79 cm
Thickness	0.159 cm
Magnet	
Pole Face Width	2.54 cm
Pole Face Length	2.54 cm
Pole Gap	3.61 cm
Calculated Field Intensity	1100 gauss

The accelerating grid is constructed of nickel metal with tungsten wires serving as a grid; in order to minimize the diverging effect of the grid, only cross wires are included in this grid and the grids on the plates. The plates are fabricated from stainless steel and spot welded together with 0.318 × 0.318 cm spaces between the plates at each of the four corners. This assembly has been nickel plated. The collector is simply a strip of platinum foil. A copper frame screwed to the lower magnet pole piece serves as the mount for the above three pieces. Ceramic rods inserted through holes in the grid plate supports and in the plates (through the spacers) and fastened with set screws provide electrical insulation and support. The ends of the platinum foil collector are simply wrapped around similar ceramic rods; electrical contact is made by a 0.0076 cm tungsten wire spot welded to the foil. Nickel wire (0.05 cm dia), in spring contact with the element provides electrical connections for the plate assembly and accelerating grid.

The cathode is of the indirectly heated type, similar to those described by Rosebury;[8] it is machined from porous tungsten and impregnated with barium calcium aluminates. This cathode was purchased from Philips Metalonics (Mount Vernon, New York) supplied with Type A impregnant. Although this impregnant is the most resistant to poisoning, the lifetime of the cathode was severely limited by contamination from pump oil, mercury, oxygen and water from the air, and various substances driven from surrounding materials upon heating by radiation from the cathode. Efforts were made to minimize this, but they were not completely effective. Probably the only satisfactory solution is to enclose the electron gun in a chamber that may be kept evacuated and separate from

the rest of the apparatus except during an experiment. The cathode is mounted by spot welding to tantalum supports which also provide electrical contact.

The magnet yoke is fabricated from soft iron and nickel plated to prevent corrosion. The energizing coils are similar to the magnet coils used in the magnetic deflection analysis experiments; 0.476 cm ØD copper tubing carries both cooling water and the energizing current. A magnetic field with calculated intensity of 1100 gauss is created by 100 amp energizing current.

2. Operation

During the production of an electron beam the cathode is held at ground potential while the collector and plate are held at the same voltage (the nominal energy of the electron beam.) The accelerating grid is held at the potential which is required to give the desired beam current; this is typically 50 to 80 volts. During operation, the beam is modulated in order to allow signal detection by frequency sensitive techniques. This modulation is accomplished by applying a square wave to the cathode; the negative half cycle is at ground potential while the positive half is at a potential larger than the plate voltage, typically 40 V. The magnetic field intensity is of sufficient strength that the rate of increase of beam current (as measured at the collector) with increasing field intensity has dropped almost to zero at typical beam currents.

Figure 3 shows the measured Hg metastable atom flux as a function of electron energy; the Hg beam was bombarded by a 0.30 milliamp beam (current density = 0.88 ma/cm^2). This is the electron current that is

Figure 3.

Excitation functions of mercury. The solid curves are the experimental curves measured for this electron gun with a current of 0.30 milliamps. The abscissa is the voltage of the electron gun plate with respect to the cathode; it was calibrated by requiring the peak in the potassium surface curve to coincide with the peak in the curve calculated from Borst's experimental data. The two broken curves were derived by integrating the data from the two indicated references over the calculated space charge potential in the electron gun. The mathematical treatment to derive the space charge potential is from Ref. 6.

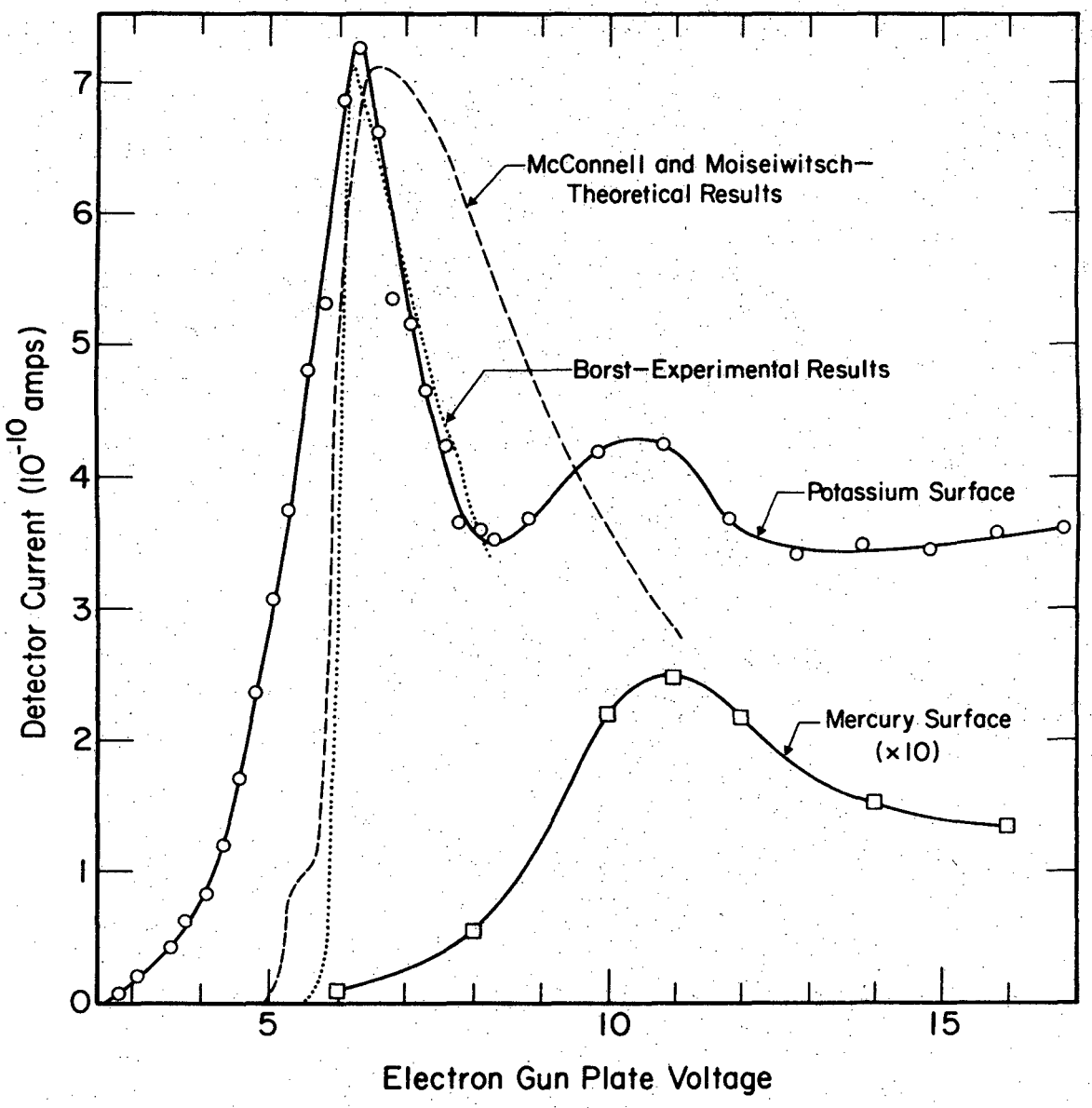

XBL 709-6555

Figure 3

used during all experiments. As discussed further in Section E, the metastable atoms are detected by collecting the electrons ejected from a metal surface by the impinging excited atoms. The potassium surface, with a work function of 2.24 V,[9] detects both the lower ($^3P_0$ and $^3P_2$) and upper ($^3D_3$)[3a] metastable states; the potassium surface curve shows a peak near 6V corresponding to the lower states and a peak at higher voltages, probably due to not only the $^3D_3$ metastable state, but also to high Rydberg states that would have lifetimes comparable to the time of flight from the excitation region to the detector. If no potassium is deposited on the detector and if the mercury beam is allowed to hit the surface for a period of time, a signal is observed with qualitatively the same features at high electron voltages, but the lower energy peak is no longer observable. These features are expected from the 4.53 V[9] work function of Hg.

The electron energy has been approximately calibrated by subtracting 4 volts from the nominal voltage applied to the electron gun plate. This value was chosen to allow the peak in the potassium surface curve to coincide with the peak in the curve calculated from the excitation function measured by Borst.[4] This is the dotted curve shown in Fig. 3; it was derived by numerically integrating the curve from Borst's paper over the space-charge voltage distribution in the electron gun. The mathematical treatment used was that of Haeff[6] using the infinite parallel plate approximation. Borst's data is for the $^3P_2$ state only and does not include the $^3P_0$ state, but since the excitation cross-section for $^3P_0$ is much smaller[10] and peaks at lower voltages[2] than the excitation function of $^3P_2$, this should not significantly affect the peak position. For comparison, a similar curve calculated from the most recent theoretical results[2] is

included; as is obvious near the threshold voltage, the $^3P_0$ state is included with correction made for different detection efficiencies. Both of these calculated curves are arbitrarily normalized at the peak heights.

The four volt difference between the nominal electron plate voltage and that derived from the approximate calibration is ascribed to 1) the contact potential between the very low work function cathode and the relatively high work function nickel surface of the plates, 2) possible surface charge on the plates, and 3) thermal energy of the electrons when they leave the cathode. The present experimental curve extends to lower voltages than the curve derived from Borst's data; this is ascribed to several factors: contributions from the $^3P_0$ state, presence of higher energy electrons at the edges of the plates where the space charge potential is less and the infinite plate approximation breaks down, local differences in the surface charge on the plates, and presence of higher energy electrons due to the modulation of the electron beam (when the beam is turned off or on, the full space charge potential does not change instantaneously).

The signal detected on the mercury surface has a tail that extends down to the peak that is ascribed to the lower metastable states. This is probably due to a residual detection of these lower states on the mercury surface since the work function of mercury is low enough to allow a small detection efficiency. However, since it is desired to investigate processes involving the lower states, one must be careful to determine that any measured signal ascribed to these lower states does, in fact, decrease proportionately to the metastable signal as measured on the potassium surface as the electron energy is increased above the peak voltage. As

described in Section F , the effect of the higher energy electrons due to the beam modulation is eliminated in the experiments by the signal detection technique employed there.

For the same electron current, the position of the excitation function on the abscissa changes slightly from experiment to experiment. This is thought to be due to changes in the work function of the cathode surface and to changes in the plate surface charge. Consequently, the calibration is checked before each experiment in order to set the nominal voltage to the optimum value.

D. Velocity Selector

1. Introduction

In order to measure the velocity dependence of the processes mentioned above, it must be possible to systematically vary the relative velocity of the incident species. The relative velocity, V, is given by

$$V = (V_1^2 + V_2^2)^{1/2}$$

where V_1 and V_2 are the velocities of the incident collision partners. Therefore, if one velocity is considerably greater than the other, by velocity selecting only the faster beam reasonably good control of the relative velocity may be achieved even when the slower beam retains a full Maxwellian distribution. In our prototype system of Hg^* + Tl the Tl beam is selected; the ratio of the velocity of the Tl to that of the Hg is only 1.5 and the resolution of the relative velocity is therefore poor. However, as discussed in the introduction to the next chapter, this system has been widely studied and shown to have large cross sections for energy transfer; consequently this system was chosen for the initial investigation. In other systems of interest the mass of the colliding partner is

generally considerably smaller than the mass of Hg, and thus the velocity resolution in future experiments should be considerably improved.

The mechanical selection and transmission of the molecules of a molecular beam within a given velocity range may be accomplished by passing the beam through two apertures which are successively opened for a short period of time. In order to prevent transmission of harmonics (secondary, slower velocities) the time between two selection periods must be long compared to the flight time of the slowest molecules; consequently the transmission of such a system is low.

An alternative that avoids this problem is a selector that not only transmits the design velocity but also eliminates high and low velocities from the beam; when this is accomplished the repetition rate can be greatly increased. One design that achieves this and has been used for velocity selection of neutrons as well as molecules consists of a rotating cylinder with helical grooves milled lengthwise along the circumference.[11,12] Molecules having rejected velocities are removed from the beam by collisions with the sides of the groove, and the repetition rate is limited (up to certain other design considerations) only by the rotational frequency achievable and the number of grooves that can be machined. However these groove are difficult to machine and the solid cylinder construction yields a high moment of inertia with its accompanying requirement of a large motor and bearings for the achievement of high rotational speeds.

These two difficulties have been overcome by construction of rotors using a series of slotted disks to define the helical paths. By placing the disks properly all harmonics can be eliminated; the faces of the disk as well as the sides of the slots become important in the removal of mole-

cules with undesired velocities. In order to simplify machining most slotted disk velocity selectors (SDVS)[13,14] have been constructed using straight slots cut parallel to the axis of rotation to approximate helical paths. Recently Kinsey[15] has suggested that straight slits be cut tangential to the desired helix; this has the advantage of a larger transmission and requires fewer disks to eliminate all harmonics. In the same reference, a systematic method for calculating an efficient disk placement is presented Grosser[16] has constructed a SDVS that will transmit two velocity ranges: high velocities when rotated in one direction and low velocities when operated in the reverse direction. In addition to the extended velocity range, a decided advantage of this design is that the alignment of the selector with the beam (which directly affects the velocity transmitted) may be confirmed by comparing the velocity analysis of the beam taken in one rotational direction with that taken in the opposite direction. Another improvement has been effected by Kristensen, et al.[17]; they have used electric discharge machining to fabricate disks with slots of closer tolerence and more complex design. It has also been reported that E. A. Greene has successfully fabricated a SDVS using disks of very thin foil; the slots are created by photoetching. Cowley, et al.[17a] have successfully designed and operated a mechanical velocity selector based on a radically different design; two concentric cylindrical shells with slits cut axially from one end are rotated about their common axis at the same rotational speed. For molecules traveling perpendicular to the axis, the slits define a trajectory for a selected velocity and eliminate all side-bands. If the beam and selector are properly aligned, rotation in either direction yields identical transmission characteristics; this

feature allows easy alignment. The rotor is a compact unit that mounts directly on the end of the motor shaft, eliminating the requirements of high speed bearings for the rotor and coupling between two rotors.

2. Design

Decisions on the design features of a SDVS represent a complex trade off between several competing factors: velocity range, beam path length, transmission, velocity resolution, ease of fabrication and speed of rotation. The parameters of this selector follow those of Trujillo, et al.[14] to a large extent; it was necessary, however, to use thicker disks and wider slots. The proper positioning of the disks was calculated by a method that closely parallels the suggestion of Kinsey;[15] this will be discussed more fully later. The resulting rotor may be used in two modes; placing the oven between the last and next to last disk yields a low resolution, short path length selector, while the complete rotor gives a comparatively high resolution, but with a longer path length and lower transmission.

The parameters which characterize the geometry of the rotor are

$$\beta = d/L,$$

$$\gamma = \ell_1/r\phi$$

and the fractional open time,

$$\eta = \ell_1/(\ell_1 + \ell_2)$$

where d is the disk thickness, L is the length of the rotor, r is the disk radius, ℓ_1 is the slit width, ℓ_2 is the wall thickness between the disks, and ϕ is the angle through which the rotor turns while a molecule with the desired velocity, v_0, travels the length, L. The performance of the selector is given by

$$v_0 = \omega L/\phi,$$

$$R \cong \gamma - \beta$$

$$T = G\, v_0\, I(v_0),$$

and

$$\eta' = \eta\,(1 - \beta/\gamma)$$

where ω is the angular frequency, R is the half-width velocity spread, T is the transmission of the rotor, $I(v_0)$ is the original beam intensity at velocity v_0, $G = \eta\,\gamma(1-\beta/\gamma)^2$ and η' is the effective fractional open time. The above treatment of the principles of rotor design was first presented by Hostettler and Bernstein[13]. The geometry and parameters characterizing the rotor constructed for this study are given in Table II.

When the parameters have been set it is necessary to determine a placement of the disks so that all side bands are eliminated. In the early designs[13,14] trial and error methods were used to discover suitable positions. Kinsey[15] presented a systematic method for determining the most efficient placement of disks with true helical slits; he generalized this method to straight slots of constant width, cut parallel to the axis of rotation. A corrected version of this generalization is developed here for use in placing the disks in the present rotor.

The principle involved in the placement of the disks is that a single slotted disk is a velocity selector, albeit of poor resolution. The second disk is placed so as to pass the design velocity, v_0, and to eliminate the maximum and minimum velocities passed by the first disk (v_1^+ and v_1^- respectively). This placement is shown in Fig. 4. The second disk should be

TABLE II. Summary of Charateristics of Velocity Selector Rotor

	Low Resolution Mode	High Resolution Mode
Number of disks	6	7
Diameter of disks	15.24 cm	
Number of slits per disk	240	
Radial length of slits	0.635 cm	
Slit width, ℓ_1	0.084 cm	
Wall thickness between slits, ℓ_2		
at base of slits	0.099 cm	
at top of slits	0.116 cm	
average value	0.107 cm	
Average radius	7.302 cm	
Disk thickness, d	0.160 cm	
Over-all length of rotor, L+d	11.42 cm	22.63 cm
L	11126 cm	22.47 cm
ϕ	0.0786 rad	0.1568 rad
γ (average)	0.146	0.073
β	0.0142	0.0071
η (average)	0.44	
G	0.0524	0.0262
Velocity spread, R	0.132	0.066
η'(average)	0.38	
Conversion from rotor frequency ν (cps) to velocity v_0 (cm/sec)	$v_0 = 897 \times \nu$	

Figure 4

Rolled out representation of the rotor showing the placement of the first two disks.

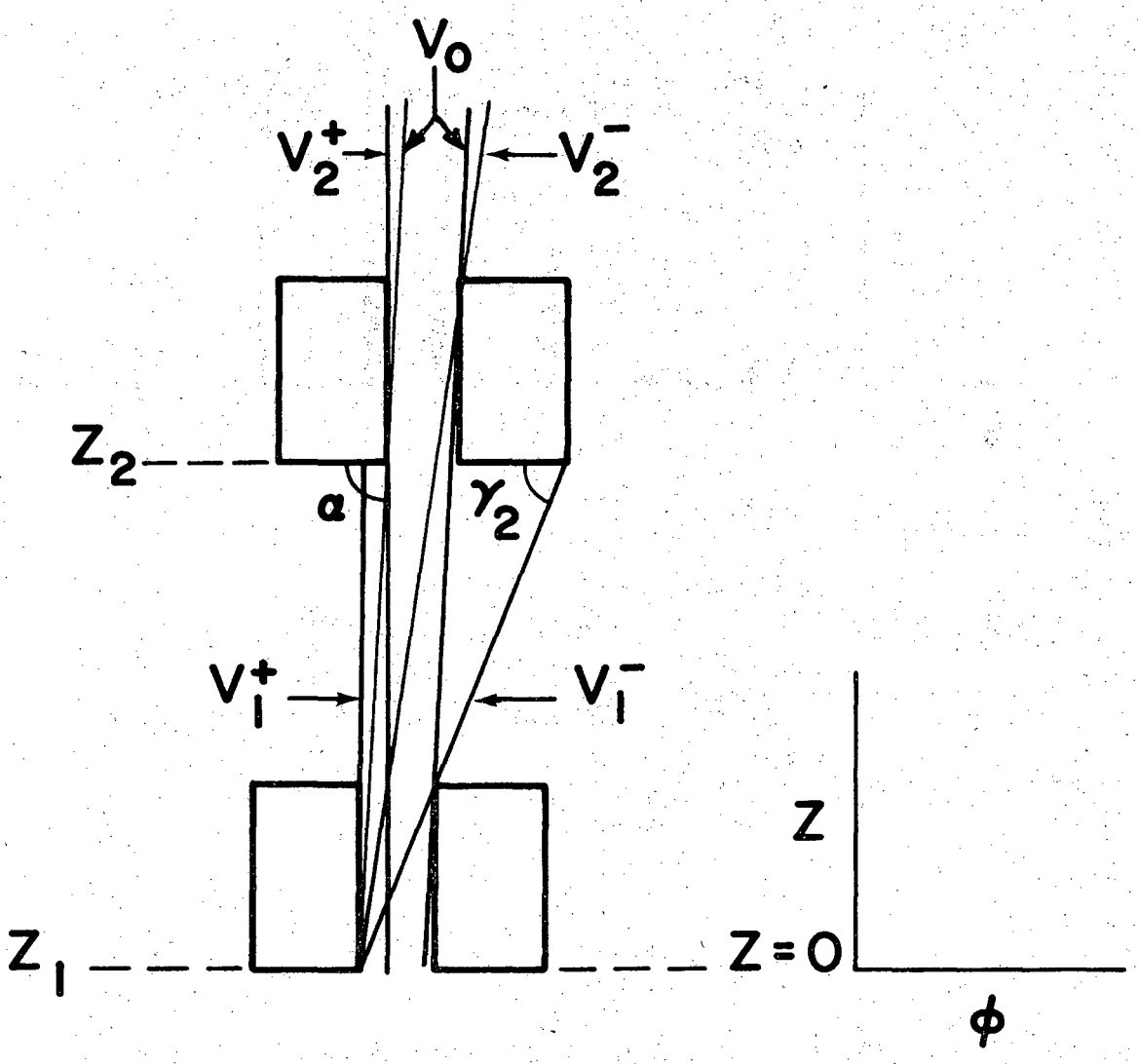

XBL 706-1280

Figure 4

placed as far as possible from the first, in order to obtain the best resolution without allowing any sidebands to pass. This process is repeated with succeeding disks until the desired resolution is obtained.

If the selector rotor is given in cylindrical coordinates, the coordinate system of Figs. 4 through 6 is obtained by "unrolling" the surface R = r where r is the radius of the disks to the bottom of the slits. The bottom of the slit is used because this is the most unfavorable part of the slit for the elimination of sidebands (the wall thickness between slits is wider at the top than at the bottom of the slits).

It can be seen from Fig. 4 that the placement of the second disk is determined by the conditions that v_1^- is eliminated, i.e.

$$Z_2 \cot \gamma_2 - Z_2 \cot \alpha \leq \ell_1 + \ell_2$$

(where α is the angle that the trajectory of v_0 makes with the ϕ axis) and that v_1^+ is eliminated, i.e.,

$$Z_2 \cot \alpha \gtrless \ell_2.$$

The seemingly best solution is to adjust α until both conditions could be satisfied for the equality; however, due to the small ϕ required for the transmission of high velocities, it is necessary to set α somewhat larger than this optimum value. In this case only the first equality need be satisfied and the second condition will be automatically met. Using

$$\cot \alpha = r\phi/L \quad \cot \gamma_2 = \ell_1/d,$$

one finds

$$Z_2 = d(\eta')^{-1}.$$

As seen from Fig. 5 an analogous condition holds for the elimination of v_2^- by the third disk, i.e.

$$Z_3 \cot \gamma_3 - Z_3 \cot \alpha = \ell_1 + \ell_2$$

where

$$\cot \gamma_3 = (\ell_1 + Z_2 \cot \alpha)/(Z_2 + d).$$

This yields the results

$$Z_3 = (Z_2 + d)\,(\eta')^{-1}$$

(Here it has been assumed that all disks have thicknesses equal to d; the generalization to disks of differing thicknesses is obvious). The above equation for Z_3 is valid only if v_2^+ is also eliminated. This is true only if

$$Z_2 \cot \alpha \leq \ell_1$$

and

$$(Z_3 - Z_2) \cot \alpha \leq \ell_2.$$

Physically, this means that some of the infinitely fast atoms pass the first two disks and that the "earliest" ones (those barely passing the second disk, thus composing v_2^+) are stopped by the third disk. This discussion for the third disk is applicable to the ith disk, yielding

$$Z_{i+1} = (Z_i + d)\,(\eta')^{-1}$$

if

$$Z_i \cot \alpha \leq \ell_1$$

and

$$Z_{i+1} \cot \alpha - Z_i \cot \alpha \leq \ell_2.$$

In the event that

$$Z_i \cot \alpha \leq \ell_1$$

but

$$(Z_{i+1} - Z_i) \cot \alpha > \ell_2$$

Figure 5

Rolled out representation of the rotor showing the placement of the third disk.

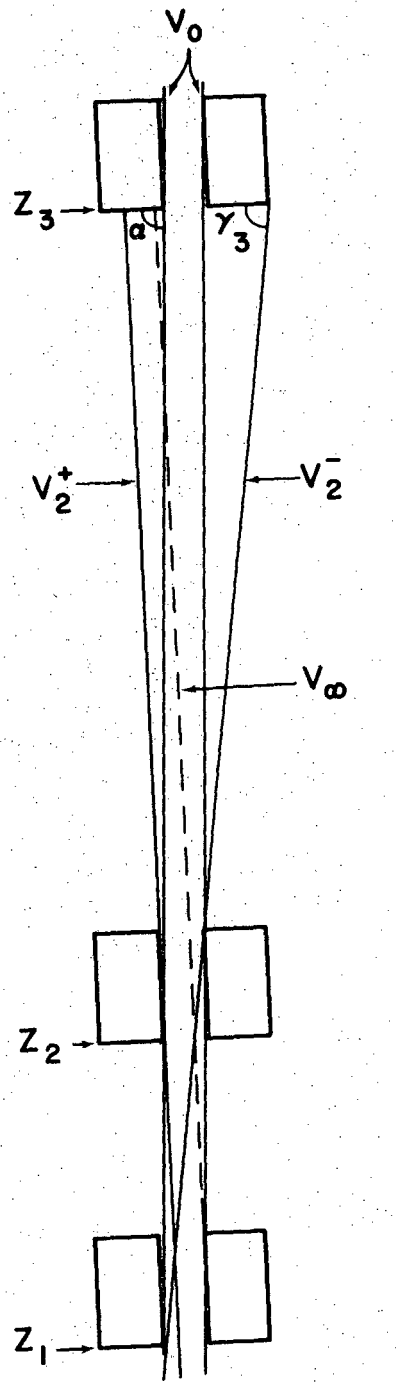

XBL 706-1279

Figure 5

Z_{i+1} must be recalculated using the condition

$$(Z_{i+1} - Z_i) \cot \alpha = \ell_2,$$

in order to eliminate v_i^+, giving

$$Z_{i+1} = Z_i + \frac{\ell_2 L}{r\phi}.$$

In the case that $Z_i \cot \alpha > \ell_1$ the condition for the elimination of v_i^- is the same as above:

$$Z_{i+1} = (Z_i + d)(\eta')^{-1}.$$

However, in order to eliminate v_i^+ the condition

$$Z_{i+1} \cot \alpha - \ell_1 - Z_{i+1} \cot \delta_{i+1} \leq \ell_2$$

must be met, as may be seen from Fig. 6. Substituting

$$\cot \delta_{i+1} = (Z_i \cot \alpha - \ell_1)/(Z_i - d)$$

yields

$$Z_{i+1} \leq (Z_i - d)(\eta')^{-1} \qquad (1)$$

Of course the smaller result must be used to prevent sidebands.

Kinsey obtains the result

$$Z_{i+1} = (Z_i + d)\,\eta^{-1}$$

for the placement of the third and all succeeding disks when helical slots are used. He then makes the evidently erroneous statement that for straight slots one merely substitutes η' for η in the above equation. This positioning would eliminate v_i^- but would allow transmission of high velocity sidebands. Figure 1 in Kinsey's article[5] suggests that in his analysis he was assuming a v_0 such that he could position his i + 1 disk at the most favorable distance, i.e. the greatest distance that would allow

Figure 6

Rolled out representation of the rotor showing the placement of disks when Eq. (1) of the text applies.

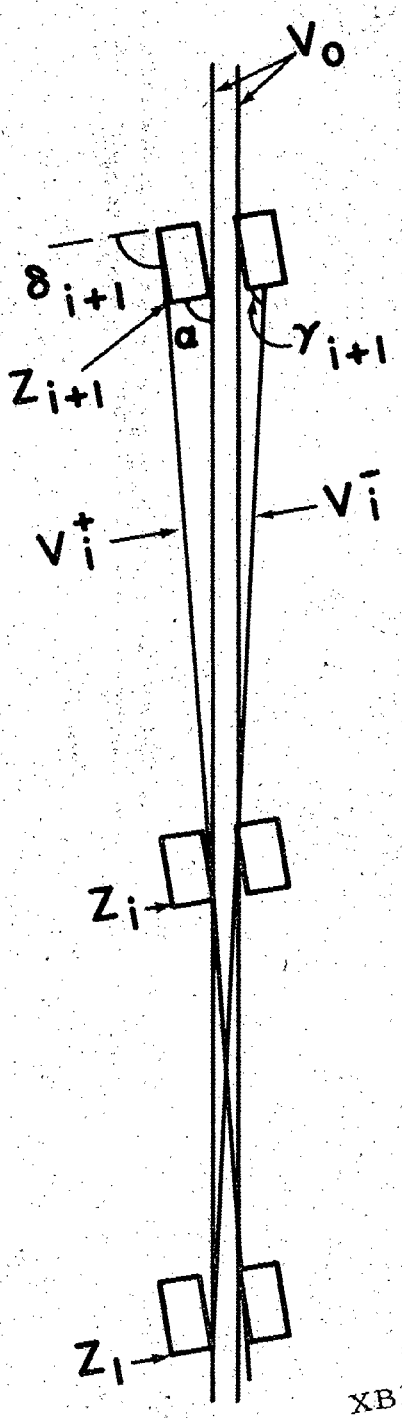

XBL 706-1281

Figure 6

the elimination of both v_i^- and v_i^+. This is achieved when both these velocities are just barely intercepted. This would be accomplished if

$$Z_{i+1} \cot \gamma_{i+1} - Z_{i+1} \cot \alpha = \ell_1 + \ell_2$$

and

$$Z_{i+1} \cot \alpha - Z_{i+1} \cot \delta_{i+1} = \ell_1 + \ell_2.$$

This imposes the condition on v_0 that

$$\cot \alpha = \ell_1/d$$

which requires that $\alpha = \gamma_2$. In this case the transmission of the rotor would be zero at the design velocity, because γ_2 is the angle of the trajectory of v_1^-. Therefore a greater α would have to be used, necessitating the placement of the disks according to the equation derived above.

A bonus of this method of disk placement is that any number of the last disks can be removed and the first ones will still be a sideband-free velocity selector. This will, of course, reduce the resolution considerably, but the rotor will be shorter allowing greater beam intensities due to reduction of the inverse square law loss.

In order to allow a tolerance in alignment of the disks, the above calculations should be made assuming a slit width, ℓ_1, larger than the actual value. Then to compensate for disk deviations from planar configuration, a suitable value should be subtracted from the value of Z calculated for one disk before the position of the next is calculated.

3. Construction

The slotted disks are fabricated from flat, 1/16" thick alcoa 6061-T6 aluminum alloy sheet. Eighteen plates of approximate diameter are clamped between heavy aluminum end plates; a 3/8" hole is drilled and reamed through the center and the whole assembly is screwed together by

means of a 3/8" shaft which is threaded at both ends and inserted through the holes. After turning to the final diameter in a lathe, the disks are clamped in a dividing head on a mill. The 240 slots are milled axially around the circumference with a 0.032" thick circular high speed steel saw. The slots are cut in four groups of equally spaced cuts; after each set of slots is milled, they are filled with black wax and then the next set is cut. This is the procedure suggested by Trujillo et al.[14] except that the black wax was substituted for the epoxy resin used in the preceding reference in order to facilitate removal after completing the cutting. This procedure is necessary in order to prevent bending of the teeth away from the tool when the adjacent slot has already been cut. Before unclamping the finished disks, the teeth are marked so that it is possible to determine which slot in each disk was milled by the same cut. Each disk is mounted on a spindle with a 3/8"shaft and clamped with a collar that has the same outside diameter of the final disk spacers. Each disk is placed in a lathe and a dial indicator is used to measure any deviations from planar configuration; these deviations as well as the thickness of each disk are recorded. The seven best disks are chosen and the length of the disk spacers and the phase angles are calculated to compensate as much as possible for the deviations in each disk. The residual deviations are then well within the tolerances allowed when the spacings of the disks were calculated. These tolerances were $\pm 0.019^{\circ}$ in the phase angle of the disks and ±0.003" for the spacing between disks; deviations of these magnitudes will allow no sidebands to pass but will reduce the transmission of the selector and therefore should be eliminated to as great an extent as possible.

The rotor is finally assembled on a 0.9525 cm dia. drill rod that is threaded at one end and drilled and tapped for a 1/4 - 28 NF. socket head screw. The disks with the 3.81 cm dia. disk spacers of the proper length are placed on the shaft; care is taken to ensure that all disks are facing the way that they were when milled. A collar and a bearing with collars designed to constitute the proper shaft housing are added at each end; also a waffle lock washer is included between the bearing collar and the outer disk collar. A pair of 3/8 - 24 NF lock nuts on the threaded end with the socket head screw on the other end allow the whole system to be tightened together to prevent both slipping of the disks with respect to each other and rotation of the inner races of the bearings with respect to the shaft.

The bearings selected are Barden SR6 - FFTA5 G6. This bearing has a phenolic retainer which keeps the ball bearings separated and is porous to guarantee complete lubrication of the bearing. Lubrication is provided by a grease that is included in the bearing at the factory; the bearing has shields which hold the grease in the bearing, prevent contaminants from entering and minimize outgasing. The bearings are stiff when new, but when put in use, the grease "channels" and bleeds in oil slowly. This bearing has a large radial play in order to accomodate more lubricant. These bearings have given very good performance, but a similar bearing using a stainless steel retainer was less successful. Even with the phenolic retainer after extended use of these bearings the grease dries out, preventing good lubrication. This grease can be removed with acetone and the bearing relubricated with Aeroshell Fluid 12 (obtained from Rotor Lab, Lawrence Radiation Laboratory, Livermore.) These regenerated

bearings have then been used and have given satisfactory performance. A major drawback of the design of this rotor is that in order to replace the bearings, the rotor must be disassembled, destroying the disk alignment; realignment and rebalancing of the rotor is then required.

Alignment of the rotor is accomplished by the method of Trujillo, et al.[14], utilizing a vernier height gauge. After assembling the rotor with a light coating of graphite between the collars, bearing and waffle washer at each end, the lock nuts are set and locked at a position where the tightening of the socket head screw will lock the assembly. The screw is then backed off to allow easy but tight movement of the disks with respect to each other. The alignment takes place on a large, flat assembly surface; the rotor is resting on its bearings in "V" blocks that have been carefully aligned with respect to each other. The vernier height gauge is used to measure the distance that the top of the outer diameter of the bearing is above the assembly surface. The method of measurement that is the easiest and most accurate is to set the height gauge on a piece of paper of uniform thickness to electrically insulate it from the assembly surface; by attaching one lead of a resistance meter to the height gauge and the other to the assembly surface, the exact position where the gauge makes contact with the bearing may be easily seen from the drop of the resistance. From the heights of both bearings the height of each end of the center of the shaft is obtained by subtracting the radius of the bearing. From these data and the calculated phase angles of each disk and the disk radius, the proper height of a given references slot above the assembly surface may be calculated for each disk. (This reference slot is a slot on each disk that was cut on a

given pass of the saw blade; this is necessary so that small inaccuracies in the milling cause minimal impairment of the operation of the selector). Starting with the first disk, every second disk is set to the proper positions by setting the gauge height and then rotating the disk until electrical contact is made at the radius (the procedure is exactly the same as that discussed in Ref. 14.) These disks are then held in position with surface gauges; care must be taken to ensure that there is no tension in the disk which would cause the disk to move when this surface gauge is removed. When these four disks are properly positioned the three intervening disks are similarly positioned; however, surface gauges are not necessary to hold these disks. When all seven disks have been properly placed, the surface gauges are gingerly removed and the socket head screw is tightened very, very carefully. When the screw is tightened to the full extent possible, the positioning is rechecked. Needless to say this procedure is a very unsatisfactory one, consuming much time and nervous energy, and often the disks move during tightening, causing the repetition of the entire process. A further very serious failure of this system is caused by the difference in thermal expansion coefficients between the steel shaft and the aluminum spacers. If the roter is allowed to cool to a low enough temperature the spacers contract enough to relieve the pressure and allow the disks to slip, destroying the alignment. The waffle lock washers are partially successful in preventing this catastrophe but it is has occurred once. A different method of mounting the disks would be desireable; The method present by Trujillo, et al.[14] is attractive but would not be possible for the first few disks due to the close spacing required in the disk placement system used here.

Since the rotor was intended to be run at speeds up to 40,000 rpm, it is crucial that it be very carefully balanced. After alignment the rotor was dynamically balanced at the rotor laboratory at the Lawrence Radiation Laboratory, Livermore.

The rotor is held in its housing in bearing sleeves, each of which is supported around its outside diameter by two concentric natural rubber O-rings[18] of 40 Durel Hardness. (These O-rings are obtained from R. W. Scott and Co, 2345 - 4th Street, Berkeley, California. Dimensions and index numbers are: 6227 - 31, 1-7/8"x2-1/4"x3/16" and 6227 - 34, 2-1/4"x 2-5/8"x 3/16"). The function of these O-rings is the same as that of the springs described in Ref. 14: the flexibility allows the bearings to move slightly so that the rotor may find its own axis. of rotation. An additional similar O-ring (6227-28, 1-1/2"x1-7/8"x3/16") is situated at the outside face of each bearing sleeve; provision is made for adjustable compression of these O-rings to provide the proper axial thrust for the bearings.

The rotor is coupled directly to a IMC Magnetics Corp. BT 2910 H-1 hysteresis synchronous motor by means of a coupling constructed from two brass caps connected with a 1-5/16" length of number 15 music wire. The caps fit over the ends of the rotor and motor shafts and are held in place with set screws. The music wire provides a flexible coupling and allows the rotor shaft to move with respect to the motor shaft. The motor is positioned with the aid of a dial indicator so that the two shafts are on the same line.

The motor has two ranges of operation utilizing two sets of windings. Low speed operation (13 to 131 Hz) uses a four pole, two phase system while

the high speed mode (66 to 660 Hz) utilizes a two pole, two phase winding. The motor was specially designed to produce at least 1 oz. in. of torgue throughout the 400 to 40,000 rpm rotational speed range; a power input of approximately 130 watts is required at 40,000 rpm.

4. Operation

The velocity selector motor is driven by a synchronous motor driver designed at the Lawrence Radiation Laboratory. This design incorporates a N. J. E. Corp. Model QR-15-20 dc power supply to drive the oscillator system. A very ragged square wave is produced which, nevertheless, drives the motor very satisfactorily; however, it is necessary to use only the minimum voltage possible to operate the motor in order to prevent over heating. The power input is monitored on an oscilliscope; a slight, slow oscillation of the shape of the input waveform indicates that the motor is locked in. This oscillation is also observable in the output voltage guage of the power supply. The frequency of rotation is measured with a Hewlett - Packard Model 522B electronic counter which is triggered by the power supply. In the low frequency, four pole mode, the input power frequency is twice the rotational frequency of the motor, while in the high frequency mode, the two frequencies are equal.

A light sensitive diode placed on the opposite side of a disk from a light bulb so that the slots pass between the two provides a convenient means for verifying that the velocity selector rotor is turning at the same speed as the motor.

5. Performance

In Fig. 7 a comparison of a measured velocity distribution with theory is presented. At these extremely low source pressures,

Figure 7.

Velocity distributions of a thermal, effusive beam. The data points were measured for Tl at a pressure of 5×10^{-4} Torr and at a temperature of 1150°K. The dashed curve is that expected for a Maxwell-Boltzman gas effusing from a slit and passing through the selector. The solid curve is the result obtained by numerically integrating the dashed curve over the geometrically calculated transmission function of the source slit, rotor and detector assembly; the angular divergence of the parent beam is taken into account, but a complete lack of slit clogging in the first disk is assumed. The data points and the solid curve have been divided by a factor of velocity to correct for the increase of transmission with velocity. The intensities, normalized to 1.0 at the peak heights, are plotted against reduced velocities. V_{mp} is the most probable velocity in each of the distributions. For the experimental points $V_{mp} = 3.79\times10^{4}$ cm/sec assuming perfect alignment of the source slit and detector with the rotor shaft. For the dashed curve, $V_{mp} = \sqrt{(3/2)}\,\alpha = 3.75\times10^{4}$ cm/sec where $\alpha = \sqrt{(2\ kT/m)}$. The integration yields $V_{mp} = 3.70\times10^{4}$ cm/sec for the solid curve.

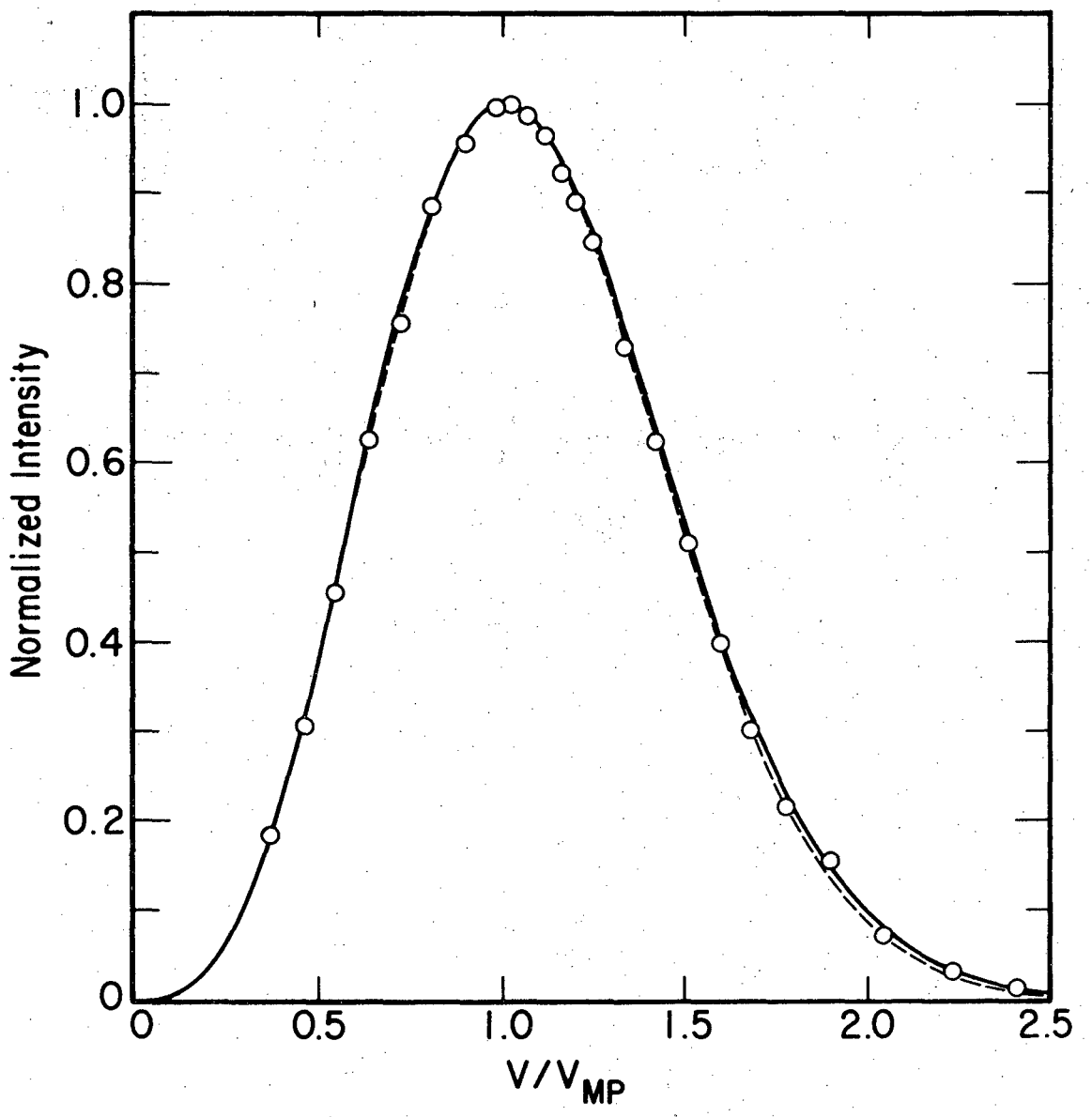

XBL 709-6556

Figure 7

excellent agreement is typical but at higher pressures, the experimental distribution narrows and moves to higher velocities due to departure from effusive flow conditions. A computer program has been written that integrates the parent velocity distribution over the transmission function; this function depends not only on the geometry of the rotor, but also on divergence in the beam, partial clogging of the first disk's slots and misalignment of the detector and source slit with respect to the rotor shaft. All of these factors are treated in the computor program. A complete discussion of this transmission function as well as calibration of the selector will be presented in the following chapter which describes experiments carried out using this velocity selector.

In Fig. 7 the shift of V_{mp} of the integrated curve with respect to that of the Maxwell-Boltzmann curve is due to the lack of symmetry in the transmission function; the deviation of the experimental V_{mp} is ascribed to a small misalignment angle of the beam with the rotor axis. The discernable narrowness of the data points with respect to the solid theoretical curve can be partly accounted for by assuming a partial blocking of the first disk's slots. The distribution was run after the selector had been used for a considerable time without cleaning and this clogging was neglected in the integration.

Clogging of the slots is a problem when a Tl beam is being selected. The Tl is very readily removed by amalgmating with Hg; however, this procedure has its drawbacks and a solution of KI is generally used to dissolve the Tl. A graver difficulty is presented when an alkali metal beam is being selected; when the rotor is exposed to moist air, the alkali hydroxide is produced which gradually hydrolyzes the aluminum disks.

Therefore, care is taken to quickly clean the disks after an experiment with an alkali metal.

The major problem encountered in using this selector is achieving proper alignment of the beam with the selector rotor axis. The problem is exaggerated by the thermal expansion of the beam source oven which was discussed in an earlier section; consequently a calibration procedure to be discussed later must be relied upon. If this thermal expansion can be eliminated the alignment procedure suggested by Richman and Wharton[19] may prove very helpful; in their work a mirror mounted perpendicular to the shaft axis is used for alignment by autoreflection along the beam path.

The velocity selector has given reasonably trouble free performance when operated at low speeds. An improved coupling between the rotor and the motor would be desirable; the use of a speedometer cable with ends shaped to fit into square holes in the ends of the motor and rotor shafts has been suggested but not tried. The highest speed reached was 33,000 rpm. but the bearing changes which have been made will hopefully allow the achievement of the design rotational frequency in the future.

E. Beam Monitors

The surface ionization detector that is described in Chapter II is used to continuously monitor the Tl beam intensity. The tungsten filament is operated at 1300°K and no oxygenation is required. Except for a very large, unexplained background that occasionally appears it has given excellent results.

A continuously deposited potassium surface is used to monitor the metastable beam intensity by measuring the current due to the electrons

ejected by the Auger de-excitation of the excited atoms. The details of this detector will be described elsewhere;[20] the current is measured by a Cary Electrometer, or alternatively, for accurate calibration curves, such as shown in Fig. 3 by a Princeton Applied Research Model HR-8 Lock-in amplifier. During an experiment the signals from the two beam monitors are continuously recorded by a Leeds and Northrup Speedomax G, two pin recording potentiometer.

Hagstrum[21] has presented a complete theory of Auger ejection of electrons from metals. His theory treats atomically clean surfaces only; this situation certainly does not pertain to our apparatus, but applying his results to a potassium surface allows upper limits of the detection efficiencies to be set: for Hg $^3P_0$ and $^3P_2$ the values .057 and .084 are obtained, respectively. These results coupled with the maximum current measured allows the calculation of a lower limit of 0.0013% for the fractional excitation of the mercury beam by the electron gun. A crude calculation using the excitation cross section from Ref. 4 suggests that the percent excitation should be approximately a factor of 8 times greater. This is taken to indicate that the detector employed here has a detection efficiency of only about 13% of that expected for a clean potassium surface. This efficiency is sufficient for our purposes but could probably be improved greatly. For example, achievement of a clean surface and acceleration of the ejected electrons into an electron multiplier should increase the detection efficiency by a factor of 10^8 to 10^9.

The above calculations have assumed that the lifetimes of these two metastable states are long with respect to the time of flight from the electron gun to the detector. The $^3P_0$ state can only radiate to the

ground $^1S_0$ state; this radiation, therefore, is forbidden for all types of radiation by the selection rule J = 0 does not combine with J = 0. In view of this consideration, the lifetime of $4.2\ 10^{-4}$ sec given by Cvetanovic[22] must be held in some suspicion. Indeed, in his discussion of forbidden transitions Garstang[23] quotes a calculation that gives 5×10^{-9} as the value of the intensity ratio of the $^3P_0 \rightarrow {}^1S_0$ transition to the $^3P_1 \rightarrow {}^1S_0$ transition; taking the lifetime of the $^3P_1$ state as $1.1\ 10^{-7}$ sec [24] a lifetime of 2.4 seciis derived for the $^3P_0$ state. The above intensity ratio is reportedly[23] in good agreement with an experimental measurement. The theory used to derive the above intensity ratio assumes that the transition is brought about in only the Hg isotopis with odd atomic weights due to perturbations of the electronic energy levels by hyperfine interactions with the nuclear spin; the nuclear spin is zero for the isotopes with even atomic weights. Grastang also reports that this treatment was substantiated by an experiment with a Cd resonance lamp using Cd that had the odd isotopes enriched; the analogous intensity ratio was increased in proportion to the amount of odd isotopes present. This discussion is rather academic since the $^3P_0$ accounts for probably somewhat less than 14% of the signal. For the $^3P_2$ state radiation is forbidden to the ground state for electric dipole, electric quadrupole, and magnetic dipole radiation; radiation to the $^3P_1$ state is forbidden for electric dipole, but allowed for magnetic dipole and electric quadrupole. A life time of approximately 0.1 sec.[3b] is derived if the principal mode of decay is assumed to be a magnetic dipole transition to the $^3P_1$ state. The conclusion from this discussion is that no significant emission attenuation of the metastable intensity occurs between excitation and detection.

The Auger detector is expected to be sensitive to ultra-violet photons by means of the photoelectric effect. Since Hg $^3P_1$ (which radiates at 2537Å) has an excitation cross section[2] comparable to that of $^3P_2$, emission from that state might be expected to produce a spurious signal that would be dependent on the electron beam. However, since the lifetime of the state is short (10^{-7} sec) all these excited atoms would radiate before leaving the excitation region. The Auger detector subtends only a very small solid angle compared to the 4π steradians to the emitted photons. Thus, only a negligible effect is expected. This prediction was verified by moving a suprasil-2 window in front of the detector; the electron beam dependent signal was completely quenched. Care was taken to be sure that the window was not coated with mercury before moving into the beam; the transparency of the window at 2537Å was verified in a Cary ultraviolet spectrometer immediately upon opening the apparatus after the experiment.

F. Photon Detection System

1. Photomultiplier System

To detect the radiation from the collisionally formed, electronically excited species, an EMI-9558 QB photomuliplier tube is placed directly below the scattering center. This tube was chosen with several considerations in mind. It is fitted with a Spectrosil (fused silica) window yielding on extremely wide spectral range (1650 - 8500)Å. The S-20 type trialkali cathode provides a very high (27% at 2000Å) quantum efficiency. A very low dark current (15 counts/sec) can be achieved by cooling to -40°C. The relatively low maximum gain (2×10^6 to 2×10^7) and wide distribution of pulse heights reduces the value of the tube for counting;

no plateau was found in the curve of count rate versus applied voltage, but satisfactory counting performance was achieved at 1000 volts corresponding to a gain of 8×10^6. In order to prevent interference of the performance of the photomultiplier by magnetic fields in the apparatus, the tube is surrounded by a tubular mu metal shield and an outer soft iron shield; these shields are fairly well standardized at the Lawrence Radiation Laboratory.

A very narrow band pass interference filter[25] is located directly above the photomultiplier tube. The peak transmission and band width varied widely from filter to filter; typical values were 10 to 50% and 20 to 75Å FWHM respectively. The transmission declined and the bandwidth widened as the desired wavelength of the peak was shortened. Outside of the band pass region, the filter transmitted less than 0.1% at all wavelengths where the photomultiplier was sensitive. Since the peak wavelength position is a critical function of temperature, it is necessary to keep the filter close to room temperature; in order to do this the complete photomultiplier, filter and lens assembly was wrapped with heating wires and the temperature monitored with a thermocouple. Without this heating, radiation to the surrounding liquid nitrogen surfaces cooled the assembly. Maintaining the photomultiplier at room temperature prevents the achievement of the minimum dark current, but counts from transmission through the filter of black body radiation from heating elements were much more numerous than the dark current counts.

A system of three lenses and a diaphragm, located above the filter collects the emitted light and renders it parallel for transmission through the filter. The first two lenses collect and refocus the

light at the aperture of the diaphragm; this refocusing is intended to allow only light originating from the collision zone or passing through it to reach the filter. The last lens then makes the diverging light parallel.

A spherical mirror with front surface silvering is suspended above the scattering center to increase the fraction of the emitted photons which may be collected. By locating it at a distance equal to its focal length above the collision zone, it should reflect most of the upward directed photons back through the scattering region to the condensing lenses.

The mirror, lenses and filter are held in a tubular, light tight mount (see Fig. 1). The beams enter and exit through ports in the side. Various arrangements of tubular light shields surrounding the beams have been tried; Fig. 1. shows a tube completely enclosing the Hg^* beam path except for a small slot at the collision zone. This arrangement was used when investigating a state that emitted at a wavelength near 2556Å, the emission line of Hg $^1P_0$, or 2271Å, the emission line of Hg $^3P_2$. When one of these lines was within the tail of the band pass of the filter, a high photon signal, which depended on the electron beam, was observed, and the indicated light shield minimized this signal.

2. Pulse Amplifer and Discriminator

The electronics of the counting system are depicted in a block diagram in Fig. 8. The pulses from the photomultiplier are amplified by a Lawrence Radiation Laboratory pulse amplifier with an input impedance of 50 ohms and a gain of greater than 200. With this amplifier it is very difficult to prevent echoing and even continuous oscillations in the transmission cable; a balance between large amplification and reasonable

Figure 8.

Schematic diagram of the electronic components of the counting system.

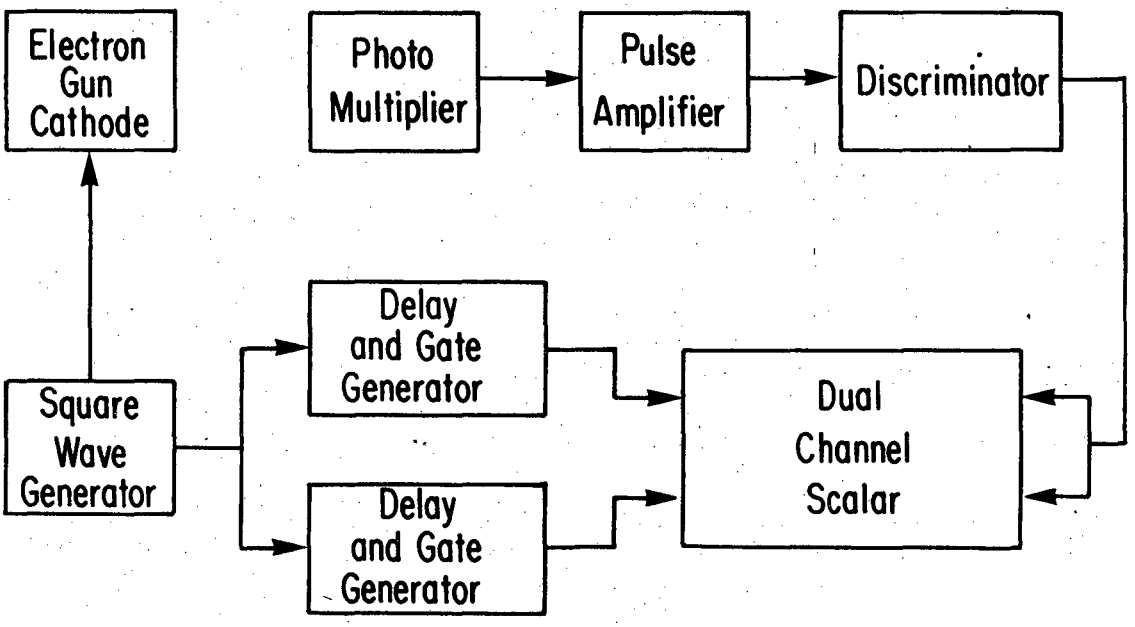
Electron Gun Cathode
Photo Multiplier
Pulse Amplifier
Discriminator
Delay and Gate Generator
Square Wave Generator
Dual Channel Scalar
Delay and Gate Generator
XBL 706-1278

Figure 8

pulse shape had to be struck. Performance is adequate, but a better system incorporating a discriminator would be desirable.

A pulse discriminator is necessary to eliminate pulses below a certain height and render the larger ones a uniform shape and height. A Lawrence Radiation Laboratory surplus 10 megacycle descriminator is utilized; however, pulses near the threshold are transmitted with reduced amplitude. Since each pulse is transmitted through separate cables to the two channels of the scalar, small differenes in the cable impedance and input characteristics of the channels cause some pulses to register on one scale but not the other. By including a second identical discriminator after the first, the difference between the two count rates is reduced to less than .01%.

The scalar requires a negative pulse, but the pulse amplifier produces a positive pulse. Consequently, a pulse inverted is included between the discriminator and scalar.

3. Counting System

In order to separate the emission signal from the large black-body radiation back ground, it was deemed desirable to use a frequency sensitive detection system. By chopping the electron beam, and thus the beam of metastable atoms, and by counting for a period of time while the beam was off and then for an equal period with the beam on, the difference in the counting rate, apart from the statistical fluctuations, should represent the signal. For a typical experiment with a total counting time of 100 seconds approximately 50,000 counts are recorded on each channel with a difference of about 3000; this would imply a statistical standard deviation of 10.5% in the signal.

At the heart of the system is a Transistor Specialties, Inc., Model 1535 Dual Channel, 100 megacycle pulse counter. It is designed so that each channel may be gated separately; however, the rise time of the gating system was slow in the design mode of coupling. Also one pulse was needed to start and another to stop the gate. A modification was made to allow the gate to be open only when +2 volts or greater is applied to the gate input; the rise and fall time were decreased to 30 and 5 nanoseconds respectively.

As discussed in previous sections the electron beam is chopped by applying a square wave to the electron gun cathode. The frequency of the square wave may be varied from 7 Hz to 10KHz but all experiments have been run with a period of 25 milliseconds. The square wave also triggers the two gate generators.

Each of the delay and gate generators is a Berkeley Nucleonics Co., Model CT-1, Del-A-Gate. It is capable of generating a pulse with rise and fall times of 10 nanoseconds and a period of from .05 microseconds to 10 milliseconds; the pulse may also be delayed from .05 microseconds to 10 milliseconds after triggering. Triggering may be accomplished by either a positive or a negative going pulse.

During an experiment the negative going leg of the square wave triggers Del-A-Gate "A" and turns of the electron beam; a delay of 2 msec and then a pulse of 10 msec is generated. This pulse gates channel "A" of the scalar and thus it counts for 10 msec starting 2 msec after the electron beam is turned on. This delay allows the electron beam to reach its equilibrium current flow and the metastable beam at the scattering center to reach its maximum intensity for all atomic velocities before counting

commences. The gate ends before the electron beam is turned off. The operation of Del-A-Gate "B" and channel "B" is identical, except that the positive going leg provides the trigger; thus channel "B" counts only while the electron beam is off and all metastable atoms have left the scattering zone. The internal test function of the scalar is used to set the two gate periods to be equal within at least 0.1%; this uncertainty in the relative channel readings has always been much less than the statistical uncertainty in the recorded counts during an experiment. For statistical analysis of the data, both channel readings, not simply the difference between the two readings, are recorded. The counting times required varies depending on the signal to background ratio and total counting rate, but is typically 50 or 100 seconds; however, a counting period of 500 seconds has been used with some success.

G. Performance

The apparatus is currently, if tenuously, operating. The next chapter describes some experiments which have been carried out.

REFERENCES

1. For recent reviews see B. L. Moiseiwitsch and S. J. Smith, Rev. Mod. Phys., 40, 238 (1968), and references cited therein.
2. J. C. McConnell and B. L. Moiseiwitsch, J. Phys. B (Proc. Phys. Soc.), Series 2, 1, 406 (1968).
3. (a) W. Lichten, Phys. Rev. 109, 1191 (1958); (b) M. N. McDermott and W. L. Lichten, Phys. Rev. 119, 134 (1960).
4. W. L. Borst, Phys. Rev. 181, 257 (1969).
5. L. Brillouin, Phys. Rev. 67, 260 (1945).
6. A. V. Haeff, Proc. I. R. E. 27, 586 (1939).
7. Actually, the region between the plates is not completely filled because the electrons directly adajacent to the plates will be removed by collisions with the plate on the outer part of the spiral. However, since the diameter of the approximately spiral path is only .004 cm, this effect is neglected.
8. F. Rosebury, Handbook of Electron Tube and Vacuum Techniques (Addison-Wesley Co., Reading, Mass., 1965) p. 103.
9. R. C. Weast, ed., Handbook of Chemistry and Physics (Chemical Rubber Co., Cleveland, 1967), 48th edition.
10. Both McConnell and Moiseiwitsch's theoretical calculations (Ref. 2) and simple probability agruments indicate that the cross-section for $^3P_0$ should be of the order of 20% of the cross section of $^3P_2$. No experimental measurement of the relative magnitudes has yet been made.
11. J. G. Dash and H. S. Sommers, Jr., Rev. Sci. Instr. 24, 91 (1953).
12. R. C. Miller and P. Kusch, Phys. Rev. 99, 1314 (1955).

13. S. U. Hostettler and R. B. Bernstein, Rev. Sci. Instr. 31, 872 (1960).

14. S. M. Trujillo, P. K. Rol, and E. W. Rothe, Rev. Sci. Instr. 33, 841 (1962).

15. J. L. Kinsey, Rev. Sci. Instr. 37, 61 (1966).

16. A. E. Grosser, Rev. Sci. Instr. 38, 257 (1967).

17. A. Kristensen, R. L. Palmer, H. Saltsberg, and J. N. Smith, Jr., Rev. Sci. Instr. 38, 987 (1967).

17a. L. T. Cowley, M. A. D. Fluendy, and K. P. Lowley, Rev. Sci. Instr. 41, 666 (1970).

18. I am indebted to Dr. Troy Story for suggesting this mounting concept and to Ching-Hon Loh for designing the mount used here.

19. E. Richman and L. Wharton, J. Chem. Phys. 53, 945 (1970).

20. C. H. Loh, Ph.D. Thesis, University of California, Berkeley.

21. H. D. Hagstrum, Phys. Rev., 96, 336 (1954).

22. R. J. Cvetanovic, Prog. in Reaction Kinetics, 2, 41 (1964).

23. R. H. Garstang, "Forbidden Transitions" in Atomic and Molecular Processes, (D. R. Bates, ed , Academic Press, New York, 1962)p. 1.

24. J. G. Calvert and J. N. Pitts, Jr., Photochemistry (J. Wiley and Sons, Inc., New York, 1966) p. 58.

25. These filters have been purchased from Baird-Atomic and Corion Instrument Corp. Neither company gave satisfactory service nor was able to produce orders promised.

APPENDIX A

List of Appartus Drawings and UCRL Numbers*

1. Ovens and Cold Shields

Low Temperature Double Chamber Oven	12N	1401
Oven Thimble	12N	1381
Oven Thimble Clamp	12N	1391
Oven Clamp	12N	1951
Velocity Selector, High Temperature Double Chamber Oven	12N	2622
High Temperature Oven Cold Shield	12N	2653
High Temperature Oven Support Tube	12N	2561
High Temperature Oven Clamp	12N	3621
High Temperature Oven Clamp Support	12N	2601

2. Velocity Selector Liquid Nitrogen Trap and Cold Shields

Liquid Nitrogen Trap	12N	2704
Velocity Selector and Trap Support	12N	2694
Liquid Nitrogen Trap Insulators	12N	2571
Velocity Selector Support Spacer	12N	2021
Flange Mount	12N	2043
Flange Attachment	12N	2053
Cold Shield Support Plate	12N	2683
Cold Shield Front Panel	12N	2642
Cold Shield Side Panel	12N	2673
Liquid Nitrogen Fill Tube Flange	12N	3633

3. Electron Gun		
Impregnated Cathode	12N	3411
4. Velocity Selector		
Rotor Assembly Diagram	12N	1053
Rotor Shaft	12N	1073
Slotted Disk	12N	1063
Front Bearing Collar	12N	1011
Inner Bearing Collar	12N	1021
End Disk Spacer	12N	1041
Bearing Sleeve	12N	2971
Front Mount Plate	14D	2992
Front Cover Plate	14D	3002
Back Mount Plate	14D	3012
Motor Mount Plate	12N	1582
Side Mount Plate	12N	1613
Motor Plate Support	12N	1481
Mount Plate Support	12N	1531
5. Photomultiplier Mount		
Fluorescence Light Shield	12N	3853

*See Appendix A, Chapter II; many of the apparatus components whose drawings are listed there were utilized in this study. The above is only a partial list of the new components constructed for this apparatus; the pieces not listed were constructed by the experimenters and there are no drawings on file. Extensive changes have been made in some of the pieces depicted in the drawings and these changes have not been recorded on the drawings.

APPENDIX B

List of Apparatus Electronics Diagrams and UCRL Numbers*

Synchronous Motor Driver	8S	6673
Pulse Amplifier	8S	6462
10 MC Discriminator	3X	9994
Square Wave Generator	8S	8922

---

*See Appendix B, Chapter II; many of the apparatus components whose drawings are listed there were included in this apparatus.

VII. VELOCITY DEPENDENCE OF Hg^* + Tl COLLISIONAL EXCITATION TRANSFER

A. Introduction

In 1922 Franck predicted that a transfer of electronic energy could occur between an excited atom and a ground state atom of a different species.[1] This prediction was soon verified when Cario and Franck observed radiation from the excited states of thallium when a mixture of mercury and thallium vapors was irradiated with the Hg 2537Å line.[2] This process was labeled "sensitized fluorescene"; it has also been referred to as collisions of the second kind. In the two decades following this pioneering study investigations were extended to many different systems. A review[2a] has summarized this early work and has shown how the results conform to four selection rules: (1) as the difference between the energy level of the doner atom and the energy level of the recipient atom increases, the emitted intensity decreases; (2) if the energy level of the recipient atom is higher than the energy level of the doner atom, the emitted intensity is less than that found for a similar energy discrepancy but with the order of the energies switched (presumably this is due simply to the fraction of collisions which occur without enough relative kinetic energy to make-up for the energy discrepancy in the former case); (3) the Wigner spin rule is obeyed, i.e. the total spin of the system does not change; and (4) for the most likely transitions the total electron angular momentum of the system does not change. Later investigations have studied the effects of changing such conditions as the pressure of foreign gases and the temperature and pressure of the two collision species.[3] As discussed in Ref. 3 the experimental conditions were generally complex and ill defined in these

early studies; for example the identity of all initial excited states was often in doubt or the role of the Hg_2 or the HgTl molecule was not established. Attempts have been made to study the temperature dependence of the energy transfer.[4,5] These experiments have all been performed in a bulb with solid or liquid samples of the reagents enclosed. In order to vary the translational energy of the collision partners, it was necessary to change the temperature of the experimental vessel.[4] Concomitant with this energy change was a pressure change which obscured effects due solely to the energy variation. In addition, an unknown pressure of impurities due to outgassing from the walls of the sealed container must certainly have been present. This presence is likely to have a strong effect that would certainly vary with temperature. Thus, it is not clear how much credence can be attached even to the gross temperature dependence of the total cross sections that have been previously reported.

Utilization of the apparatus described in the previous chapter allows not only greatly improved control of the identity of the incident species, but also permits the incident relative translational energy to be varied independently of any other parameter of the system. However, it would be very difficult to obtain absolute values of the cross sections (which can be obtained with good accuracy in the bulb experiments) and thus the two techniques are complementary. Low velocity resolution measurements of the velocity dependence of the effective cross section for collisional excitation of the Tl 5350Å fluorescence by Hg $^3P_{0,2}$ have been made in this apparatus and they will be presented here.

Figure 1 presents an energy level diagram for thallium. All of the thallium emission lines that have been reported in previous studies of

mercury sensitized fluorescence are included. The two lower metastable states of mercury (which are the two levels excited in the experiment to be described) are also indicated.

B. Experimental Conditions

A complete discussion of the apparatus and data gathering procedures is given in the preceding chapter. The two beams are prepared in the double chamber oven sources; the temperature of all four chambers are periodically checked and maintained as constant as possible throughout the experiment. The upper chambers are maintained ~100°C above the lower chambers to prevent any condensation or clogging in the upper oven or at the oven slits; this temperature differential also minimizes any possible dimer concentration. Typical operating pressures are one to two Torr in each oven. The Hg_2 molecule is known but its measured bond dissociation energy is so small[5a] that its concentration is inconsequential in this study. The dimer of Tl has not been reported and no evidence of it has been seen in the velocity distributions measured in this study.

The electron beam is set to 0.30 mamps before starting the experiment. The plate and collector voltage is adjusted to the peak of the excitation function (see Fig. 3 of Chapter VI). Throughout the experiment the electron beam current is monitored and held at its initial value.

Before the Tl oven is brought up to its operating temperature to start the experiment, a velocity distribution of the parent beam is measured at very low source pressures. These data in the form of transmitted beam flux intensity as a function of rotor rotational frequency are necessary to calibrate the velocity selector. This calibration procedure is discussed in detail in the next section.

Figure 1.

Thallium energy level diagram. All energies are given in electron volts. For Tl levels below 4 eV the energy of the level above the ground state is indicated, but for the higher energies the difference between the Tl level and the nearest metastable Hg level is given. Note the scale change at 4 eV. The two lower dashed lines indicate the energies of the low lying metastable Hg levels, while the upper dashed line gives the Tl ionization potential. The diagonal lines indicate the emission lines observed in the mercury sensitized fluoresence spectrum of thallium; the number labeling each line gives the wavelength in Å.

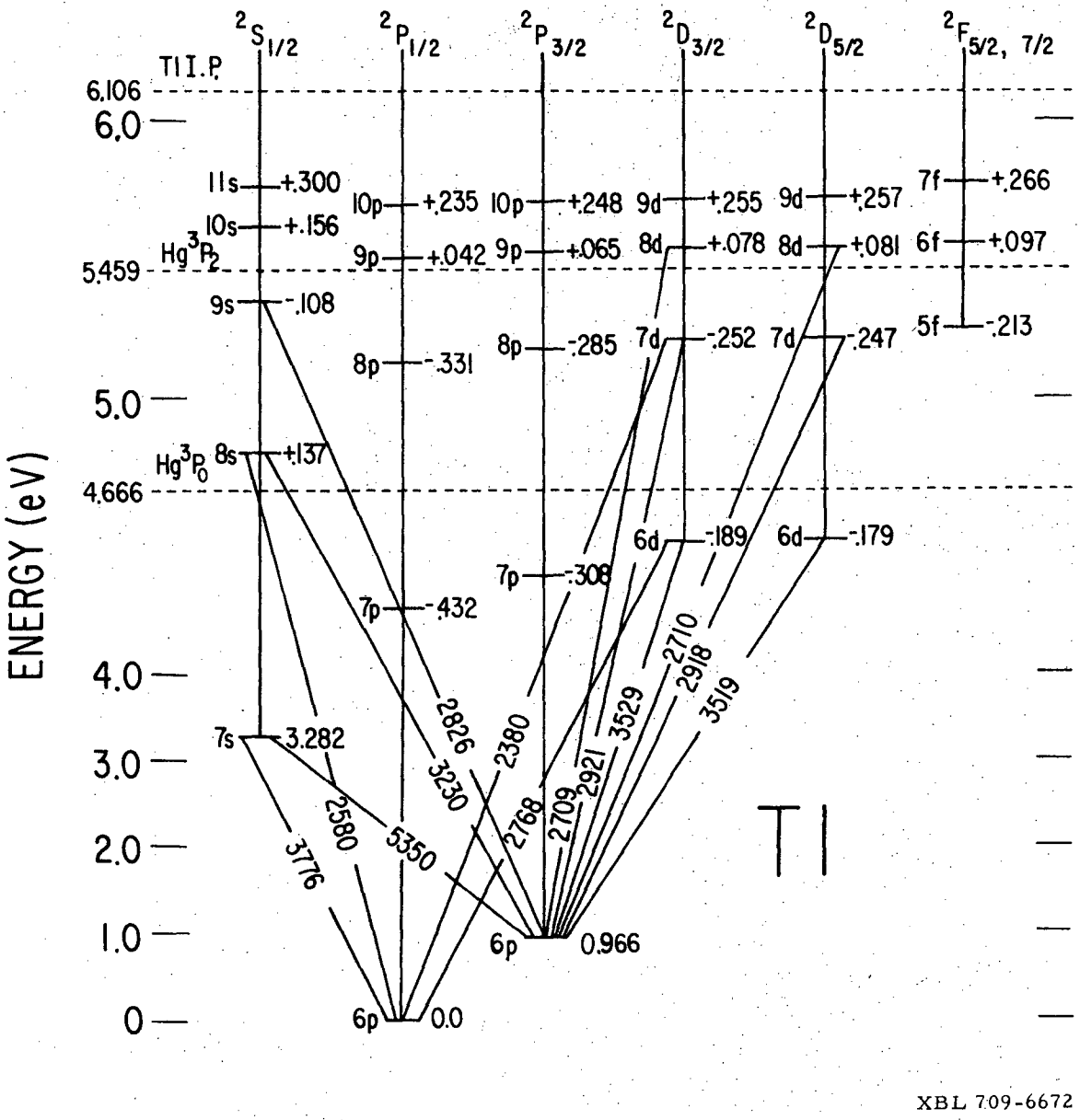

XBL 709-6672

Figure 1

The two scalar channels must also be set to count for equal periods with proper delays after the electron beam is turned on or off. The calibration procedure is discussed in the previous chapter. The data are not a critical function of the delay times so no effort is made to set them to great accuracy nor to constantly monitor them; they have been found to remain approximately constant. The counting times, on the other hand, are extremely critical and are subject to slight drifts; therefore they are periodically monitored and adjusted if necessary.

During an experimental run the photomultiplier is heated as necessary to maintain the temperature of the interference filter near 20°C; the peak wavelength transmitted is reported to shift toward shorter wavelengths at a rate of 1Å per 5.5°C. Typical background pressure in the apparatus is 1.5×10^{-6} Torr (uncorrected ion gauge reading). If the background pressure were high enough to appreciably attenuate the Tl beam, the measured Tl beam flux at different Tl velocities would not accurately reflect the true Tl flux at the collision zone because the extent of attenuation would be expected to be a strong function of velocity. The good agreement of measured Tl velocity distributions with the theoretical Maxwell-Boltzmann distribution indicates that this attenuation effect is negligible. No problem is expected from secondary collisions in the scattering region because of the relatively low intensities of the beams. In an auxillary experiment, a beam flag was installed on the Hg beam; no attenuation of the Tl beam by the Hg beam could be observed.

The object of the experiment is to measure the light signal that depends on the electron beam and therefore on the metastable Hg atom flux. Approximately fifteen settings of the velocity selector are chosen

before beginning the experiment; these settings are selected so that as large a range of relative velocities as possible is scanned with a due regard for Tl flux expected at each selector setting. Typically a range of 0.85 α_0 to 3.90 α_0 has been found useful. The failure to reach lower Tl velocities is due both to the increase of selector transmission with increasing velocity selected and to the shift of the velocity distribution to higher velocities due to the Laval effect. A counting period is chosen that allows the extraction of the signal from the background; typically 50 to 100 seconds is used. At each velocity selector setting the rotational frequency, the counts on each of the two scalar channels, and the exact counting period as measured on a stop watch are recorded. Concurrently the Tl beam flux and Hg^* beam flux are being recorded on the chart recorder; the position on the chart provides a record of the time during the experiment that the data point was taken. This procedure is executed at each of the selected settings; if the signal is particularly low, the process is repeated two or more times at a given setting. Periodically during a scan through the velocity range, a counting period is completed with the Tl beam blocked by the beam flag to check for any background modulated at the electron beam chopping frequency. Also periodic checks are made to verify that the two scalar channels continue to count for equal periods. As many scans as possible are made through the complete velocity range; termination of the experiment comes when some apparatus component malfunctions. In the event that it were deemed that enough scans had been made, it would be desirable to repeat the measurement of the velocity distribution of the Tl beam to check for any shift, but this situation has not arisen.

C. Data Analysis

If all of the collisionally excited species radiate before leaving the scattering region, the observed photon counts must be proportional to the total number of atoms excited to the emitting level per second (denoted by N'). Now

$$N' = V \iint n_{Tl}\, n_{Hg}\, Q_{eff}(g)\, gP(v_{Tl})\, P(v_{Hg})\, dv_{Tl}\, dv_{Hg} \qquad (1)$$

where

n_{Tl}, n_{Hg} = number density of Tl, Hg^* atoms in collision zone of volume V

v_{Tl}, v_{Hg} = velocity of Tl, Hg^* atoms

g = initial relative velocity = $(v_{Tl}^2 + v_{Hg}^2)^{1/2}$

$P(v_{Tl}), P(v_{Hg})$ = number density velocity distributions of the Tl, Hg^* atoms in the collision zone.

$Q_{eff}(g)$ = effective total cross section for excitation to the observed level.

It should be noted here that Q_{eff} is the total cross section not only for direct excitation in a collision of the level monitored but also for formation by cascade emission from higher states that are directly formed. In the present situation the distribution of Hg^* velocities, $P(v_{Hg})$, is almost a full thermal distribution[15] and the distribution of Tl velocities $P(v_{Tl})$ is the fairly broad distribution transmitted by the velocity selector. Instead of attempting to treat the experimental data directly be deconvoluting $Q_{eff}(g)$ from $P(v_{Tl})$ and $P(v_{Hg})$, an indirect two step method is resorted to: by assigning single velocities to both beams the total cross section as a function of velocity may be approximately extracted; then this curve is averaged over the initial relative velocity distribution to reproduce

the experimental data. If necessary the approximate curve may be adjusted until a satisfactory fit is achieved. Only the first step will be discussed here. Another member of this research group is completing the process.

To derive the approximate curve all mercury atoms are assumed to have the most probable source velocity and the transmission through the velocity selector is assumed to be a delta function. Since the observed photon counting rate, $S_{h\nu}$, is directly proportional to N', Eq. (1) yields

$$Q_{eff} \propto \frac{S_{h\nu}}{n_{Hg}\, n_{Tl}\, g} .$$

Within the framework of this approximation

$$n_{Hg} \propto \frac{S_{Hg}}{\alpha_{Hg}}$$

$$n_{Tl} \propto \frac{S_{Tl}}{v_0'}$$

where S_{Hg}, S_{Tl} are the measured beam flux intensities, α_{Hg} is the most probable mercury source velocity and v_0' is the most probable velocity transmitted by the velocity selector. Consequently

$$Q_{eff} \propto \frac{S_{h\nu}}{S_{Hg}\, S_{Tl}} \left(\frac{1}{v_0'^2} + \frac{1}{\alpha_{Hg}^2} \right)^{-1/2} \qquad (2)$$

The determination of v_0' and the data reduction and statistical analysis will now be discussed.

1. Calibration of Velocity Selector

The rotational frequency of the velocity selector rotor is an easily measured parameter, but relating its value to the exact distribution of velocities transmitted by the selector is fairly complicated. For a non-

divergent beam aligned perfectly parallel to the rotor the nominal velocity transmitted is given by

$$v_0 = \omega L/\phi.$$

(See Chapter VI for notation). The most probable velocity transmitted is v_0 but velocities in a range on either side of v_0 have smaller but finite probabilities of being transmitted. Hostettler and Bernstein[6] have derived equations for the transmission function. If perfect alignment and a non-divergent beam are assumed the velocity distribution can be derived from these equations. Considerations of probable alignment error indicate the calculated peak position should deviate no more than 5% from the true experimental value, but the width of the true transmission function is probably a factor of two greater than that calculated. In order to obtain a more accurate idea of the true transmitted velocity distribution, complicated calculations and an involved calibration procedure are necessary. The remainder of this section will be devoted to deriving these relatively minor corrections which arise from (1) a small misalignment of the center line of the beam with the rotor axis, (2) the effect of the divergence of the beam about the center line and (3) clogging of the slits of the first disk. Throughout this treatment, great simplication is achieved by using the small angle approximation which is very accurate for the magnitudes ($\leq 1^\circ$) of the angles that are involved. First the distribution of the transmitted velocities is calculated for a a non-divergent beam misaligned by an angle α. The divergence of the beam has the effect of introducing a distribution of misalignment angles. Thus, the transmitted velocity distribution is obtained by integrating the transmission function for a non-divergent beam over the distribution of misalignment angles.

Gillen[7] has generalized the equations of Ref. 6 to describe the transmission function for a non-divergent beam aligned at an angle α to the rotor shaft. A further problem has been encountered in this study: the Tl tends to collect on the first disk of the velocity selector and partially clog the slits of this disk. This clogging effect is expected to affect the transmission function. Visual observation indicates that primarily the beam material collects on the face of the disk and on the side of the slit moving toward the beam. Elementary considerations of the geometry involved indicate that the closing of the slit is more important than the thickening of the disk due to building-up of the beam material on the disk face. Using a treatment similar to that of Ref: 6 and 7 and denoting the amount of the slit that is clogged in units of length by δ yields:

$$B(v) = 0 \qquad v \leq v_{min}$$

$$B(v) = B_1(v) = \eta \left[1 - \left(\frac{\omega(L+d)}{v} - \phi - \frac{\alpha(L+d)}{r} \right) \frac{r}{\ell_1} \right] \qquad (3)$$

$$v_{min} \leq v \leq v_{crit}$$

$$B(v) = B_2(v) = \eta \left[1 - \left(\frac{d\omega}{v} - \frac{d\alpha - \delta}{r} \right) \frac{r}{\ell_1} \right] \qquad (4)$$

$$v_{crit} \leq v \leq v_0$$

$$B(v) = B_3(v) = \eta \left[1 - \left(- \frac{\omega(L-d)}{v} + \phi + \frac{\alpha(L-d)+\delta}{r} \right) \frac{r}{\ell_1} \right] \qquad (5)$$

$$v_0' \leq v \leq v_{max}$$

$$B(v) = 0 \qquad v_{max} \leq v$$

$$v_{min} = \frac{(L+d)\ \omega r}{\varphi r + \ell_\perp + (L+d)\alpha} \qquad (6)$$

$$v_{crit} = \frac{L\,\omega r}{\phi r + L\alpha + \delta} \tag{7}$$

$$v_0' = \frac{L\,\omega r}{\phi r + L\alpha} = \frac{L\omega}{\phi}\left(1 + \frac{L\alpha}{\phi r}\right)^{-1} \tag{8}$$

$$v_{max} = \frac{(L-d)\,\omega r}{\phi r - \ell_1 + (1-d)\alpha + \delta} \tag{9}$$

Physically, v_{min} is the lowest velocity transmitted and v_{max} is the highest; v_0' is the most probable velocity transmitted and v_{crit} is the lowest velocity attenuated by the slit clogging. The other notation is as defined in Chapter VI. Equations (6) and (8) are equivalent to the equations of Ref. 7 that give v_{min} and v_o; however here v_{max} given in Eq. (9) is less than the v_{max} that was derived in that eariler work. The sign of α is defined so that the rotor has to rotate through an angle greater than ϕ to transmit the nominal velocity when α is positive. The neglect of both the slit clogging from the other side of the slit and the beam material deposited on the face of the disk introduces small errors in the calculation of B(v), but since clogging on only one side of the disk is considered the treatment presented here places an upper limit on the distortion of the transmission function due to the clogging. Equation (4) and (5) are valid only when δ does not exceed 70% of the slit width; they break down at a somewhat higher degree of clogging. It should be noted that the four characteristic velocities given by Eq. (6)-(9) are each proportional to the rotational frequency, ω. Thus, the velocity transmitted is not only directly proportional to ω, but also the width of the transmission function $(v_{max}-v_{min})$ is proportional to ω. This feature implies that the total selector transmission increases directly proportional to ω.

For a non-divergent beam, the above generalized transmission function accounts for all possible effects that this writer has been able to recog-

nize with the exception of the variation of the transmission function with r, the radius of the disk. The appropriate value of r varies over the height of the transmitted beam. If α equals zero and δ equals zero, variation of r does not affect B(v), but if misalignment or clogging occurs, a small dependence of B(v) on r is observed. Calculations with values of δ and α believed to be upper limits for clogging and misalignment that could be present in this investigation show that the effect is very small ($< 0.3\%$) for the range of r due to the slit height. If an average value of r is taken, the effect largely cancels and, therefore, it has been neglected.

Now it is necessary to consider the distribution of misalignment angles which arises from (1) the error in alignment that is likely to result when optical alignment must be relied upon, and (2) the divergence of the beam that is present in any experiment. The procedure that has been adopted is to integrate the product of I(v) and B(v) over the distribution of misalignment angles [I(v) denotes the flux intensity as a function of velocity that is incident upon the selector and is related to P(v) in Eq. (1) by $I(v) \propto v\, P(v)$.]

In the apparatus employed here, the divergence of the beam may be geometrically calculated from the known slit parameters, but the misalignment of the center line of the beam with the rotor axis is unknown and δ can only be roughly measured visually. Consequently a calibration process is necessary if it is desired to determine the absolute value of v_0' to better than the 5% accuracy which can be easily achieved by optical alignment. This calibration process is rather involved due to two complicating factors: the thermal expansion of the oven causes α (this symbol

now represents the beam center line misalignment) to be a function of oven temperature and $I(v)$ is a function of the source pressure.

The first step of the calibration procedure was the writing of a computor program to integrate the product of $I(v)$ and $B(v)$ over the distribution of misalignment angles and then over the complete velocity range transmitted by the selector. By carrying out this calculation at various values of ω a theoretical curve is derived which may be compared with experimental measurements of S_{Tl} versus rotational frequency. At very low source pressures, the Maxwell-Boltzmann flux distribution is the appropriate $I(v)$ to integrate over, i.e.

$$I(v) \propto v^3 \exp(-v/\alpha_0)^2$$

(α_0 denotes the most probable source velocity). For this integration $\alpha = 0$ and $\delta = 0$. Multiplication of ν_{max}, the experimental rotational frequency that corresponds to the flux intensity peak, by 2π gives an effective angular velocity equal to $\omega_{max}(1 + L\alpha/r\phi)^{-1}$ where ω_{max} is equal to the angular velocity of the theoretical curve that corresponds to the peak of the flux intensity (Eq. (8) indicates why this is true). The equation

$$2\pi \nu_{max} = \omega_{max} \left(1 + \frac{L\alpha}{r\phi}\right)^{-1}$$

allows the value of α to be determined. Now, from Eq. 8

$$v_0' = \left[\frac{2\pi L}{\phi} \left(1 + \frac{L\alpha}{\phi r}\right)^{-1}\right]\nu \qquad (10)$$

where ν is the rotational frequency of the rotor. The factor in brackets (which will be denoted by R_0), should be very close to 897, the factor derived for perfect alignment (see Table II, Chapter VI); in all completed experiments this has been true to within 5%. The above discussion is

strictly applicable only to the situation with no clogging. Since clogging attenuates the higher velocities more than it does the lower velocities, a distortion of the velocity distribution results. Thus for $\delta \neq 0$, the factor derived above will not give v_0', but will give a slightly smaller, weighted average of the transmitted velocities. This is no problem in the approximate derivation of Q_{eff}, but this small effect should be taken into account by visually estimating δ when the velocity averaged total effective cross section curve is calculated. The calibration is made at the start of an experiment with low source pressures; therefore it is justified to set $\delta = 0$ in the integration to derive the theoretical curve. Later in the experiment δ may become finite but the value of α is not affected by the clogging. An example of a calibration curve is shown in Fig. 7 of the preceding chapter.

The first complicating factor must now be taken into account. Before proceeding however it is perhaps worthwhile to stress that it is a minor effect resulting in less than a 2.5% change in the value of R_0 derived in Eq. (10). When the temperature of the oven is increased, a thermal expansion takes place perpendicular to the beam axis. Thus, the misalignment angle changes. The situation is further complicated by the fact that the beam entering the collision zone is defined by the source slit and the collimating slit while the beam detected is defined by the detector width and the source slit. Only when the detector is placed at the center of the total beam profile is the same value of α appropriate to both beam distributions. This particular complication could have conceivably been avoided by constructing a detector that was larger than the beam profile, but this was not practical for several compelling experimental reasons.

The procedure that has been adopted is to center the detector in the beam profile and then to measure a velocity distribution. Unfortunately, the velocity distribution was usually taken at lower oven temperatures. Consequently, the value of R_0 (see Eq. 10) derived from the measured velocity distribution must be corrected for the thermal change of α to yield R_o' appropriate to the temperature at which the ovens were maintained during the measurement of the beam profile. In the small angle limit

$$R'_0 = \frac{2\pi L}{\phi} \left(1 + \frac{L\alpha'}{\phi r}\right)^{-1} \qquad (11)$$

where $\alpha' = \alpha + \Delta\ell/D$. Here $\Delta\ell$ is the displacement of the source slit due to the thermal expansion and D is the distance from the source slit to the detector. This adjusted factor is now also appropriate at this temperature to the total beam defined by the two slits. A final calculation must be made to yield R_0'', the conversion factor appropriate to the beam entering the collision zone at the higher oven temperatures that are required during the experiment. R_0'' is given by Eq. 11 if $\alpha'' = \alpha' + \Delta\ell'/D'$ is substitute for α'. Here $\Delta\ell'$ is the thermal expansion due to changing from the beam profile oven temperatures to the experimental oven temperatures and D' is the distance from the source slit to the collimating slit. In these calculations $\Delta\ell$ and $\Delta\ell'$ are roughly calculated by estimating the temperatures of the various components of the oven and clamp assembly.

Due to intensity limitations it has sometimes been necessary to measure velocity distributions at source pressures high enough that deviations from the Maxwell-Boltzmann distribution become appreciable. These deviations cause a narrowing of the velocity distribution and,

more importantly, a shift of the peak position to higher velocities. Consequently, it is difficult to estimate I(v) which is required to calculate the theoretical calibration curve. A study[8] of the velocity distribution in a molecular beam indicates that the simplest version of the Laval nozzle theory gives fair agreement with experiment. (A beam of metal atoms originating from a source equipped with a slit rather than a circular orifice was investigated; thus the results should be appropriate here.) This theory predicts

$$I(v) \propto w^3 \exp\left[-\rho^2 (w-\sigma)^2\right] \qquad (12)$$

where $w = v/\alpha_0$ and ρ and σ are related by

$$M = (2/\gamma)^{1/2} \rho \sigma$$

$$\rho = \left[1 + 1/2\,(\gamma-1)M^2\right]^{1/2}$$

where γ is the heat capacity ratio C_p/C_v and M is the Mach number which is rigorously defined as the ratio of the gross velocity of the volume of gas to the local speed of sound. In practice M is varied as a parameter of the calculation. Extensive computor calculations integrating Eq. (12) over the selector transmission function show that the measured velocity distributions at given values of σ and ρ should have very nearly identical shapes when plotted on the reduced units shown in Fig. 7 of Chapter VI regardless of the extent of clogging and magnitude of the misalignment angle, at least over the range that is considered possible in these experiments. The ordinate dimensionless units are obtained by dividing the intensity by the intensity at the peak and the abscissa units result from dividing the velocity by the velocity at which the peak of the distribution appears (see Caption of Fig. 7, Chapter VI for further discussion). It

should be noted that the peak velocity is a critical function of δ and α. Figure 2 shows the curve that is used to calibrate the selector. The long curve which (as will be discussed later) failed to give good results was derived from Eq. 12; it plots the peak position versus the full width at half maximum (FWHM) of the integrated distribution plotted with reduced units. By determining the FWHM of an experimental curve, the magnitude of the corresponding peak velocity may then be read off the graph if Eq. (12) adequately describes the true I(v). This peak velocity and the rotational frequency at which the peak appeared yield the value of R_0 when substituted in Eq. (10). From this point the calibration is identical to that of the Maxwell-Boltzmann distribution. This theoretical curve derived from Eq. (12), however, does not give consistent results for several velocity distributions taken with the same alignment but at different source pressures. This observation is ascribed to a failure of Eq. (12) to adequately describe the velocity distributions. Consequently, an empirical curve (shown in Fig. 2 with the data points) was derived from four velocity distributions measured for various source pressures but with the same alignment. This empirical curve was used for the calibration in all experimental runs.

Table I presents the results of all of the velocity selector calibrations.

2. Data Reduction and Statistical Analysis

It is desired not only to obtain the most accurate dependence of Q_{eff} on relative velocity, but also to place reliable limits on the accuracy of each data point. The digital nature of the primary data allows the determination of the probable error by a reasonably objective statistical

analysis. There are essentially three steps in this process: calculation of the magnitude and standard deviation of Q_{eff} for each data point, time normalization of the calculated values, and calculation of the most reliable value and standard deviation of Q_{eff} at each relative velocity that was investigated. These three steps will now be discussed consecutively.

a. Calculation of relative magnitude and standard deviation of Q_{eff} for each data point.

No attempt is made to directly calculate the absolute Q_{eff}; all calculations are for relative values and are obtained from (2) using a proportionality constant equal to 1. S_{Hg} and S_{Tl} are read from the chart recording taken during the experiment. The product of the measured rotational frequency with the conversion factor derived by the calibration of the velocity selector yields v_0'. The value of α_{Hg} is calculated from the measured temperature of the Hg beam source. Calculation of $S_{h\nu}$, however, is complicated by the observation that a small positive photon signal in phase with the electron beam is registered when the Tl beam is blocked. This signal could possibly arise from several sources: a small detection efficiency for the fluorescence of the metastable atoms in the collision zone; a greater photon counting efficiency on one channel; or a small difference in counting periods between the two channels. This background has been found to be correlated with time but not with the Tl beam intensity. This latter observation indicates that this background signal is not due to a small amount of the Tl beam passing the beam flag. $S_{h\nu}$ is the difference between the two scalar readings (expressed in units of counts per hundred seconds) minus a correction for the background.

TABLE I. Summary of Velocity Selector Calibrations

Date	ν_{max}	FWHM	R_0	R_0'	R_0''	$\lvert 1 - R_0''/897 \rvert \times 100$
3/24/70	45.00	.8465	902.9	902.3	910.1	1.5
4/ 8/70	43.64	.9290	856.6	856.5	864.7	3.6
4/22/70	41.90	.9395	835.7	836.9	853.6	4.8
7/ 7/70	46.25	.8625	879.0	877.7	887.5	1.1
7/10/70-A	42.22	.9410	875.7	877.7	887.5	1.1
7/10/70-B	42.29	.9480	876.5	877.7	887.5	1.1
7/10/70-C	42.49	.9460	877.2	877.7	887.5	1.1

Figure 2. Variation of peak velocity, V_{MP}, in the measured or integrated velocity distribution as a function of the FWHM of that velocity distribution plotted in reduced units. The long solid curve was calculated using Eq. (12). The shorter curve with the data points was derived from four experimental velocity distributions taken with the same alignment; the distribution measured at the lowest source pressure (see Fig. 7 Chapter VI for this curve) was assumed to be unshifted from the Maxwell-Boltzmann peak. The numbers running along the theoretical curve indicate the Mach number. The most probable source velocity is denoted by α_0.

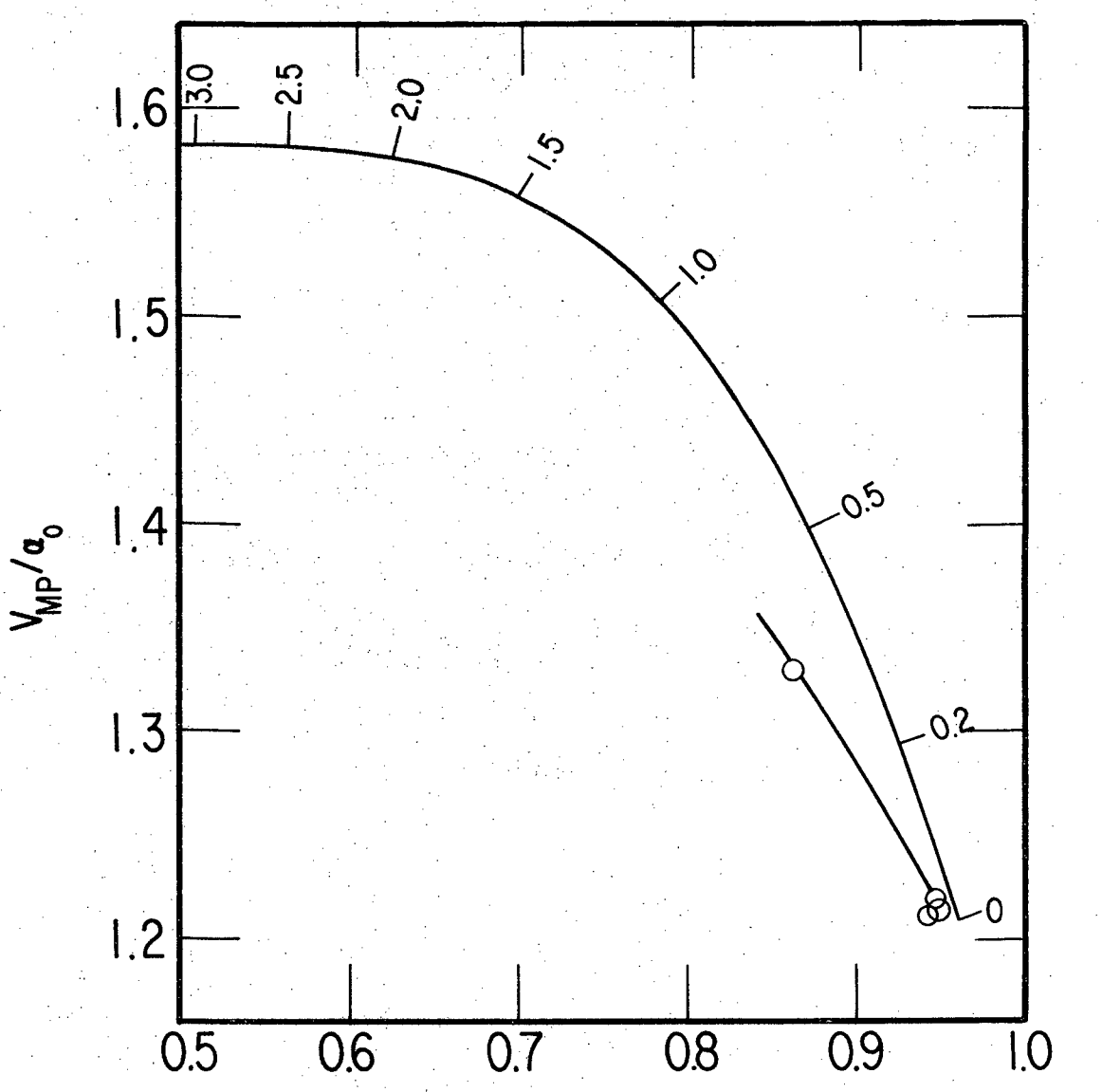

XBL 709-6671

Figure 2

This background correction term is calculated from an expression which is a function of time and is obtained by fitting the measured background magnitudes to an appropriate functional form. In the experiments investigating the 5350Å Tl line (the results will be discussed later) the measured background showed no correlation with S_{Hg}. This background was very small (typically 10% of the maximum Tl fluorescence photon signal) and a least squares linear fit of the background versus time was as high an order fit as was justified by the statistical scatter of the data. The background to be subtracted at each data points was calculated from this linear fit. In experiments involving the 2816Å Tl line, the measured background (due to Hg^* emission) was much larger (typically 90% of the total photon signal) and was found to be, within statistical limits, directly proportional to S_{Hg}; consequently a more sophisticated treatment was necessary. The measured background data point, in units of counts per 100 seconds, was divided by S_{Hg} measured simultaneously with the photon signal. These data points were then fit to a Legendre polynomial expansion[9] in time. In both fitting procedures the deviations of the measured points from the fitted curve were consistent with the statistical uncertainties in the measured signals.

For experiments where the linear fit to the background is sufficient, the above discussion results in the equation

$$Q_{eff} = [(NA-NB)\ 100/TN - (A+BT)] \left(\frac{1}{v_{0'}^2} + \frac{1}{\alpha_{Hg}^2} \right)^{-1/2} (S_{Hg}\ S_{Tl})^{-1} \qquad (13)$$

where

NA, NB = counts recorded on channel A, B

TN = counting period

A = intercept of linear fit to background

B = slope of linear fit to background

T = time during experiment that data point was taken.

Simple error propagation theory[10] allows an approximate standard deviation σ_Q, to be assigned to each data point. Appendix A details the calculation of σ_Q.

b. Time normalization of calculated values of Q_{eff}

If the detection efficiencies of the two beam monitors and the photomultiplier assembly remained constant throughout the experimental run, the values of Q_{eff} calculated in the preceding section would be the final data points. However values of Q_{eff} measured at the same velocity show a definite correlation with time. This time variation is ascribed to a change in one or more of the three detection efficiencies Therefore a time normalization procedure is necessary.

The use of a time normalization process is resorted to in many molecular beam studies. Usually in other studies one reference data point that is relatively noise-free has been chosen and its value periodically measured to follow the time variation of the signal. Here all of the data points are relatively noisy and the measurement of each is repeated several times. Therefore, a more sophisticated time normalization treatment is required. The procedure adopted here is (1) to calculate the most probable value of the mean of all the measured data points taken at each relative velocity, (2) to calculate reduced data points by dividing each data point by the calculated mean of all the data points taken at that relative velocity, (3) to fit all of these reduced data points to a Legendre polynomial expansion in time, (4) to obtain time normalized data

points by dividing each original data point by the value of the Legendre expansion corresponding to the time that the data point was taken, and (5) to repeat steps (1)-(4) with the mean recalculated from the time normalized data points obtained in step (4). This repetition continues until the sum of the squares of the deviations of the reduced data points from the Legendre expansion converges to a minimum. A paragraph will now be devoted to each of these steps.

At a given relative velocity the most probable value of the mean of an infinite number of measurements of Q_{eff} at that velocity may be approximately calculated from the finite set of measurements made during the experiment by a weighted average,[10]

$$\bar{Q}_{eff} = \Sigma \left(Q_{eff_i}/\sigma^2_{Q_i}\right) / \Sigma \left(1/\sigma^2_{Q_i}\right) \tag{14}$$

(Here as elsewhere a bar over a symbol indicates the average value.) The value of $\bar{Q}_{eff}$ is calculated for each relative velocity.

Each reduced data point, Q^R_{eff}, may be calculated by dividing each Q_{eff} by the appropriate $\bar{Q}_{eff}$. The uncertainty of each reduced data point must also be calculated from

$$\frac{\sigma^2_{Q^R}}{Q^{R\,2}_{eff}} = \frac{\sigma^2_Q}{Q^2_{eff}} + \frac{\sigma^2_{\bar{Q}}}{\bar{Q}^2_{eff}} - \frac{2\sigma^2_{Q\bar{Q}}}{Q_{eff}\,\bar{Q}_{eff}} \tag{15}$$

The estimated standard deviation of the mean is calculated from

$$\sigma^2_{\bar{Q}} = \left(\Sigma\ 1/\sigma^2_{Q_i}\right)^{-1} \tag{16}$$

and $\sigma_{Q\,\bar{Q}}$, the covariance[10] of Q_{eff} and $\bar{Q}_{eff}$, is approximately equal to $\sigma_{\bar{Q}}$.

The computor program LEGFIT from Ref. 10 is used to fit the reduced data points to a Legendre polynomial expansion. This expansion is defined by

$$F(t) = \sum_n a_n P_n (\cos t) \qquad (17)$$

where $0 \leq t \leq 180$. Thus, it is necessary to express the time span of the experiment on this scale. This coordinate change is accomplished by

$$t = cT - d$$

where $c = 0.96 \ [180/(T_{max} - T_{min})]$ and $d = c\, T_{min} - (.02)(180)$. A maximum of ten terms is used in the expansion, but the expansion is terminated at a lesser number if an additional term is not statistically justified. The F distribution test of an additional term as described in Ref. 10 is applied after the calculation of each additional term to determine if that term is statistically justified. If the probability is 5% or greater that a set of points with random deviations from the n-1 term expansion would be fit by the n term expansion as well as the true data points are actually fit, then the expansion is terminated at n-1 terms. Each of the reduced data points is weighted by $1/\sigma_{Q^R}^2$. A special case is presented if only a single measurement of Q_{eff} is made at a given relative velocity because Q_{eff}^R will always be equal to 1 on the first iteration. Since this single data point cannot contain any information about the time variation of the signal, it is given essentially zero weighting during the calculation of the Legendre polynomial expansion.

The time normalized data points may now be calculated by dividing each data point by F(t); each such data point is denoted by Q_{eff}^T. The expected uncertainty, σ_{Q^T}, may be approximately calculated from

$$\frac{\sigma_{Q^T}^2}{Q_{eff}^{T\ 2}} = \frac{\sigma_Q^2}{Q_{eff}^2} + \frac{\sigma_F^2}{F(t)^2} \qquad (18)$$

where σ_F is the uncertainty of F(t) and may be estimated from

$$\sigma_F^2 = \sum_n P_n^2 (\cos t)\, \sigma_{a_n}^2$$

where σ_{a_n}, directly evaluated by the computor program of Ref. 10, represents the uncertainty in the value of a_n.

Now these four steps may be repeated with a few changes. The new averages, $\bar{Q}^T_{eff}$, for step (1) are calculated from Eq. (14) by substituting Q^T_{eff} and $\sigma_{Q^T_i}$. In step (2) Eq. 15 is still the appropriate expression for σ_{Q_R} if the time normalized values of the average and its uncertainty are substituted. However, the covariance is more complicated, and is estimated from

$$\sigma^2_{Q\,\bar{Q}T} = \sigma_{Q^T}^2 \left[F(t)\ \sigma_{Q^T}^2 \sum \frac{1}{\sigma_{Q^T_i}^2}\right]^{-1}. \qquad (19)$$

Repetition continues until the sum of the squares of the deviations of the reduced data points from F(t) decreases by less than 10% between two successive calculations. For all sets of data analyzed, three sucessive iterations have sufficed. Figure 3 shows the final fit of F(t) for the experiment with the most extensive data; this experiment also exhibited the greatest range of values for F(t).

This procedure for time normalization has proven very valuable for the limited number of completed experiments that have shown a reasonable signal to noise ratio. When the data becomes noisy enough that a significant number of data points lie below zero, the average value of the data

Figure 3. Legendre polynomial fit to the reduced data points. Five terms were considered justified according to the criterion given in the text. The function giving the solid curve is the factor that is divided by in order to time normalize Q_{eff}, the measured effective cross section.

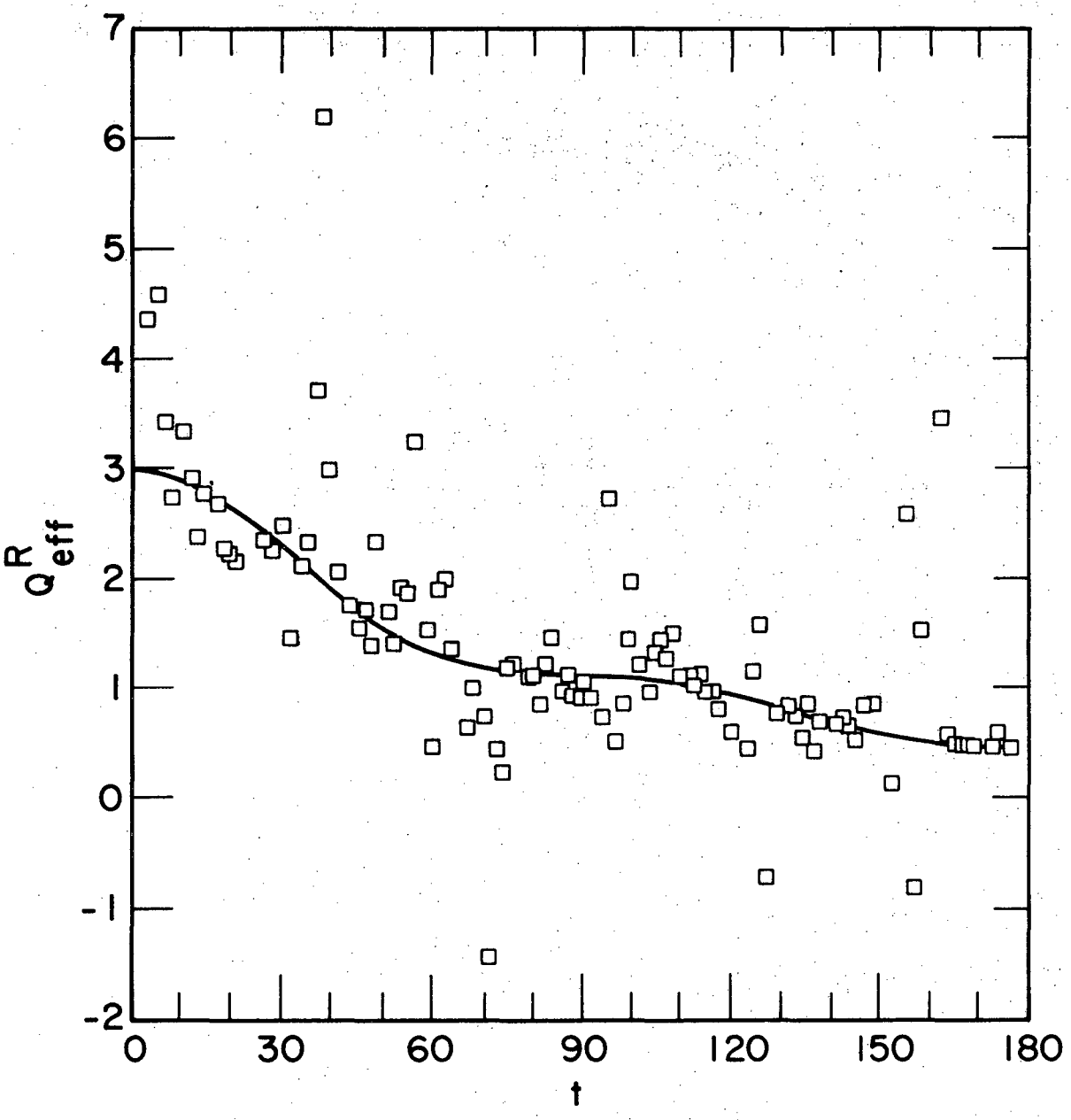

XBL 7010-6783

Figure 3

points at a particular velocity becomes small with respect to the absolute values of the data points. Thus the Q^R_{eff} values diverge and the procedure breaks down. It is unfortunate that we have not yet succeeded in the extraction of meaningful results from data with a signal to noise ratio of zero. This procedure becomes dangerous to use under two conditions: when the number of terms in the Legendre polynomial expansion becomes comparable to the number of data points and when many measurements of each data point have not been made at scattered times. By testing the significance of each term in the expansion, one has a safeguard against achieving a fit that passes through all the data points thereby removing not only all scatter in the data but also all reliable information. Another check that will further substantiate our belief that we have not over-corrected for the time variation in the data will be discussed in the next section. In order to avoid the second danger, repeated scans through the selected velocities are made in varying sequence; the experiment shown in Fig. 3 represents at least five measurements at the majority of the points and up to twice that many at the nosiest points which lie at the edges of the Tl velocity distribution.

c. Calculation of most reliable values and estimated standard deviations of Q_{eff}

The weighted mean (denoted by Q for the remainder of this chapter) of the final values of Q^T_{eff} (the time normalized effective cross sections) calculated from Eq. (14) where the final values of σ_{Q^T} (the estimated uncertainties of Q^T_{eff}) have been used are the most reliable values that may be extracted from the data. Two methods may be used to estimate the standard deviations of Q: direct calculation from the deviations of the

experimental points, Q^T_{eff}, from Q and calculation by error propagation theory from the original data. Direct calculation gives σ_D from

$$\sigma_D = \left(\frac{\sum_{j=1}^{N} (Q^T_{eff_j} - Q)^2}{N-1} \right)^{1/2} \qquad (20)$$

while treatment by error propagation results in σ_E expressed by

$$\sigma_E = [\Sigma \ (1/\sigma_{Q^T_i}{}^2)]^{-1/2} \qquad (21)$$

where the σ_{Q^T} values are the final calculated uncertainties of the time normalized data points; see Eq. (18) for the calculation of these values. These two estimates of the standard deviations of the averages should be mutually consistent. If σ_D were found to be consistently significantly smaller than σ_E, it would indicate that the time normalization might have been more closely fit to the data than was statistically warrented. Figure 4 shows the final results for the data included in Fig. 3. The two standard deviations are of comparable magnitudes and neither seems to consistently dominate the other. Calculations have been made replacing the 5% probability cutoff in the time normalization by 50%. In this case nine terms were included, and it could be discerned that, for the points most heavily weighted in the time normalization, σ_E was consistently larger than σ_D. However, it should be emphasized that the magnitudes of the resultant values of Q showed only very slight differences from those shown in Fig. 4.

D. Results and Discussion

Studies of two Tl lines have been concluded. No indication of the velocity dependence of the 2826Å Tl fluorescence could be extracted because the modulated background photon signal was too large. The interference filter transmitted too great a fraction of the fluorescence of

Figure 4. Final results from one experimental run. The circles indicate the individual time normalized data points. The diamonds give the calculated means. Two error bars are shown for each mean: the left ones give $Q \pm \sigma_E$ while the ones on the right show $Q \pm \sigma_D$.

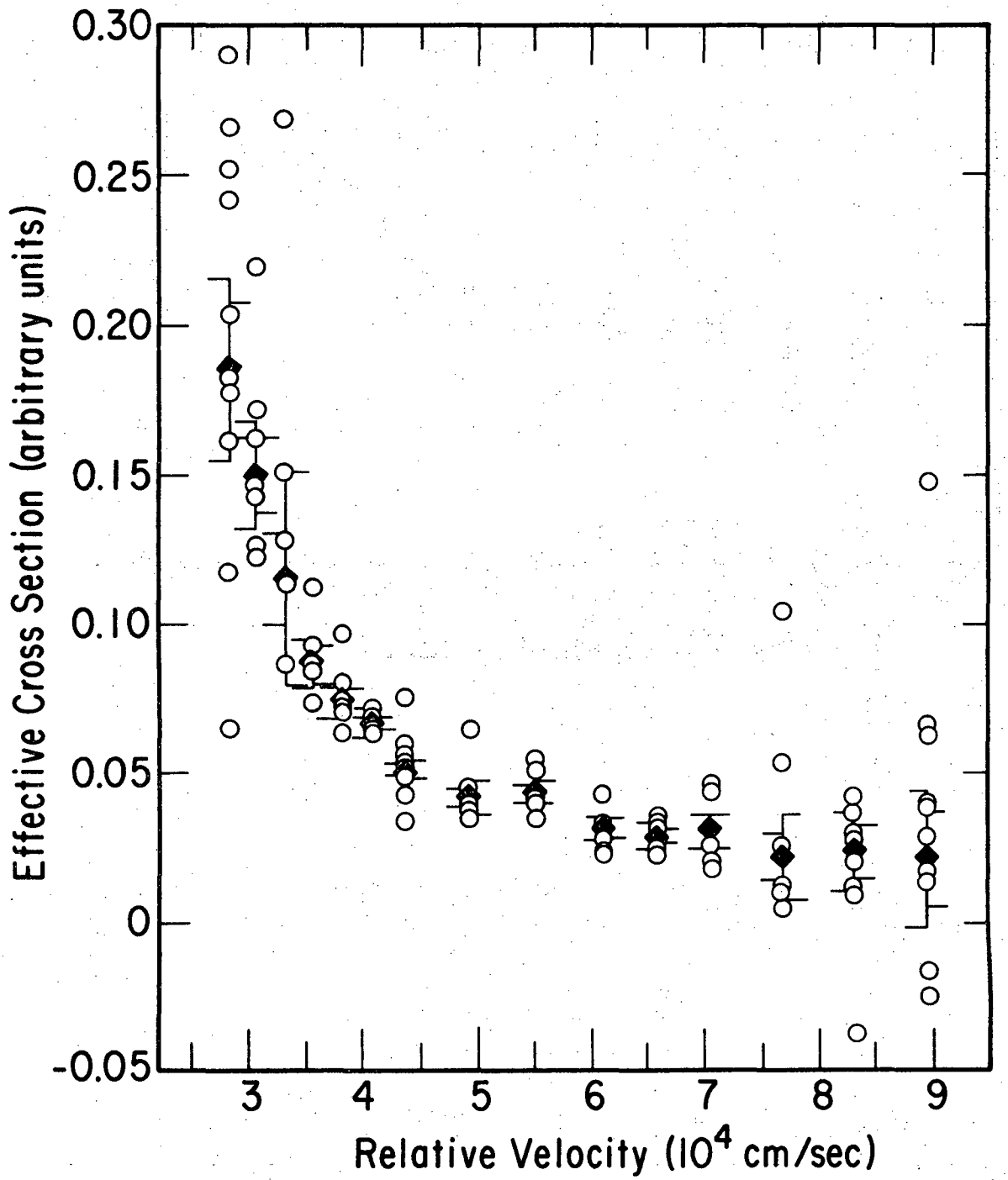

XBL 7010-6785

Figure 4

the metastable mercury atoms. The values of Q_{eff} before time normalization do indicate, however, that there is a positive Tl fluorescence signal and further studies with improved wavelength resolution are contemplated. Results have been obtained for the 5350Å Tl fluorescence, and thus the effective cross section for the formation of Tl 7s $^2S_{1/2}$ level is obtained. Figure 5 presents the velocity dependence of this cross section. It is clear that the cross section decreases rapidly with relative velocity and that the measured values of the cross section are fit well by a curve proportional to the inverse of the square of the relative velocity.

A curve fit to the derived values of Q is being integrated over the experimental distribution of relative velocities by another member of this research group. Final integrated curves are not yet available, but preliminary results indicate that the averaging process has very little effect, at least for cross sections that decrease as V^{-1}.

The significance of the possible V^{-2} dependence will not be discussed here. A comprehensive discussion will await the results of further experiments on the Tl-Hg* system as well as other collision partners.

The 5350Å Tl line is due to emission from Tl 7s $^2S_{1/2}$ (see Fig. 1). The energy discrepancy between this level and the two metastable mercury levels is so great that it very likely that direct excitation is negligible compared to excitation by cascade radiation from higher Tl levels. Since Hg $^3P_2$ is the most prevalent metastable level (see Chapter VI) and since there are Tl levels closer to this level than to Hg $^3P_0$, it is also very probable that the $^3P_0$ level contributes only slightly to the effective total cross section for the collisional excitation of the Tl 7s $^2S_{1/2}$ level. The four selection rules of Ref. 2a can yield some indication

of what Tl levels are originally excited. The Wigner spin rule is fulfilled for all of the transitions; therefore this rule is of no help here. The first two rules involving the energy discrepancy suggest that the 9s $^2S_{1/2}$, 9p $^2P_{1/2,3/2}$, 8d $^2D_{3/2,5/2}$ and 6f $^2F_{5/2,7/2}$ states are perhaps the most likely candidates for direct excitation. The initial resultant electronic angular momentum, J, of the collision partners, Hg $^3P_2$ and Tl $^2P_{1/2}$, is either 3/2 or 5/2; thus Tl 9p $^2P_{3/2}$, 8d $^2D_{3/2,5/2}$ and 6f $^2F_{5/2}$ are the states in the preceding list of candidates that satisfy the fourth, partial selection rule. Since of these four levels only the $^2P_{3/2}$ state can readily radiate to the 7s $^2S_{1/2}$ state in a single transition and moreover since it has nearly the smallest energy discrepancy, it is likely that this is the predominate state directly excited in the collision. However, significant contributions from other states, especially 9p $^2P_{1/2}$, cannot be ruled out.

The study of the velocity dependence of electronic energy transfer between atoms is potentially very interesting. These processes are generally believed to be curve crossing phenomena.[11,12] Consequently, collisions involving electronic energy transfer may proceed by either of two trajectories. During the traversal of one of the possible trajectories, the collision partners cross to the final surface on the incoming path and then do not recross on the outgoing leg. The other trajectory is characterized by no curve crossing on the incoming path and then the transition to the final curve takes place on the outgoing part of the trajectory. Thus, scattering from two potential energy functions occurs simultaneously. Semi-classical analysis of systems where similar phenomena occur[13,14] indicate that if both curves give scattering at the same center of mass angle (i.e. if the

Figure 5. Velocity dependence of the effective cross section for the formation of Tl 7s $^2S_{1/2}$ in collisions with Hg $^3P_{0,2}$ metastable atoms. The different symbols indicate separate experimental runs which have been normalized to give the best overall agreement. Included for comparison are three functions of the relative velocity; they are normalized to the same value at $V = 6\times10^4$ cm/sec. The error bars ($Q\pm\sigma_E$) give the estimated two-thirds confidence limits evaluated by error propagation.

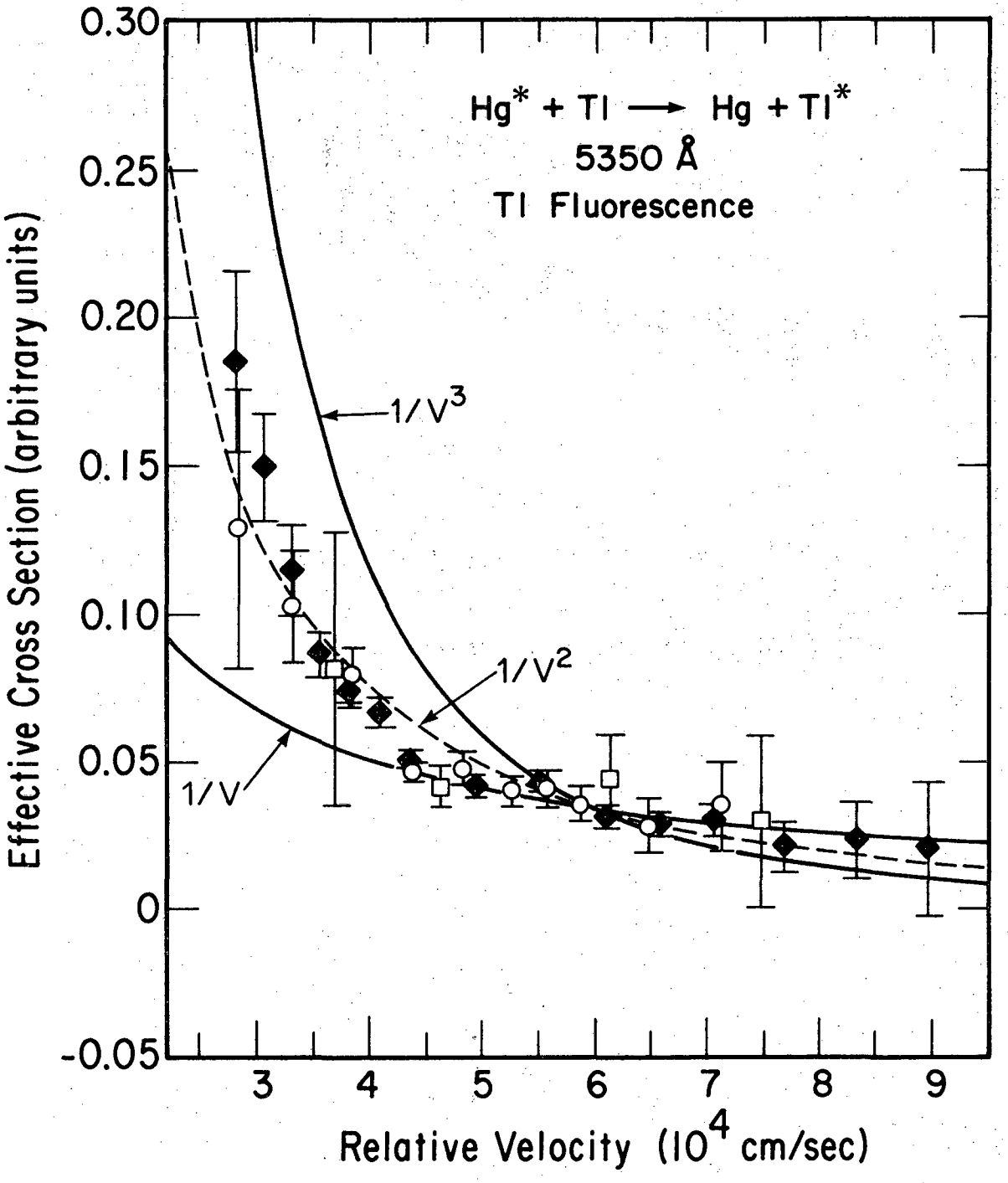

XBL 7010-6784

Figure 5

deflection functions intersect for some value of the orbital angular momentum in the partial wave formulation) interference effects can occur. The experimentally observable manifestation of this phenomenon should be undulations superimposed upon the cross section versus relative velocity curve. If these quantum undulations can be resolved, they should yield detailed information concerning the potential surfaces. Such quantum effects have been observed in an experimental study of the velocity dependence of the total cross section for resonant charge exchange[13] and have been predicted theoretically for Penning Ionization.[14] Experiments are planned with an improved signal to noise ratio and better velocity resolution to attempt to observe these features for non-resonant electronic excitation transfer. The $Li + Hg^*$ system is the likely candidate for this study.

REFERENCES

1. J. Franck, Z. Physik 9, 259 (1922).

2. G. Cario and J. Franck, Z. Physik 17, 202 (1923).

2a. J. G. Winans, Rev. Mod. Phys. 16, 175 (1944).

3. M. H. Ornstein and R. N. Zare, Phys. Rev. 181, 214 (1969) contains a summary and bibliography of the investigations of electronic energy transfer between atoms of different species.

4. R. E. Swanson and R. H. McFarland, Phys. Rev. 98, 1063 (1955).

5. E. K. Kraulinya and A. E. Lezdin, Opt. i. Spektroskopiya 20, 539 (1966) (English transl: Opt. Spectry. (USSR) 20, 304 (1966).)

5a. G. Herzberg, Molecular Spectra and Molecular Structure I. Spectra of Diatomic Molecules (D. Van Nostrand Co., Inc., Princeton, N.J. 1950).

6. H. U. Hostettler and R. B. Bernstein, Rev. Sci. Instr. 31, 872 (1960).

7. K. T. Gillen, PhD Thesis, University of Wisconsin, 1970.

8. R. J. Gordon,R. R. Herm, D. R. Herschbach, J. Chem. Phys. 49, 2684 (1968).

9. The procedure for fitting data points to a Legendre polynomial expansion will be fully discussed in a later section of this chapter.

10. P. R. Bevington, Data Reduction and Error Analysis for the Physical Sciences (McGraw Hill Book Co., New York, 1969). This book was found to be a very useful reference for statistical analysis because it presented not only the theory but also practical computor programs for application.

11. N. F. Mott and H. S. W. Massey, The Theory of Atomic Collisions 3rd ed. (Oxford University Press, London, 1965).

12. R. W. Anderson, Ph.D. Thesis, Harvard University, 1968. This work presents a very comprehensive study of nonadiabatic (i.e. curve crossing) processes.

13. R. E. Olson, Phys. Rev. 187, 153 (1969).

14. W. H. Miller, J. Chem. Phys. 52, 3563 (1970).

15. By measuring the fluorescence from the metastable mercury atoms in the collision zone as a function of time after the electron beam was turned on, it has proven possible to extract an approximate velocity distribution of the metastable atoms. Since the widths of the viewing region of the photomultiplier and of the excitation region are small compared to the distance between the two, a time of flight technique is applicable. The measured distribution is unshifted from the Maxwell-Boltzmann peak but a considerable attenuation of the low velocity atoms is apparent.

APPENDIX A. CALCULATION OF σ_Q

The techniques of simple error propagation as presented in Ref. 10 are used here.

$$\frac{\sigma_Q^2}{Q_{eff}^2} = \frac{\sigma_I^2}{I^2} + \frac{\sigma_{II}^2}{II^2} + \frac{\sigma_{III}^2}{III^2} \qquad (A1)$$

where I, II and III denote the first, second and third terms of the right side of Eq. (13). The distribution of many measurements of the counts recorded during a certain time interval should be well represented by the Poisson distribution.[10] Thus

$$\sigma_I^2 = [NA + NB + \left(\frac{\sigma_{TN}[NA-NB]}{TN}\right)^2] \left(\frac{100}{TN}\right)^2 - \sigma_{BkG}^2 \qquad (A2)$$

σ_{TN} is the estimated uncertainty in the counting period

σ_{BkG} gives the expected uncertainty in the calculated background value. It is approximately evaluated by

$$\sigma_{BkG} = \left[\frac{\sum_{i=1}^{J} (BkG_i - [A+BT_i])^2}{J-2}\right]^{1/2} \qquad (A3)$$

which is simply the calculated standard deviation of the J experimental measurements, BkG_i, of the background from the linear, least squares fit.

Using approximate analysis:

$$\frac{\sigma_{II}^2}{II^2} = \left[\frac{\alpha_{Hg}^4}{v_0'^2} \sigma_{v_0'}^2 + \frac{v_0'^4}{\alpha_{Hg}^2} \sigma_{\alpha_{Hg}}^2\right] (\alpha_{Hg}^2+v_0'^2)^{-2} \qquad (A4)$$

$\sigma_{v_0'}$ is the estimated uncertainty in v_0' and is approximately evaluated by

$$\sigma_{v_0'}^2 = v_0'^2 (\sigma_{FREQ}^2/FREQ^2) \qquad (A5)$$

FREQ is the rotational frequency of the rotor and its estimated uncertainty of measurement is σ_{FREQ}. The uncertainty in the factor that converts rotor frequency to v_o' has been neglected because it must be the same for all data points.

$\sigma_{\alpha_{Hg}}$ represents the expected standard deviation in α_{Hg} and is approximately given by

$$\sigma_{\alpha_{Hg}} = \frac{1.2897}{2} (MT)^{-1/2} \sigma_T \qquad (A6)$$

T is the Hg source temperature and σ_T is its expected uncertainty. M is the molecular weight of Hg.

$$\frac{\sigma_{III}^2}{III^2} = \frac{\sigma_{Tl}^2}{S_{Tl}^2} + \frac{\sigma_{Hg}^2}{S_{Hg}^2} \qquad (A7)$$

σ_{Tl} and σ_{Hg} give the estimated uncertainties in the measurement of the Tl and Hg signals, respectively.

All of the values in the above equations are known or may be reasonably estimated; thus, a numberical value of σ_Q may be derived.

ACKNOWLEDGEMENTS

It has been a valuable experience and a pleasure to work with Professor Ronald Herm during the past four years. He has never failed to receive my most naive questions with patience and enlightening suggestions. The relaxed yet exciting and inspiring atmosphere that he has provided for research and study has encouraged the fullest utilization of individual initiative. At the same time he has directed my efforts into exciting and realistic projects.

The people who compose the two research groups which have shared the same facilities and efforts deserve special thanks for many discussions and suggestions. In particular I would like to thank Ching-Hon Loh and Charlotte Sholeen for the beneficial experience of our joint effort on the sensitized fluorescence investigation.

The technical assistance of the LRL and Chemistry Department personnel has been an invaluable aid to my work. Especially important were Phil Eggers who maintained the apparatus electronics and Carl Baugh who directed the fabrication of many of the mechanical components of the apparatus.

My friends in Berkeley have all helped to make my life here more enjoyable and meaningful; in particular I wish to single out Jill Lawson for a special note of gratitude.

Finally I want to thank my mother for encouragement from a distance.

This work was conducted under the auspices of the Atomic Energy Commission, whose support I gratefully acknowlege.

TECHNICAL INFORMATION DIVISION
LAWRENCE RADIATION LABORATORY
UNIVERSITY OF CALIFORNIA
BERKELEY, CALIFORNIA 94720